Amplitude Analysis of the Charmless Decays of Charged B Mesons to the Final States K+- Pi-+ Pi+- Using the BaBar Detector

By Thomas Edward Latham

SLAC-R-834

Prepared for the Department of Energy
under contract number DE-AC02-76SF00515

Printed in the United States of America. Available from the National Technical Information Service, U.S. Department of Commerce, 5285 Port Royal Road, Springfield, VA 22161.

Amplitude analysis of the charmless decays of charged B mesons to the final states $K^{\pm}\pi^{\mp}\pi^{\pm}$ using the *BABAR* detector

Thomas Edward Latham

University of BRISTOL

Department of Physics

University of Bristol

June 8, 2005

A thesis submitted to the University of Bristol in accordance with the requirements of the degree of Doctor of Philosophy in the Faculty of Science

38 000 words

There is a theory, which states that if ever anyone discovers exactly what the universe is for and why it is here it will instantly disappear and be replaced by something even more bizarrely inexplicable.
There is another theory, which states that this has already happened.

– Douglas Adams

Abstract

Results of an amplitude analysis of the $B^+ \to K^+\pi^-\pi^+$ Dalitz plot are presented. The analysis uses a data sample with an integrated luminosity of $210.6\,\mathrm{fb}^{-1}$, recorded by the *BABAR* detector at the PEP-II asymmetric B Factory. This sample corresponds to 231.8 million $B\overline{B}$ pairs. Branching fractions and 90% confidence level upper limits are calculated, averaged over charge conjugate states ($\mathcal{B}$). For those modes that have significant branching fraction measurements *CP* violating charge asymmetry measurements are also presented (A_{CP}). The results from the nominal fit are summarised here:

- $\mathcal{B}(K^{*0}(892)\pi^+;\, K^{*0}(892) \to K^+\pi^-) = (8.53 \pm 0.74 \pm 0.46) \times 10^{-6}$
- $\mathcal{B}(K_0^{*0}(1430)\pi^+;\, K_0^{*0}(1430) \to K^+\pi^-) = (34.7 \pm 1.8 \pm 1.6) \times 10^{-6}$
- $\mathcal{B}(\rho^0(770)K^+;\, \rho^0(770) \to \pi^+\pi^-) = (5.17 \pm 0.80 \pm 0.37) \times 10^{-6}$
- $\mathcal{B}(f_0(980)K^+;\, f_0(980) \to \pi^+\pi^-) = (9.36 \pm 0.98 \pm 0.47) \times 10^{-6}$
- $\mathcal{B}(\chi_{c0}K^+;\, \chi_{c0} \to \pi^+\pi^-) < 2.4 \times 10^{-6}$
- $\mathcal{B}(K^+\pi^-\pi^+ \text{ non resonant}) < 10.8 \times 10^{-6}$
- $A_{CP}(K^{*0}(892)\pi^+;\, K^{*0}(892) \to K^+\pi^-) = (5.7 \pm 7.7 \pm 5.7)\%$
- $A_{CP}(K_0^{*0}(1430)\pi^+;\, K_0^{*0}(1430) \to K^+\pi^-) = (-6.5 \pm 3.3 \pm 2.0)\%$
- $A_{CP}(\rho^0(770)K^+;\, \rho^0(770) \to \pi^+\pi^-) = (32 \pm 13 \pm 6)\%$
- $A_{CP}(f_0(980)K^+;\, f_0(980) \to \pi^+\pi^-) = (9.3 \pm 9.7 \pm 2.6)\%$

Acknowledgements

Firstly I'd like to thank PPARC for giving me this incredible opportunity, both to work in this amazing field and to experience life in California.

I've spent time with a number of great people over the last three years. Many thanks go to each of them for all sorts of reasons:

My two supervisors: Nicolo de Groot and Fergus Wilson for all their support, advice and encouragement.

The $K\pi\pi$ Krew: Wahid Bhimji, Nicole Chevalier and Huw Shorthouse. For letting me get involved so soon in my PhD and for teaching me so much. Also for the times in the Vaults after a long day fit testing!

The UK Dalitz group, especially John Back, Paul Harrison and Sian Morgan. It's a great pleasure to be able to work more closely now with John and Paul at Warwick. Many thanks go to Sian for being an excellent person to work with on this analysis. Despite all the set backs and horrors we made it work! Thank goodness for West Wing and Ravenswood!!

My office mates at SLAC: Jamie Boyd and Marc Kelly. For your geniusness in all matters.

All the Bristol particle group (who haven't already been mentioned), in particular Nick Barlow, Jim Burke, Phil Clark and Noel Cottingham.

The *BABAR* Charmless and Trigger groups.

Jamie G, Jack, Manny, Eric and all the other *BABAR*ians at SLAC for making my

time there so enjoyable.

Barlow, Bhimji and Boyd for the excellent parties on Twin Peaks!

All my non-particle-physics friends for your very subtle humouring of me while I was writing this thesis and for being generally fantastic people, in particular: Brendan, Chris, Ben, Jamie Fatlad, Marco, Kate & Dave, the "C-floor clique" and all my other friends from Bristol.

Kelly: you've made the last two and a half years the most enjoyable of my life. You've been an incredible help and wonderful companion on the journey. I hope the coming years will be as exciting, and I look forward to sharing them with you.

Lastly I'd like to thank my family and in particular my parents for all their love and faith over the years. Without you I would never have been able to do this. Thanks for encouraging me to watch the RI Christmas Lectures all those years ago and for always supporting me in the choices I've made that have brought me here.

Declaration

I declare that the work in this thesis was carried out in accordance with the Regulations of the University of Bristol. No part of the thesis has been submitted for any other academic award at this or any other university. Any views expressed in the dissertation are those of the author.

The data used in this analysis were recorded by the *BABAR* detector run by the *BABAR* collaboration. The author contributed to the running of the detector through the taking of general shifts and being the Commissioner of the Electromagnetic Calorimeter Trigger for 15 months. The event reconstruction process described in Chapters 3 and 4 makes use of code developed centrally within *BABAR* as well as more specific pre-selection code developed by the charmless three-body analysis working group with some input from the author. The code for the final selection described in Section 4.3.3 was developed by the author and that for the calculation of the Fisher coefficients (Section 3.5.3) was developed by the author and John Back. The code used for the amplitude analysis was developed by the author, Paul Harrison, John Back and Sian Morgan. The cut optimisation described in Section 4.3.5 was performed by John Back. The amplitude analysis was undertaken jointly with Sian Morgan; specifically the fit to determine the signal and continuum background yields (Section 4.6) and the optimisation of the $K_0^{*0}(1430)$ lineshape (Section 5.5) was the sole work of the author while the optimisation of the $f_0(980)$ lineshape (Section 5.5), and the calculation of the upper limits (Section 5.7.2) were performed by Sian Morgan.

SIGNED: ..... DATE: .....

Contents

Acknowledgements **iii**

Declaration **v**

Introduction **1**

1 Theory **3**

1.1 Introduction 3

1.2 Hadronic Decays of B Mesons 4

1.2.1 Weak Interactions of Hadrons 4

1.2.2 CP Violation in the Standard Model 6

1.2.3 Strong Interactions of Hadrons 13

1.3 Three-body Decay Kinematics 19

1.3.1 The Dalitz Plot 19

1.3.2 Mass 22

1.3.3 Helicity Angle 23

1.3.4 Interference 24
1.3.5 The Light Meson Spectrum 25
1.4 The Decay $B^+ \to K^{*0}(892)\pi^+$ 27
1.4.1 Branching Fraction Predictions 27
1.4.2 *CP* Asymmetry Predictions 29

2 The *BABAR* Experiment **33**
2.1 Introduction 33
2.2 The PEP-II Accelerator 34
2.2.1 Overview 34
2.2.2 The Interaction Region 35
2.2.3 Machine Backgrounds 35
2.2.4 Trickle Injection 37
2.2.5 Performance 38
2.3 The *BABAR* Detector 39
2.3.1 The *BABAR* Co-ordinate System 40
2.4 The Silicon Vertex Tracker (SVT) 42
2.4.1 SVT Physics Requirements 42
2.4.2 SVT Design 42
2.4.3 SVT Performance 45
2.5 The Drift Chamber (DCH) 46
2.5.1 DCH Physics Requirements 46
2.5.2 DCH Design 46

2.5.3 DCH Performance 49
2.6 The Detector of Internally Reflected Cerenkov light (DIRC) 51
2.6.1 DIRC Physics Requirements 51
2.6.2 DIRC Design 52
2.6.3 DIRC Performance 53
2.7 The Electromagnetic Calorimeter (EMC) 54
2.7.1 EMC Physics Requirements 54
2.7.2 EMC Design 55
2.7.3 EMC Performance 57
2.8 The Instrumented Flux Return (IFR) 61
2.8.1 IFR Physics Requirements 61
2.8.2 IFR Design 61
2.8.3 IFR Performance 63
2.9 The Trigger (TRG) 65
2.9.1 Level 1 Trigger (L1T) 66
2.9.2 Level 3 Trigger (L3T) 68
2.10 The Data Acquisition System (DAQ) 69

3 Analysis Techniques **71**

3.1 Introduction 71
3.2 Reconstruction 72
3.2.1 Tracking Algorithms 72
3.2.2 Calorimeter Algorithms 74

3.2.3 Particle Identification (PID) 74
3.2.4 Vertexing of Composite Candidates 77
3.3 Monte Carlo Simulation 78
3.3.1 Efficiency Corrections 79
3.4 B Counting 80
3.5 Discriminating Variables 81
3.5.1 Kinematic Variables 82
3.5.2 Topological Variables 83
3.5.3 Fisher Discriminant 87
3.6 Maximum Likelihood Fitting 91
3.6.1 Error Calculation 92
3.6.2 Extended Maximum Likelihood Fitting 92
3.6.3 Fitting Packages 93

4 Analysis Method **97**

4.1 Introduction 97
4.2 Overview 98
4.3 Event Selection 100
4.3.1 Event Preselection 101
4.3.2 Batch Level Pre-Analysis 101
4.3.3 Final Selection for $B^+ \to K^+\pi^-\pi^+$ 102
4.3.4 Definition of Fitting Regions 104
4.3.5 Selection Optimisation 104

4.4 Efficiency, Self Cross Feed and Migration . . . 107
4.4.1 Efficiency Variation across the Dalitz plot . . . 109
4.4.2 Self Cross Feed . . . 110
4.4.3 Migration . . . 111
4.5 Background Determination . . . 113
4.5.1 $B\overline{B}$ background . . . 114
4.5.2 $q\overline{q}$ background . . . 121
4.6 Determination of Signal and $q\overline{q}$ Background Yields . . . 123
4.7 Dalitz Plot Amplitude Fitting . . . 125
4.7.1 The Likelihood Function . . . 126
4.7.2 Signal Model . . . 127
4.7.3 Efficiency Model . . . 129
4.7.4 Background Model . . . 129
4.8 Numerical Integration . . . 130

5 Analysis Results **133**

5.1 Introduction . . . 133
5.2 Total Rate Results . . . 134
5.2.1 ${}_s\mathcal{P}lots$ . . . 136
5.3 Toy Monte Carlo Tests . . . 138
5.3.1 Multiple Solutions . . . 138
5.3.2 Toy MC Test Results . . . 140
5.4 Full Simulation Monte Carlo Tests . . . 142

5.5 Determination of Lineshape Parameters . . . 143
5.6 Nominal Model Amplitude Fit Results . . . 146
5.7 Alternative Model Amplitude Fits . . . 153
5.7.1 Omission Tests . . . 155
5.7.2 Addition Tests . . . 155
5.8 Systematic Uncertainties . . . 160
5.8.1 Amplitude Fit Uncertainties . . . 160
5.8.2 Branching Fraction Uncertainties . . . 164

6 Discussion and Conclusion **169**

6.1 Introduction . . . 169
6.2 Summary of Results . . . 170
6.3 Implications for Factorisation . . . 172
6.4 S-wave Contributions . . . 174
6.4.1 The $f_0(980)$ . . . 175
6.5 Future Enhancements . . . 177
6.5.1 Fit χ^2 Determination . . . 177
6.5.2 Resolution and Self Cross Feed Effects . . . 178
6.5.3 Combined Amplitude and $m_{\rm ES}$ Fit . . . 179
6.5.4 Combined Charge Fit . . . 179

A Yield Fit PDF Parameters **181**

List of Figures

1.1 The Unitarity Triangle. 8

1.2 Tree and penguin diagrams for the decay $B^0 \to K^+\pi^-$. 10

1.3 Second order weak processes that give rise to $B^0\overline{B}^0$ mixing. 10

1.4 Tree diagram for the decay $B^0 \to J/\psi K^0_S$. 12

1.5 Three diagrams for the decay $B^+ \to \rho^0(770)K^+$. 15

1.6 Illustration of the Dalitz plot 21

1.7 The diagram for the decay $B^+ \to K^{*0}(892)\pi^+$. 28

2.1 Plan view of the PEP-II interaction region. 36

2.2 PEP-II integrated luminosity per month 38

2.3 The *BABAR* Detector. 41

2.4 End on view of the SVT. 43

2.5 Side on view of the SVT. 44

2.6 Side on view of the DCH. 47

2.7 DCH cell layout for the first four superlayers. 48

2.8 Tracking efficiency for the DCH. 49

2.9 dE/dx measurements in the DCH. 50

2.10 Structure and concept of the DIRC. 52

2.11 DIRC K/π separation. 54

2.12 Reconstructed K π mass with and without DIRC PID. 55

2.13 Side on view of the EMC. 56

2.14 Energy resolution of the EMC. 58

2.15 Angular resolution of the EMC. 58

2.16 Electron efficiency and pion misidentification probability. 59

2.17 Mechanical structure of the IFR. 62

2.18 Cross section of an RPC. 62

2.19 Muon efficiency and pion misidentification probability. 64

2.20 Schematic of the *BABAR* DAQ system. 69

3.1 Distribution of the topological variable $|\cos\theta_T|$. 84

3.2 The distribution of the CLEO Cones. 85

3.3 The distribution of the L_0 and L_2 variables. 86

3.4 The distribution of $\cos(\theta_{Bmom})$ and $\cos(\theta_{Bthr})$ 87

3.5 The distribution of $|$`TFlv`$|$. 89

3.6 Distribution of the Fisher discriminant. 90

4.1 ΔE–$m_{\rm ES}$ plane, showing signal strip, sideband and signal box. 105

4.2 Signal significance as a function of Fisher selection. 108

4.3 Efficiency variation across the Dalitz plot. 110

4.4 Efficiency variation, corrected for low statistics bins. 111

4.5 Efficiency variation for B^+ and B^-. 112

4.6 Dalitz distribution of Self Cross Feed Events. 113

4.7 Self Cross Feed distribution for B^+ and B^-. 114

4.8 Migration of truth matched events within the Dalitz plot. 114

4.9 Migration of self cross feed events within the Dalitz plot. 115

4.10 Dalitz plot projections comparing the $B\overline{B}$ subtracted on-peak sideband with off-peak data. 122

4.11 The ratio of the $B\overline{B}$ subtracted on-peak sideband and off-peak data Dalitz projections. 122

4.12 The $m_{\rm ES}$ distribution of $B^+ \to K^+\pi^-\pi^+$ non resonant events. 123

4.13 The $m_{\rm ES}$ distribution of off-peak data events. 124

4.14 The $m_{\rm ES}$ distribution of $B\overline{B}$ background events. 124

4.15 Dalitz plot distribution for continuum ($q\overline{q}$) background events. 130

4.16 Dalitz plot distribution for $B\overline{B}$ background events. 130

5.1 The $m_{\rm ES}$ fit to data. 135

5.2 Signal ${}_s\mathcal{P}lot$ distributions of $m_{K^+\pi^-}$ and $m_{\pi^+\pi^-}$. 137

5.3 Signal ${}_s\mathcal{P}lot$ of the $B^\pm \to K^\pm\pi^\mp\pi^\pm$ Dalitz plot 137

5.4 The $B^\pm \to K^\pm\pi^\mp\pi^\pm$ Dalitz plot 138

5.5 Multiple solutions 139

5.6 Pull distributions for the magnitudes in the 500 toy tests 140

5.7 Pull distributions for the phases in the 500 toy tests 141

5.8 Likelihood curves for the LASS parameter scans. 144

5.9 Likelihood curves for the Flatté parameter scans. 145

5.10 Invariant mass projection plots for the nominal $B^+ \to K^+\pi^-\pi^+$ fit. . 149

5.11 Invariant mass projection plots for the nominal $B^- \to K^-\pi^+\pi^-$ fit. . 150

5.12 Invariant mass regional plots for the nominal $B^+ \to K^+\pi^-\pi^+$ fit. . . 151

5.13 Invariant mass regional plots for the nominal $B^- \to K^-\pi^+\pi^-$ fit. . . 152

5.14 Nominal fit χ^2 for the positive sample. 154

5.15 Nominal fit χ^2 for the negative sample. 154

5.16 Determination of the fit bias 162

6.1 Feynman diagram for $B^+ \to f_0(980)K^+$ 176

List of Tables

1.1 $K^+\pi^-$ Mass Spectrum Summary 26

1.2 $\pi^+\pi^-$ Mass Spectrum Summary 27

1.3 Theoretical predictions of charmless branching fractions 30

1.4 Theoretical predictions of charmless decay *CP* asymmetries 31

2.1 PEP-II Machine Performance Records 39

2.2 Definition of DCT and EMT trigger primitives. 67

4.1 Summary of average selection efficiencies. 106

4.2 Charm B^+B^- background mode details. 117

4.3 Charmless B^+B^- background mode details. 118

4.4 Charm $B^0\overline{B}^0$ background mode details. 119

4.5 Charmless $B^0\overline{B}^0$ background mode details. 120

5.1 The event yields from the 1D fit to $m_{\rm ES}$ 134

5.2 Magnitude and Phase pulls in 500 toy tests 141

5.3 Magnitude and Phase results of fit to full simulation MC 143

5.4 Results of the scans for the Flatté and LASS parameters 145

5.5 Results of the nominal fit to data. 147

5.6 Fit fraction asymmetries 148

5.7 Results of fit to B^+ data with 5 components. 156

5.8 Results of fit to B^- data with 5 components. 157

5.9 Results of fit to B^+ data with 7 components 158

5.10 Results of fit to B^- data with 7 components 159

5.11 Systematic uncertainties from the amplitude fit 163

5.12 Selection requirement efficiency corrections 167

6.1 Summary of branching fraction and A_{CP} results 170

A.1 The signal $m_{\rm ES}$ fit parameters 182

A.2 The $q\overline{q}$ background $m_{\rm ES}$ fit parameters 182

A.3 The $B\overline{B}$ background $m_{\rm ES}$ fit parameters 182

Introduction

Together with colleagues from *BABAR* I have previously analysed the $B^+ \to K^+\pi^-\pi^+$ Dalitz plot using a data sample of $56.4\,\text{fb}^{-1}$. This analysis used a "quasi-two-body" approach — the signal event yield in different regions of the Dalitz plot was determined using a maximum likelihood technique. These yields were then used to calculate branching fractions by considering the possible contributions to each of these regions by different resonant and non resonant modes. Possible interference between all the contributing modes was considered as a systematic error. This analysis was published in Physical Review D [1] and gave the following results:

- $\mathcal{B}(B^+ \to K^{*0}(892)\pi^+) = (15.5 \pm 1.8 \pm 1.1^{+0.6}_{-3.8} \pm 0.9) \times 10^{-6}$
- $\mathcal{B}(B^+ \to$"higher K^{*0}"π^+, $K^{*0} \to K^+\pi^-) = (25.1 \pm 2.0 \pm 2.9^{+9.4}_{-0.5} \pm 4.9) \times 10^{-6}$
- $\mathcal{B}(B^+ \to \overline{D}^0\pi^+$, $\overline{D}^0 \to K^+\pi^-) = (184.6 \pm 3.2 \pm 9.7) \times 10^{-6}$
- $\mathcal{B}(B^+ \to \rho^0(770)K^+) = (3.9 \pm 1.2^{+0.3+0.3}_{-0.6-3.2} \pm 1.2) \times 10^{-6}$
- $\mathcal{B}(B^+ \to f_0(980)K^+$, $f_0(980) \to \pi^+\pi^-) = (9.2 \pm 1.2 \pm 0.6^{+1.2}_{-1.9} \pm 1.6) \times 10^{-6}$
- $\mathcal{B}(B^+ \to$"higher f"K^+, $f \to \pi^+\pi^- = (3.2 \pm 1.2 \pm 0.5^{+5.8}_{-2.4} \pm 1.5) \times 10^{-6}$
- $\mathcal{B}(B^+ \to K^+\pi^-\pi^+$ non resonant$) = (5.2 \pm 1.9^{+0.8+3.3}_{-1.8-7.5} \pm 6.4) \times 10^{-6}$
- $\mathcal{B}(B^+ \to \chi_{c0}K^+$, $\chi_{c0} \to \pi^+\pi^-) = (1.5 \pm 0.4 \pm 0.1) \times 10^{-6}$

This thesis presents the next step in the process, which is an amplitude level analysis. This analysis of the $B^+ \to K^+\pi^-\pi^+$ Dalitz Plot is the first such analysis performed

at the *BABAR* experiment. I present measurements of the fit fractions and phases of the contributing amplitudes in both the B^+ and B^- samples. Combining these results allows determination of the branching fractions of each of the decays, as well as, potentially, the Charge-Parity (CP) asymmetries and the weak and strong phases for each contributing decay mode.

The need for a full amplitude level Dalitz plot analysis has become increasingly clear as the analysis of many B decay modes requires a detailed understanding of the interference of intermediate states. For example the measurement of the Unitarity Triangle angle β (Section 1.2.2.1) in the charmless mode $B^0 \to K^+K^-K^0_S$ requires that the CP-odd and CP-even components of the Dalitz plot be well separated. Without knowledge of the interferences any measurements made of a 3-body decay will be subject to large systematic uncertainties. However, a full Dalitz plot analysis requires large statistics and is technically difficult, and as such is only becoming feasible for a handful of modes, such as $B^+ \to K^+\pi^-\pi^+$ now that the *BABAR* data set exceeds $150\,\mathrm{fb}^{-1}$.

As seen from the above results, the $B^+ \to K^+\pi^-\pi^+$ Dalitz Plot has many possible contributions including: a non resonant component, $K^{*0}(892)\pi^+$, $f_0(980)K^+$ and $\rho^0(770)K^+$. These contributions form overlapping bands of various widths and shapes in the Dalitz Plot, the greater the overlap, the stronger the interference is between the channels. As mentioned, previous measurements [1] were performed at the intensity level, and as such treated the interferences between the various contributions as a systematic error. The amplitude analysis of the Dalitz plot takes into account, and indeed quantifies, these interferences.

1

Theory

1.1 Introduction

In this chapter the various aspects of theories that affect the decays under consideration in this analysis will be examined. Hadronic B decays are governed by the weak interaction, which is theoretically very well understood and is easily calculable. However, the situation is complicated by the effects of the strong interaction since both the initial and final states are hadronic and can have interactions via soft gluons.

Firstly the weak interaction in the Standard Model will be examined and it will be demonstrated how CP violation can occur within this framework. Then methods

of approximating the quantum chromodynamic (QCD) effects will be presented, namely the Operator Product Expansion and Factorisation. These can be used to make predictions of branching fractions and *CP* asymmetries of rare hadronic B decays.

Next there will be a discussion of the kinematics of three-body decays focusing on the concept of the Dalitz Plot and how it can be used to probe the interference between three body decays. Finally it will be shown how each of these theories can be applied to the example decay $B^+ \to K^{*0}(892)\pi^+$ and what predictions can be made about its decay rate and possible *CP* violation. Predictions for the decay $B^+ \to \rho^0(770)K^+$ will also be presented.

1.2 Hadronic Decays of B Mesons

B mesons decay via the weak interaction with an average lifetime of around 1.5 ps [2]. The hadronic initial and final states of the decays in this analysis mean that QCD effects must also be considered in theoretical calculations. In this section the theory of the weak interactions of the quarks within the Standard Model will be examined and it will be seen how this gives rise to *CP* violation, before discussing methods that can approximate the QCD effects.

1.2.1 Weak Interactions of Hadrons

In the Standard Model the fundamental particles of matter are the quarks and leptons. There are three generations of these particles and the weak interaction couples to their left-handed versions. The left-handed quarks are arranged in $SU(2)_L$ doublets, as in Eq. (1.1); where the primes refer to the fact that the weak eigenstates of the down-type quarks, denoted (d', s', b'), are not necessarily equal to the mass

eigenstates, denoted (d, s, b), but are a linear superposition of them.

$$\begin{pmatrix} u \\ d' \end{pmatrix}_L, \quad \begin{pmatrix} c \\ s' \end{pmatrix}_L, \quad \begin{pmatrix} t \\ b' \end{pmatrix}_L \tag{1.1}$$

The matrix that transforms the mass eigenstates into the weak eigenstates is the Cabibbo-Kobayashi-Maskawa (CKM) matrix, denoted $V_{\rm CKM}$, which must be unitary ($VV^\dagger = 1$) [3]. The charged current weak interactions are mediated by massive charged gauge bosons $W^\pm$ and are described by the Lagrangian in Eq. (1.2); where g is the weak coupling constant, $W_\mu^\dagger$ are the weak gauge bosons and h.c. indicates the hermitian conjugate of the first term.

$$\mathcal{L}_{\rm CC} = -\frac{g}{\sqrt{2}} \left(\overline{u}_L, \overline{c}_L, \overline{t}_L\right) \gamma^\mu V_{\rm CKM} \begin{pmatrix} d_L \\ s_L \\ b_L \end{pmatrix} W_\mu^\dagger + \text{h.c.} \tag{1.2}$$

The condition of unitarity that is imposed on the CKM matrix, combined with the requirement that any phases must be non-trivial (*i.e.* cannot be set to zero with a redefinition of the fields) means that the CKM matrix can be completely determined by four quantities - three real angles and one remaining non-trivial phase. The form of the CKM matrix is shown in Eq. (1.3), where it is presented in the "standard parameterisation" [4].

$$\begin{aligned} V_{\rm CKM} &= \begin{pmatrix} V_{ud} & V_{us} & V_{ub} \\ V_{cd} & V_{cs} & V_{cb} \\ V_{td} & V_{ts} & V_{tb} \end{pmatrix} \\ &= \begin{pmatrix} c_{12}c_{13} & s_{12}c_{13} & s_{13}e^{-i\delta} \\ -s_{12}c_{23} - c_{12}s_{23}s_{13}e^{i\delta} & c_{12}c_{23} - s_{12}s_{23}s_{13}e^{i\delta} & s_{23}c_{13} \\ s_{12}s_{23} - c_{12}c_{23}s_{13}e^{i\delta} & -c_{12}s_{23} - s_{12}c_{23}s_{13}e^{i\delta} & c_{23}c_{13} \end{pmatrix} \end{aligned} \tag{1.3}$$

where $s_{ij} = \sin\theta_{ij}$, $c_{ij} = \cos\theta_{ij}$. $\cos\theta_{12}$, $\cos\theta_{13}$, $\cos\theta_{23}$ are the three real angles and δ is the non-trivial phase, which is the sole source of *CP* violation in the Standard Model.[1]

[1]There is in fact one further potential source in the QCD Lagrangian, but the contribution from this term is constrained to be very small by measurements of the neutron's electric dipole moments [5].

An alternative form of the CKM matrix developed by Wolfenstein [6] can be seen in Eq. (1.4). It is an approximate form and makes use of experimental indications of the hierarchy of the matrix elements, expanding in powers of the element $\lambda = V_{us} \approx 0.22$ and making the definitions $V_{cb} = A\lambda^2$ and $V_{ub} = A\lambda^3(\rho - i\eta)$, where A, ρ and η are all $\mathcal{O}(1)$.

$$V_{\mathrm{CKM}} \approx \begin{pmatrix} 1 - \frac{\lambda^2}{2} & \lambda & A\lambda^3(\rho - i\eta) \\ -\lambda & 1 - \frac{\lambda^2}{2} & A\lambda^2 \\ A\lambda^3(1 - \rho - i\eta) & -A\lambda^2 & 1 \end{pmatrix} + \mathcal{O}(\lambda^4) \tag{1.4}$$

The quantities λ and A are well determined experimentally, from the semi-leptonic decays of kaons and B-mesons respectively, but ρ and η (which correspond to the phase δ) are not and hence it is one of the goals of *BABAR* to determine these quantities through a variety of measurements and methods.

1.2.2 *CP* Violation in the Standard Model

There are three discrete symmetries in the Standard Model in addition to the continuous Lorentz and gauge transformations. Parity (P) and time reversal (T) are space-time transformations that cause $\vec{x} \to -\vec{x}$ and $t \to -t$ respectively. Both of these operators have the effect of reversing the momentum vector whilst leaving spin unchanged. Charge conjugation (C) does not affect space-time quantities but instead changes particles into anti-particles by changing the internal quantum numbers of the particle. In a quantum field theory formed with very general assumptions any Hamiltonian operator (H) which is invariant under Lorentz transformations will be invariant under the combined operation *CPT* [7]. Since *CPT* is conserved *CP* violation also implies T violation. T transforms e^{-iEt} to e^{iEt} and transforms the Hamiltonian H into its complex conjugate H^*. If $H \neq H^*$ then T and hence *CP* is violated [8]. It is for this reason that the complex phase of the CKM matrix is a potential source of *CP* violation. If the angles θ_{ij} in the parameterisation of Eq. (1.3) are not 0 or $\pi/2$ and the phase δ is not 0 or π then *CP* is violated. These conditions can be combined into a single term, which must be non-zero, called the Jarlskog

invariant [9]. This is shown in Eq. (1.5), which is written in both the Eq. (1.3) parameterisation and that of Eq. (1.4).

$$J = c_{12}c_{23}c_{13}^2 s_{12}s_{23}s_{13}\sin\delta \approx A^2\eta\lambda^6 \tag{1.5}$$

Parity was seen to be maximally violated in weak decays in 1957 [10]. Apart from the apparent matter antimatter asymmetry of the universe, *CP* violation was first observed in the $K^0\overline{K}^0$ system in 1964 [11]. Until 2001 this was the only system in which *CP* violation was observed but then *BABAR* made the first observation of *CP* violation in the $B^0\overline{B}^0$ system [12]. Even so *CP* violation remains one of the least well investigated areas of the Standard Model.

CP violation can occur in three different forms in B decays: direct, which occurs in the decay process; indirect, which occurs in the mixing of the neutral B mesons; and that arising from the interference between the decay and mixing processes. These three forms will be examined following a more detailed examination of *CP* violation within the Standard Model.

1.2.2.1 The Unitarity Triangle

The condition of unitarity on the CKM matrix results in equations of the form

$$\sum_i V_{ij}V_{ik}^* = 0 \quad (j \neq k) \tag{1.6}$$

There are six such equations, each of which represents a triangle in the complex plane. Two of these equations, have sides of similar magnitude and also contains some of the least well constrained CKM matrix elements:

$$V_{ud}V_{ub}^* + V_{cd}V_{cb}^* + V_{td}V_{tb}^* = 0 \tag{1.7}$$

$$V_{ud}V_{td}^* + V_{us}V_{ts}^* + V_{ub}V_{tb}^* = 0. \tag{1.8}$$

The first of these triangles, rescaled by $\frac{1}{|V_{cd}V_{cb}^*|}$, is illustrated in Figure 1.1. The vertex of the triangle is given by $\bar{\rho}, \bar{\eta}$, which are related to the original ρ and η of the

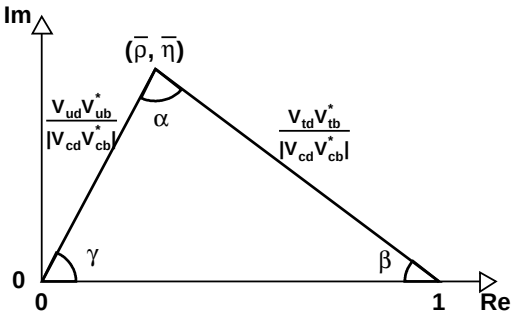

Figure 1.1: *The Unitarity Triangle.*

Wolfenstein parameterisation by Eq. (1.9), which is calculated from an extension of this parameterisation to $\mathcal{O}(\lambda^5)$. Since $\lambda \approx 0.22$, $\bar{\rho} = \rho$ and $\bar{\eta} = \eta$ to within 3%.

$$\bar{\rho} = \rho\left(1 - \lambda^2/2\right), \quad \bar{\eta} = \eta\left(1 - \lambda^2/2\right) \tag{1.9}$$

The internal angles of the triangle are given by

$$\alpha \equiv \arg\left[-\frac{V_{td}V_{tb}^*}{V_{ud}V_{ub}^*}\right], \quad \beta \equiv \arg\left[-\frac{V_{cd}V_{cb}^*}{V_{td}V_{tb}^*}\right], \quad \gamma \equiv \arg\left[-\frac{V_{ud}V_{ub}^*}{V_{cd}V_{cb}^*}\right] \tag{1.10}$$

Additionally, the bottom side of the triangle does have a small phase from $|V_{cd}|$ that means that it does not lie exactly on the real axis and so the whole triangle can be rotated about the origin in Figure 1.1.

The area of the Unitarity Triangle is found to be $J/2$ (Eq. (1.5)) and so the condition for *CP* violation becomes that the triangle has non-zero area. Measurement of the angles and sides of the Unitarity Triangle is one of the main physics goals of *BABAR*. It is important that these measurements be made through as many independent decay modes as possible in order to attempt to over-constrain the triangle and probe for contributions from physics beyond the Standard Model. Such contributions could, for example, cause disagreement between measurements in different processes of what, in the Standard Model, should be the same angle.

1.2.2.2 *CP* Violation in Decay

Direct *CP* violation occurs when the amplitude for a certain decay process and its *CP* conjugate process are not equal. It has been observed in K decays [13, 14] and very recently for the first time in B decays [15]. It is also the only type of *CP* violation possible in charged B decays such as those in this analysis.

Consider the decay $B \to f$, where f is any final state, and its *CP* conjugate $\overline{B} \to \bar{f}$. The amplitudes for these decays can be written

$$A_f = \langle f \,|H|\, B\rangle = \sum_j A_j e^{i(\delta_j+\phi_j)}, \quad \bar{A}_{\bar{f}} = \left\langle \bar{f} \,|H|\, \overline{B}\right\rangle = \sum_j A_j e^{i(\delta_j-\phi_j)} \tag{1.11}$$

where A_j, δ_j, and ϕ_j are the amplitude, strong (or *CP*-conserving) phase and weak (or *CP*-violating) phase of a contributing process. The condition for *CP* violation is that $\left|\bar{A}_{\bar{f}}\right|^2 \neq |A_f|^2$. In order for this condition to be met there must be contributions from at least two processes of similar magnitude which also have different weak and strong phases. These two requirements indicate that charmless B decays are excellent candidates for potentially observing *CP* violation in decay. Most charmless decay modes have contributions from both weak tree level processes as well as penguin diagrams, which involve gluon exchange. Both of these processes are illustrated in Figure 1.2 for the example case of $B^0 \to K^+\pi^-$. Charmless decays that proceed only via penguin diagrams can also give rise to *CP* violation in decay since the penguin diagram shown in Figure 1.2 is actually three diagrams, each of which has a different quark in the loop. Each of these diagrams may have different weak and strong phases.

In order to cleanly observe direct *CP* violation it is desirable to avoid the effects of neutral meson mixing (Section 1.2.2.3) and so "self-tagged" decay modes should be used. These are where the flavour of the B meson that decays is apparent from the final state particles. All charged B decays are self-tagging. For such decays an

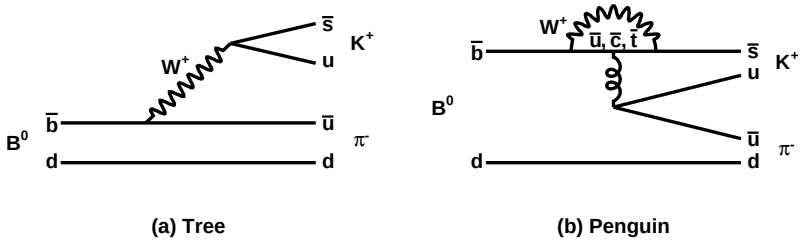

Figure 1.2: *Tree and penguin diagrams for the decay* $B^0 \to K^+\pi^-$.

observed asymmetry can be rewritten in terms of decay rates (Γ) as

$$A_{CP} = \frac{\Gamma(\overline{B} \to \bar{f}) - \Gamma(B \to f)}{\Gamma(\overline{B} \to \bar{f}) + \Gamma(B \to f)} = \frac{\left|\bar{A}_{\bar{f}}/A_f\right|^2 - 1}{\left|\bar{A}_{\bar{f}}/A_f\right|^2 + 1} \tag{1.12}$$

1.2.2.3 *CP* Violation in Mixing

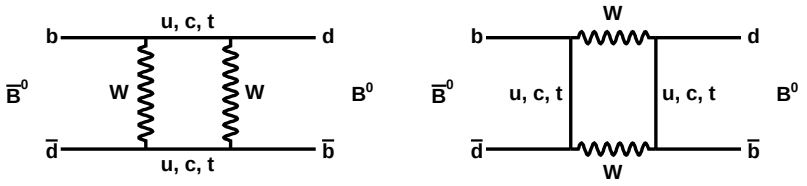

Figure 1.3: *Second order weak processes that give rise to* $B^0\overline{B}^0$ *mixing.*

The neutral B mesons can mix via second order weak processes such as those shown in Figure 1.3, where the t quark contribution dominates due to its considerably larger mass [8]. The B^0 and $\overline{B}^0$ mesons, which have definite quark content, are dubbed the *flavour eigenstates*, whilst the eigenstates of the propagation Hamiltonian are dubbed the *mass eigenstates*. Denoted by B_H and B_L, these mass eigenstates are linear superpositions of the flavour eigenstates

$$|B_L\rangle \;=\; p\left|B^0\right\rangle + q\left|\overline{B}^0\right\rangle$$

$$|B_H\rangle \;=\; p\left|B^0\right\rangle - q\left|\overline{B}^0\right\rangle \tag{1.13}$$

where p and q are complex coefficients that satisfy the condition $|p|^2 + |q|^2 = 1$.

The time evolution of an arbitrary linear combination of the flavour eigenstates

$$a\left|B^0\right\rangle + b\left|\overline{B}^0\right\rangle \tag{1.14}$$

is described by the time dependent Schrödinger equation

$$i\frac{d}{dt}\begin{pmatrix} a \\ b \end{pmatrix} = H\begin{pmatrix} a \\ b \end{pmatrix} \equiv \begin{pmatrix} H_{11} & H_{12} \\ H_{21} & H_{22} \end{pmatrix}\begin{pmatrix} a \\ b \end{pmatrix} \equiv \left(M - \frac{i}{2}\Gamma\right)\begin{pmatrix} a \\ b \end{pmatrix} \tag{1.15}$$

where M and Γ are 2×2 Hermitian matrices that originate from mixing and decay respectively.

Invariance under *CPT* means that H_{11} and H_{22} are equal. The remaining elements, H_{12} and H_{21} are the amplitudes for mixing and as such if they are zero there is no $B^0\overline{B}^0$ mixing. Furthermore, *CP* symmetry requires that $H_{12}^* = H_{21}$, which implies that the mass eigenstates are also eigenstates of the *CP* operator and that $|p| = |q|$. Consequently if $\left|\frac{p}{q}\right| \neq 1$ then there is *CP* violation in mixing.

The experimental finding that $\Delta\Gamma_B \ll \Delta m_B$ [2], where $\Delta\Gamma_B = \Gamma_H - \Gamma_L$ and $\Delta m_B = m_H - m_L$, can be used to make a leading order approximation of the value of $\left|\frac{p}{q}\right|$, which is found to be unity [8]. *CP* violation in mixing is expected to be small since second order corrections to this approximation should be $< 1\%$.

1.2.2.4 *CP* Violation in Interference Between Mixing and Decay

The final form of *CP* violation arises from interference between the mixing and decay processes. This can be observed in decays of B^0 and $\overline{B}^0$ mesons to the same final state, which must therefore be a *CP* eigenstate ($f = \bar{f}$).

Defining A_f as the amplitude for the decay $B^0 \to f$ and $\bar{A}_f$ as the amplitude for the decay $\overline{B}^0 \to f$, the quantity

$$\lambda_f = \frac{q}{p}\frac{\bar{A}_f}{A_f} \tag{1.16}$$

must be equal to unity if *CP* is conserved. Furthermore the time-dependent asymmetry is found to be

$$\begin{aligned} A_{CP}(t) &= \frac{\Gamma(B \to f)(t) - \Gamma(\overline{B} \to f)(t)}{\Gamma(B \to f)(t) + \Gamma(\overline{B} \to f)(t)} \\ &= \left(\frac{1 - |\lambda_f|^2}{1 + |\lambda_f|^2}\right) \cos\Delta m_B t - \left(\frac{2\mathrm{Im}\,(\lambda_f)}{1 + |\lambda_f|^2}\right) \sin\Delta m_B t \end{aligned} \tag{1.17}$$

The cosine term arises from direct *CP* violation and vanishes if $|\lambda_f| = 1$, since together with the fact that $\left|\frac{p}{q}\right| \approx 1$ it implies that $\bar{A}_f = A_f$. The sine term is due to the interference of decays with and without mixing and vanishes if $\mathrm{Im}\,(\lambda_f) = 0$.

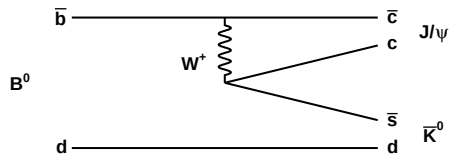

Figure 1.4: *Tree diagram for the decay $B^0 \to J/\psi\, K^0_S$.*

The decay channel $B^0 \to J/\psi\, K^0_S$ is an example of a decay to a *CP* eigenstate. It proceeds mainly via the tree diagram in Figure 1.4 and there is negligible expected *CP* violation in decay. As such the approximation $|\lambda_f| = 1$ can be made causing the cosine term in Eq. (1.17) to vanish. The sine term reduces to $\mathrm{Im}\left(\lambda_{J/\psi\, K^0_S}\right)$, which is built up from three terms: one from $B^0\overline{B}^0$ mixing; one from the ratio $\frac{\bar{A}_f}{A_f}$; and one from $K^0\overline{K}^0$ mixing. Hence

$$\lambda_{J/\psi\, K^0_S} = -\left(\frac{V^*_{tb}V_{td}}{V_{tb}V^*_{td}}\right)\left(\frac{V^*_{cs}V_{cb}}{V_{cs}V^*_{cb}}\right)\left(\frac{V^*_{cd}V_{cs}}{V_{cd}V^*_{cs}}\right) \tag{1.18}$$

$$\mathrm{Im}\left(\lambda_{J/\psi\, K^0_S}\right) = \sin 2\beta \tag{1.19}$$

$$A_{CP}(t) = \sin 2\beta \sin\Delta m_B t \tag{1.20}$$

The amplitude of this asymmetry, and hence $\sin 2\beta$, can be measured using events where one B is reconstructed in its decay to $J/\psi\, K^0_S$ and the other B is "flavour

tagged". Flavour tagging involves examining the charge of certain final state particles in order to determine the flavour of the B meson. The decay products that are used in this process include electrons and muons from semi-leptonic decays of the B or of a secondary D meson, kaons from hadronic decays and soft pions from secondary decays of D^* mesons. Accurate determination of the mis-tag rate, the probability of assigning the wrong flavour to a given B, is essential since mis-tagging will reduce the amplitude of the asymmetry and hence alter the measured value of $\sin 2\beta$. Measurements of the $B^0\overline{B}^0$ mixing rate through decays to flavour eigenstates are used to determine the mis-tag rate since the amplitude of these oscillations should be unity with perfect tag performance. Since the tagging method uses information from the rest of the event its performance should be independent of final state of the reconstructed B.

The *BABAR* and Belle collaboration results for $\sin 2\beta$ use a combination of charmonium modes including $J/\psi\, K^0_S$. The results presented at the ICHEP 2004 conference were as follows, where the first error is statistical and the second is systematic [16,17]:

- $\sin 2\beta = 0.722 \pm 0.040 \pm 0.023$ – *BABAR*
- $\sin 2\beta = 0.728 \pm 0.056 \pm 0.023$ – Belle

1.2.3 Strong Interactions of Hadrons

The relatively simple weak interactions are complicated by radiative corrections, which stem from gluons being emitted and absorbed. These gluons can have a range of momenta and greatly complicate the calculations of cross sections. In this section we will examine the methods that can be employed to estimate these QCD effects in hadronic B decays in order to make predictions of branching fractions and CP asymmetries.

1.2.3.1 The Operator Product Expansion (OPE)

The OPE attempts to separate the non-perturbative long distance effects from the calculable short distance ones, thereby producing an *effective* theory [18]. This is achieved by means of an expansion of the decay amplitude in a small parameter k^2/m_W^2, where k is the momentum transfer through the weak gauge boson propagator, W, which itself has mass m_W. This expansion relies on the condition

$$k < m_b \ll m_W \tag{1.21}$$

where m_b is the mass of the b quark.

Consider the decay $B^+ \to \rho^0(770)K^+$, which at the tree level proceeds via the diagram in Figure 1.5 (a). The amplitude for this diagram is

$$\frac{G_F}{\sqrt{2}} V_{ub}V_{us}^* \left(b^\dagger \gamma^\mu \gamma_L u\right)\left(u^\dagger \gamma_\mu \gamma_L s\right) \frac{m_W^2}{k^2 - m_W^2} \tag{1.22}$$

where γ_L is used to denote $(1-\gamma_5)$ and $\frac{G_F}{\sqrt{2}} = \frac{g^2}{8m_W^2}$. In the OPE this non-local product of currents can be expanded into an infinite series of local operators

$$\begin{aligned} & -\frac{G_F}{\sqrt{2}} V_{ub}V_{us}^* \left(b^\dagger \gamma^\mu \gamma_L u\right)\left(u^\dagger \gamma_\mu \gamma_L s\right)\left[1 + \frac{k^2}{m_W^2} + \cdots\right] \\ \approx\ & -\frac{G_F}{\sqrt{2}} V_{ub}V_{us}^* \left(b^\dagger \gamma^\mu \gamma_L u\right)\left(u^\dagger \gamma_\mu \gamma_L s\right) = -\frac{G_F}{\sqrt{2}} V_{ub}V_{us}^* Q_1 \end{aligned} \tag{1.23}$$

Since k is at most m_b and $m_b^2/m_W^2 \approx 10^{-3}$ all but the leading term can safely be neglected as corrections to the approximation.

The W-boson has thus been removed as a degree of freedom from the theory leaving a form that resembles the Fermi theory of weak interactions. This procedure is sometimes referred to as "integrating out" the degree of freedom, in reference to its formal path-integral derivation.

Consider now the QCD corrections to the decay $B^+ \to \rho^0(770)K^+$. The simplest case is illustrated in Figure 1.5 (b). The gluons complicate the situation because they carry colour, mixing the colour indices of the quarks and generating a new

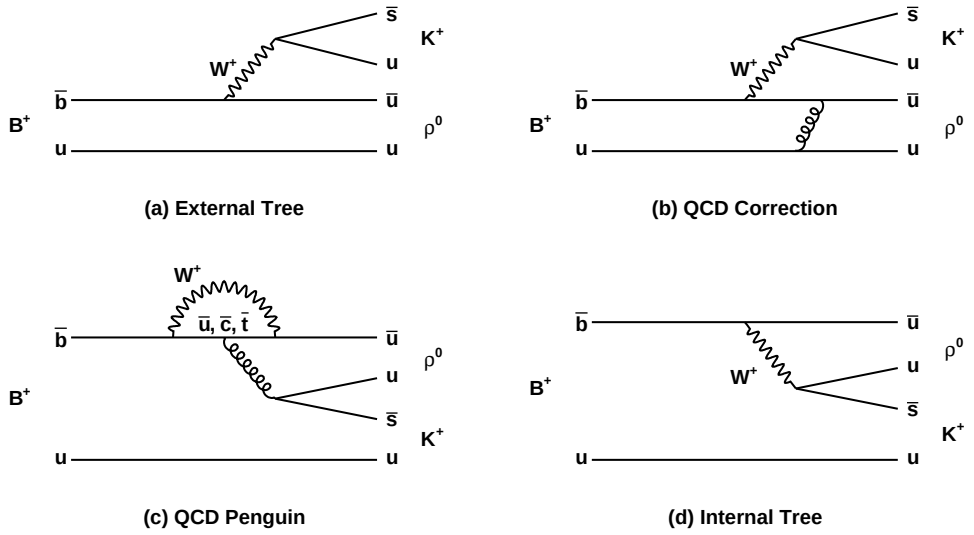

Figure 1.5: *(a) External tree diagram for the decay $B^+ \to \rho^0(770)K^+$, (b) a typical QCD correction, (c) penguin diagram, (d) internal tree diagram.*

operator

$$\sum_{a=1}^{8} \left(b_w^\dagger \gamma^\mu \gamma_L \lambda^a_{wz} u_z\right) \left(u_y^\dagger \gamma_\mu \gamma_L \lambda^a_{yx} s_x\right) \tag{1.24}$$

where λ^a are the Gell-Mann matrices and w, x, y and z are the colour indices. Performing a Fierz [19] transformation on this operator shows it to be a combination of the operator in Eq. (1.23) and

$$Q_2 = \left(b_x^\dagger \gamma^\mu \gamma_L u_y\right) \left(u_y^\dagger \gamma_\mu \gamma_L s_x\right) \tag{1.25}$$

Additionally the gluons can transfer momentum between the quarks in the initial and final states. Where the gluon momentum is large, so called "short distance" corrections, perturbation theory can be applied due to the asymptotic freedom of QCD. However, this requires the introduction of a renormalisation scale μ to the operators. Since the amplitude cannot have a dependence on μ the scale dependence must be cancelled in μ dependent coefficients, called Wilson coefficients, $C_n(\mu)$. The Wilson coefficients are computed by matching the standard model and the effective theory at a scale $\mu \sim m_W$, which yields $C_n(m_W)$. The perturbative evolution of

the coefficients down to the scale m_b is then achieved by using the renormalisation group to sum the large logarithms that occur.

The tree level effective Hamiltonian that takes QCD effects into account requires two current-current operators Q_1 and Q_2, each multiplied by Wilson coefficients

$$\mathcal{H}_{\text{eff}} = \frac{G_F}{\sqrt{2}} V_{ub} V_{us}^* \left(C_1(\mu) Q_1(\mu) + C_2(\mu) Q_2(\mu) \right) + \text{h.c.} \tag{1.26}$$

Four further operators in the effective Hamiltonian may arise from diagrams such as Figure 1.5 (c), which are known as QCD "penguin" diagrams, where the CKM factor in the Hamiltonian depends on which quark is present in the loop. The penguin operators differ from Q_1 and Q_2 in that the gluon coupling has both a left and right handed part and that there is a sum over the the possible $q\overline{q}$ pairs that the gluon may produce. Defining $\gamma_R = (1 + \gamma_5)$, we now have the following six operators

$$\begin{aligned}
Q_1 &= \left(b_x^\dagger \gamma^\mu \gamma_L u_x \right) \left(u_y^\dagger \gamma_\mu \gamma_L s_y \right) \\
Q_2 &= \left(b_x^\dagger \gamma^\mu \gamma_L u_y \right) \left(u_y^\dagger \gamma_\mu \gamma_L s_x \right) \\
Q_3 &= \left(b_x^\dagger \gamma^\mu \gamma_L s_x \right) \sum_q \left(q_y^\dagger \gamma_\mu \gamma_L q_y \right) \\
Q_4 &= \left(b_x^\dagger \gamma^\mu \gamma_L s_y \right) \sum_q \left(q_y^\dagger \gamma_\mu \gamma_L q_x \right) \\
Q_5 &= \left(b_x^\dagger \gamma^\mu \gamma_L s_x \right) \sum_q \left(q_y^\dagger \gamma_\mu \gamma_R q_y \right) \\
Q_6 &= \left(b_x^\dagger \gamma^\mu \gamma_L s_y \right) \sum_q \left(q_y^\dagger \gamma_\mu \gamma_R q_x \right)
\end{aligned} \tag{1.27}$$

There are also contributing operators from *e.g.* electroweak penguins and annihilation diagrams but they will be suppressed with respect to the significant tree and QCD penguin diagrams in the decay modes under consideration here.

By using the OPE the calculable short distance contributions have been separated into the Wilson coefficients. The long distance, low momentum, QCD effects are contained in the operators. The next section discusses a method of approximating these effects.

1.2.3.2 Factorisation

The previous section has shown how the calculable effects can be contained in the Wilson coefficients and that the low momentum effects are swept into the hadronic matrix elements. Theoretical work on performing calculations of these elements using lattice QCD techniques is making progress but has not nearly reached the stage where calculations can be made for the decays considered here. We will examine here the approximation approach known as Factorisation. For a more detailed review of this subject see for example [20].

Factorisation states that a matrix element of the form

$$\left\langle \rho^0 K^+ \left| Q_n \right| B^+ \right\rangle \tag{1.28}$$

can be expressed as a product of two elements such as

$$\left\langle K^+ \left| J_n^1 \right| 0 \right\rangle \left\langle \rho^0 \left| J_n^2 \right| B^+ \right\rangle \tag{1.29}$$

or

$$\left\langle \rho^0 \left| J_n^1 \right| 0 \right\rangle \left\langle K^+ \left| J_n^2 \right| B^+ \right\rangle \tag{1.30}$$

Factorisation assumes that soft gluons are not exchanged between quarks in different elements. This is quite a reasonable assumption in charmless B decays since the quarks are produced with sufficient energy that they are unlikely to interact with long wavelength gluons.

Currents such as $J_n^{1,2}$ can be written as products of experimentally determined quantities, such as form factors and decay rates. The constraints are that the currents must have the correct flavour and colour content for the hadrons under consideration. Where necessary Fierz transformations are used to reorder the quarks.

There are two possible tree diagrams for the decay $B^+ \to \rho^0(770)K^+$, the external tree in Figure 1.5 (a) and the internal tree in Figure 1.5 (d). The operators Q_1 and Q_2 are tree level operators and can contribute to both of these diagrams. The

contribution of Q_1 to the external tree is given by the factorisation

$$\begin{aligned} & \left\langle \rho^0 K^+ \left| \left(u_x^\dagger \gamma^\mu \gamma_L s_x\right) \left(b_y^\dagger \gamma_\mu \gamma_L u_y\right) \right| B^+ \right\rangle \\ = & \left\langle K^+ \left| \left(u_x^\dagger \gamma^\mu \gamma_L s_x\right) \right| 0 \right\rangle \left\langle \rho^0 \left| \left(b_y^\dagger \gamma_\mu \gamma_L u_y\right) \right| B^+ \right\rangle \end{aligned} \tag{1.31}$$

The contribution of Q_1 to the internal tree requires a Fierz transformation and is given by

$$\begin{aligned} & \left\langle \rho^0 K^+ \left| \left(u_x^\dagger \gamma^\mu \gamma_L s_x\right) \left(b_y^\dagger \gamma_\mu \gamma_L u_y\right) \right| B^+ \right\rangle \\ = & \left\langle \rho^0 K^+ \left| \left(u_x^\dagger \gamma^\mu \gamma_L u_y\right) \left(b_y^\dagger \gamma_\mu \gamma_L s_x\right) \right| B^+ \right\rangle \\ = & \left\langle \rho^0 \left| \left(u_x^\dagger \gamma^\mu \gamma_L u_y\right) \right| 0 \right\rangle \left\langle K^+ \left| \left(b_y^\dagger \gamma_\mu \gamma_L s_x\right) \right| B^+ \right\rangle \end{aligned} \tag{1.32}$$

Colour singlet mesons can only be produced by Eq. (1.32) in the case that $x = y$ and so is suppressed with respect to Eq. (1.31) by a colour factor, $\frac{1}{N_C}$, where $N_C = 3$ is the number of colours. The contributions of Q_2 are the same factorised amplitudes but the $\frac{1}{N_C}$ suppression acts on the external tree.

The penguin operators Q_3 to Q_5 behave in much the same way as the tree operators but Q_6 is sightly different. Applying the Fierz transformation gives

$$\left(b_x^\dagger \gamma^\mu \gamma_L s_y\right) \sum_q \left(q_y^\dagger \gamma_\mu \gamma_R q_x\right) = -2 \sum_q \left(b_x^\dagger \gamma_R q_x\right) \left(q_y^\dagger \gamma_L s_y\right) \tag{1.33}$$

This reordering has removed the γ_μ and created a scalar operator. Acting on the scalar quantities $|0\rangle$ and $|B\rangle$ this operator cannot produce a vector meson and as such will not take part in the decay modes $B^+ \to \rho^0(770)K^+$ or $B^+ \to K^{*0}(892)\pi^+$. It may however play a role in the decays $B^+ \to K_0^{*0}(1430)\pi^+$ and $B^+ \to f_0(980)K^+$.

Defining new coefficients

$$\begin{aligned} a_n &= C_n + \frac{1}{N_C} C_{n+1} \quad i = \text{odd} \\ a_n &= C_n + \frac{1}{N_C} C_{n-1} \quad i = \text{even} \end{aligned} \tag{1.34}$$

and operators

$$O_1 = \left\langle h_1 \left| \left(b^\dagger \gamma^\mu \gamma_L u\right) \right| B \right\rangle \left\langle h_2 \left| \left(u^\dagger \gamma_\mu \gamma_L q\right) \right| 0 \right\rangle \tag{1.35}$$

$$
\begin{aligned}
O_2 &= \left\langle h_1 \left| \left(b^\dagger \gamma^\mu \gamma_L q\right) \right| B \right\rangle \left\langle h_2 \left| \left(u^\dagger \gamma_\mu \gamma_L u\right) \right| 0 \right\rangle \\
O_3 &= \left\langle h_1 \left| \left(b^\dagger \gamma^\mu \gamma_L q\right) \right| B \right\rangle \left\langle h_2 \left| \sum_{q'} \left(q'^{\,\dagger} \gamma_\mu \gamma_L q'\right) \right| 0 \right\rangle \\
O_4 &= \left\langle h_1 \left| \left(b^\dagger \gamma^\mu \gamma_L q'\right) \right| B \right\rangle \left\langle h_2 \left| \sum_{q'} \left(q'^{\,\dagger} \gamma_\mu \gamma_L q\right) \right| 0 \right\rangle \\
O_5 &= \left\langle h_1 \left| \left(b^\dagger \gamma^\mu \gamma_L q\right) \right| B \right\rangle \left\langle h_2 \left| \sum_{q'} \left(q'^{\,\dagger} \gamma_\mu \gamma_R q'\right) \right| 0 \right\rangle \\
O_6 &= -2 \left\langle h_1 \left| \left(b^\dagger \gamma_R q'\right) \right| B \right\rangle \left\langle h_2 \left| \sum_{q'} \left(q'^{\,\dagger} \gamma_L q\right) \right| 0 \right\rangle
\end{aligned}
$$

the effective Hamiltonian for the general decay $B \to h_1 h_2$ is now

$$\langle h_1 h_2 \left| \mathcal{H}_{\text{eff}} \right| B \rangle = \frac{G_F}{\sqrt{2}} \sum_n^6 a_n \left[O_n(h_1, h_2) + O_n(h_2, h_1) \right] \tag{1.36}$$

The factorised operators can now be expressed in terms of experimentally known quantities. Section 1.4 details this procedure for the decay $B^+ \to K^{*0}(892)\pi^+$.

1.3 Three-body Decay Kinematics

Three-body B decays have several kinematic constraints that can be used to distinguish different intermediate decays. First I shall consider the phase space available to a three-body decay and how the Dalitz plot can illustrate this. Intermediate resonances have additional dynamical behaviour, which I will examine next. Finally I will discuss the possible resonant contributions to the decay $B^+ \to K^+\pi^-\pi^+$.

1.3.1 The Dalitz Plot

Consider the decay of a B meson, with mass m_B, at rest to three particles with masses $m_{1,2,3}$, momenta $\vec{p}_{1,2,3}$ and energies $E_{1,2,3}$. Defining $p_{ij} = p_i + p_j$, where p_i is the four momentum of particle i, and $m_{ij}^2 = p_{ij}^2$ we find that

$$m_{12}^2 + m_{13}^2 + m_{23}^2 = m_B^2 + m_1^2 + m_2^2 + m_3^2 \tag{1.37}$$

and

$$m_{ij}^2 = (p_B - p_k)^2 = m_B^2 + m_k^2 - 2m_B E_k \tag{1.38}$$

The momenta of the three particles lie in a plane in the B rest frame and their orientation with respect to one another can be calculated from their energies.

The Lorentz invariant phase space for this decay is given by

$$dN \propto \delta^4 \left(p_B - \sum_{i=1}^{3} p_i \right) \prod_{i=1}^{3} \frac{d^3 p_i}{E_i} = \delta \left(m_B - \sum_{i=1}^{3} E_i \right) \frac{p_1^2 dp_1 p_2^2 dp_2 d\Omega_1 d\Omega_2}{E_1 E_2 E_3} \tag{1.39}$$

Since the B meson is scalar fixing the direction of $\vec{p}_1$ means that $\int d\Omega_1 = 4\pi$ and $\int d\Omega_2 = 2\pi d\cos\theta_{12}$, where θ_{12} is the angle between $\vec{p}_1$ and $\vec{p}_2$. Together with

$$E_3 = \sqrt{p_1^2 + p_2^2 + 2p_1 p_2 \cos\theta_{12} + m_3^2} \tag{1.40}$$

we find that

$$dN \propto \delta \left(m_B - E_1 - E_2 - \sqrt{p_1^2 + p_2^2 + 2p_1 p_2 \cos\theta_{12} + m_3^2} \right) d\cos\theta_{12} \frac{p_1^2 dp_1 p_2^2 dp_2}{E_1 E_2 E_3} \tag{1.41}$$

which becomes

$$dN \propto \frac{E_3}{p_1 p_2} \frac{p_1^2 dp_1 p_2^2 dp_2}{E_1 E_2 E_3} \tag{1.42}$$

$$\propto \frac{p_1 dp_1}{E_1} \frac{p_2 dp_2}{E_2} \tag{1.43}$$

Since $E_i dE_i = p_i dp_i$

$$dN \propto dE_1 dE_2 \tag{1.44}$$

$$\propto dm_{12}^2 dm_{23}^2 \tag{1.45}$$

The decay rate is therefore proportional to

$$|\mathcal{M}|^2 \, dm_{12}^2 dm_{23}^2 \tag{1.46}$$

where $\mathcal{M}$ is the matrix element for the particular decay.

A Dalitz plot [21] is defined as a scatter plot in any two of the three m_{ij}^2 variables. For example, the Dalitz plot for the decay $B^+ \to K^+\pi^-\pi^+$ is most usefully constructed

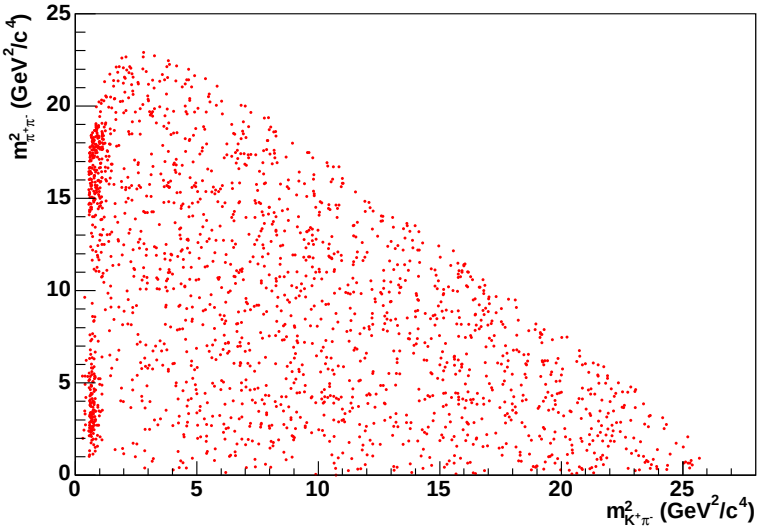

Figure 1.6: *Illustration of the Dalitz plot, showing* $B^+ \to K^+\pi^-\pi^+$ *non resonant and* $B^+ \to K^{*0}(892)\pi^+$*;* $K^{*0}(892) \to K^+\pi^-$ *toy Monte Carlo events.*

in the variables $m^2_{K^+\pi^-}$ and $m^2_{\pi^+\pi^-}$. The boundaries of the Dalitz plot at a given point along one axis occur when the momenta of the particles of the other axis are parallel or anti-parallel. For example if the Dalitz plot is constructed from $m^2_{K^+\pi^-}$ and $m^2_{\pi^+\pi^-}$ then the boundaries at a point in $m^2_{K^+\pi^-}$ occur where $\cos\theta_{\pi^+\pi^-} = \pm 1$

$$\left(m^2_{\pi^+\pi^-}\right)_{\max} = \left(E_{\pi^+} + E_{\pi^-}\right)^2 - \left(p_{\pi^+} - p_{\pi^-}\right)^2 \quad (1.47)$$

$$\left(m^2_{\pi^+\pi^-}\right)_{\min} = \left(E_{\pi^+} + E_{\pi^-}\right)^2 - \left(p_{\pi^+} + p_{\pi^-}\right)^2 \quad (1.48)$$

Decays which proceed only according to phase space will be found to be uniformly distributed in such a Dalitz plot. Appearance of non-uniform structure in a Dalitz plot is indicative of a matrix element that has dependence on kinematics. For example the decay $B^+ \to K^{*0}(892)\pi^+$ will appear as a narrow band around $m_{K^+\pi^-} = m_{K^{*0}}$ in the $B^+ \to K^+\pi^-\pi^+$ Dalitz plot, as can be seen in Figure 1.6. The following sections will discuss the kinematic dependence of resonant decays.

1.3.2 Mass

1.3.2.1 The Breit–Wigner Lineshape

Consider a spin-less particle with mass m_0 and decay rate Γ. The time dependent wave function for such a particle is given by

$$\Psi(t) = \Psi(0)e^{-t(im_0+\Gamma/2)} \tag{1.49}$$

Performing a Fourier transform yields the amplitude as a function of energy

$$A(E) = \int \Psi(t)e^{iEt}dt = \frac{C}{(m_0 - E) - i\Gamma/2} \tag{1.50}$$

where C is an arbitrary constant. Squaring the amplitude provides an estimator of the probability of measuring the state as having energy E. This is the Breit–Wigner formula:

$$|A(E)|^2 = \frac{C^2}{(m_0 - E)^2 + \Gamma^2/4} \tag{1.51}$$

There are several refinements that can be applied to this form. The first is to make it relativistic [22]

$$A(s) = \frac{C}{(m_0^2 - s) - im_0\Gamma} \tag{1.52}$$

where s is the reconstructed mass of the particle candidate. The second is to take into account that the width should really be a function of energy, particularly for wide resonances. Blatt and Weisskopf [23] put forward the following parameterisation of the width

$$\Gamma = \Gamma_0 \left(\frac{q}{q_0}\right)^{2j+1} \left(\frac{m_0}{\sqrt{s}}\right) \frac{F_j^2(q)}{F_j^2(q_0)} \tag{1.53}$$

where q is the momentum of either of the resonance daughters in the rest frame of the resonance; q_0 and Γ_0 are the values of q and Γ respectively when $\sqrt{s} = m_0$; j is the spin of the resonance and

$$F_0(x) = 1 \tag{1.54}$$

$$F_1(x) = \sqrt{1/(1 + R^2x^2)} \tag{1.55}$$

$$F_2(x) = \sqrt{1/(R^4x^4 + 3R^2x^2 + 9)} \tag{1.56}$$

where $R \approx 4.0(\text{ GeV}/c)^{-1}$ is the "radius" of the interaction.

1.3.2.2 The Flatté Lineshape

A further modification to the Breit–Wigner lineshape is to adapt it to account for the opening of a threshold. For example in the decay $B^+ \to f_0(980)K^+$ the opening of the $K\overline{K}$ threshold modifies the lineshape. This modification is given by the Flatté form [24]:

$$A(s) = \frac{C}{(m_0^2 - s) - im_0(\Gamma_{\pi\pi} + \Gamma_{KK})} \tag{1.57}$$

The decay widths of the resonance in the $\pi\pi$ and KK systems are given by

$$\Gamma_{\pi\pi} = g_\pi \sqrt{s - 4m_\pi^2} \tag{1.58}$$

$$\Gamma_{KK} = g_K \sqrt{s - 4m_K^2} \tag{1.59}$$

where $g_{\pi/K}$ are the coupling constants for $f_0(980) \to \pi^+\pi^-$ and K^+K^- respectively. Below the K^+K^- threshold the function continues analytically, the Γ_{KK} term contributing to the real part of the denominator. The coupling constants have been measured to be:

- $g_\pi = 0.138 \pm 0.010$ and $g_K/g_\pi = 4.45 \pm 0.25$ – BES Collaboration [25]
- $g_\pi = 0.09 \pm 0.01 \pm 0.01$ and $g_K = 0.02 \pm 0.04 \pm 0.03$ – E791 Collaboration [26]
- $g_\pi = 0.28 \pm 0.04$ and $g_K = 0.56 \pm 0.18$ – WA76 Collaboration [27].

1.3.3 Helicity Angle

Consider the decay of a particle denoted "1" into two particles denoted "2" and "3" in the rest frame of particle 1. The helicity of a particle is given by

$$\lambda_i = \frac{\vec{p}_i \cdot \vec{s}_i}{|\vec{p}_i|} \tag{1.60}$$

where $\vec{p}_i$ and $\vec{s}_i$ are the particle's momentum and spin. The two particles' momenta are back-to-back and since the orbital angular momentum $L = \vec{r} \times \vec{p}$ has no component along this direction the total angular momentum of the system is $\lambda_2 - \lambda_3$.

The decays considered in this analysis are of the form $1 \to 23$ where $2 \to 45$ (or $1 \to 345$ in the case of non resonant decay). Particle 1, the B meson, is a scalar particle, as are all the final state particles (3, 4 and 5). As such the angular momentum axis of resonance 2 is the only one that can give discriminating information. Since the spin of particles 1 and 3 are zero they are also helicity zero ($\lambda_{1,3} = 0$), so by conservation of angular momentum particle 2 must also be helicity zero. The angular distribution of the decay of particle 2 in to its two scalar daughters is given by a matrix element, which has the value $|P_{s_2}(\cos\theta_H)|^2$, where s_2 is the spin of particle 2 and P_{s_2} is a Legendre polynomial of order s_2 [28]. The angle θ_H is known as the helicity angle of the resonance. It is the angle between the momentum vector of one of the daughter particles (4 or 5), in the rest frame of the resonance, and the axis defined by the momentum of the resonance in the rest frame of the B. Vector resonances such as the $K^{*0}(892)$ and $\rho^0(770)$ will have daughters which are distributed according to $\cos^2\theta_H$, while the daughters of scalars, such as the $K_0^{*0}(1430)$ and $f_0(980)$ will be uniform in θ_H. Some resonances that may be present in the $B^+ \to K^+\pi^-\pi^+$ Dalitz plot are tensor (spin 2), *e.g.* $K_2^{*0}(1430)$ and $f_2(1270)$. These will have daughters distributed according to $|3\cos^2\theta_H - 1|^2$. The helicity angle of a resonance in the invariant mass m_{12} can be related to the other Dalitz plot variable by

$$\cos\theta_H = \frac{(m_{23}^2)_{\max} + (m_{23}^2)_{\min} - 2m_{23}^2}{(m_{23}^2)_{\max} - (m_{23}^2)_{\min}} \tag{1.61}$$

1.3.4 Interference

If a given intermediate state is a resonance its dynamics can be described using Eq. (1.52) and $\cos\theta_H$ by

$$\mathcal{M}_x \propto \frac{m_x\Gamma_x}{(m_x^2 - s) - im_x\Gamma_x} P_{s_x}(\cos\theta_H) \tag{1.62}$$

where m_x, Γ_x and s_x are the mass, width and spin of the resonance.

The $B^+ \to K^+\pi^-\pi^+$ Dalitz plot may contain many such modes, which are discussed in more detail in Section 1.3.5. Since these modes all decay to the same final state

they will quantum mechanically interfere with one another. The interference of two states with amplitudes $\mathcal{M}_a$ and $\mathcal{M}_b$ and a relative phase δ is of the following form

$$\begin{aligned} |\mathcal{M}|^2 &= \left|\mathcal{M}_a + \mathcal{M}_b e^{i\delta}\right|^2 && (1.63)\\ &= |\mathcal{M}_a|^2 + |\mathcal{M}_b|^2 + 2\mathrm{Re}\left(\mathcal{M}_a \mathcal{M}_b^* e^{i\delta}\right) && (1.64)\\ &= |\mathcal{M}_a|^2 + |\mathcal{M}_b|^2 + 2\mathrm{Re}\left(\mathcal{M}_a \mathcal{M}_b^*\right)\cos\delta - 2\mathrm{Im}\left(\mathcal{M}_a \mathcal{M}_b^*\right)\sin\delta && (1.65) \end{aligned}$$

Since the decay rate is given by Eq. (1.46) the effect of the interference terms is proportional to the area of overlap between resonances in the Dalitz plot. The orthogonality of the Legendre polynomials ensures that for resonances in the same mass pair with different spins the effect of interference on the branching ratio integrates to zero over $\cos\theta_H$ when the range of integration is symmetric about $\cos\theta_H = 0$. However, the distribution of events in the Dalitz plot will still reflect this interference and an amplitude analysis will be able to measure it.

1.3.5 The Light Meson Spectrum

The $B^+ \to K^+\pi^-\pi^+$ Dalitz plot may contain many possible resonances as well as a non resonant component. While some of these potential contributions are long established mesons with accurately measured properties others are not so well understood.

In the $K^+\pi^-$ spectrum there is the very well established $K^{*0}(892)$ but there are also many possible higher K^{*0} resonances, such as $K_0^{*0}(1430)$, $K_2^{*0}(1430)$ and $K^{*0}(1680)$. These resonances are reasonably well established and have masses and widths measured to within a few percent in some cases but only to $\sim 30\%$ in others. They predominantly decay to $K^+\pi^-$ and this branching fraction is known to a few percent in all cases. Table 1.1 summarises the information currently available [2].

The most poorly understood component of the $K^+\pi^-$ spectrum is the 0^+ component. This contains the $K_0^{*0}(1430)$, which is itself well established. However there are also suggestions of other contributions, either from a non resonant component that has

Table 1.1: *$K^+\pi^-$ Mass Spectrum Summary*

Resonance	Mass (MeV/c^2)	Width (MeV/c^2)	Branching Fraction to $(K\pi)^0$
$K^{*0}(892)$	896.10 ± 0.27	50.7 ± 0.6	$(99.770 \pm 0.020)\%$
$K_0^{*0}(1430)$	1412 ± 6	294 ± 23	$(93 \pm 10)\%$
$K_2^{*0}(1430)$	1432.4 ± 1.3	109 ± 5	$(49.9 \pm 1.2)\%$
$K^{*0}(1680)$	1717 ± 27	322 ± 110	$(38.7 \pm 2.5)\%$

an "effective range" form [29,30] or from a very broad resonance dubbed the κ [31]. The LASS experiment made measurements of $K\pi$ scattering and as part of this study produced a description of the S-wave that consists of the $K_0^{*0}(1430)$ resonance together with an effective range non resonant component. This description, modified to account for differences between $K\pi$ scattering and B decay production is shown in Eq. (1.66):

$$\mathcal{M} = \frac{m_{K\pi}}{q\cot\delta_B - iq} + e^{2i\delta_B}\frac{m_0\Gamma_0\frac{m_0}{q_0}}{(m_0^2 - m_{K\pi}^2) - im_0\Gamma_0\frac{q}{m_{K\pi}}\frac{m_0}{q_0}} \tag{1.66}$$

where m_0 and Γ_0 are the mass and width of the $K_0^{*0}(1430)$ resonance, q_0 is defined as in Eq. (1.53) and $\cot\delta_B$ is defined by

$$\cot\delta_B = \frac{1}{aq} + \tfrac{1}{2}rq \tag{1.67}$$

where r is the effective range, and a is the scattering length. These parameters have been measured to be $1.76 \pm 0.36\,(\mathrm{GeV}/c)^{-1}$ and $1.95 \pm 0.09\,(\mathrm{GeV}/c)^{-1}$ respectively from fits to LASS data [30]. However, there is no *a priori* reason to expect these parameters to have the same values in the case of production in B decay.

In the $\pi^+\pi^-$ spectrum the $\rho^0(770)$ is very well established and measured. The $f_0(980)$ is well established but measurements of its mass and width continue to show disagreement and its composition is unclear, with many possible explanations including that it is a multi-quark state or a $K\overline{K}$ bound state. Several higher f and ρ states may also contribute, including the $f_2(1270)$, $f_0(1370)$, $\rho^0(1450)$, $f_0(1500)$and $f_2'(1525)$. Table 1.2 gives a summary of the currently available information.

Table 1.2: *$\pi^+\pi^-$ Mass Spectrum Summary*

Resonance	Mass (MeV/c^2)	Width (MeV/c^2)	Branching Fraction to $\pi^+\pi^-$
$\rho^0(770)$	775.8 ± 0.5	146.4 ± 1.5	$\sim 100\%$
$f_0(980)$	980 ± 10	$40 - 100$	dominant
$f_2(1270)$	1275.4 ± 1.2	185.1 ± 3.5	$(84.8 \pm 2.5)\%$
$f_0(1370)$	$1200 - 1500$	$200 - 500$	seen
$\rho^0(1450)$	1465 ± 25	400 ± 60	seen
$f_0(1500)$	1507 ± 5	109 ± 7	$(34.9 \pm 2.3)\%$
$f_2'(1525)$	1525 ± 5	76 ± 10	$(8.2 \pm 1.5) \times 10^{-3}$

There is also a potential contribution from a very broad state dubbed the σ but again it is very unclear if this really exists. For a full review of the light scalar mesons see [2].

1.4 The Decay $B^+ \to K^{*0}(892)\pi^+$

In this section the implications of the theories presented in the previous sections will be discussed, taking as an example the decay $B^+ \to K^{*0}(892)\pi^+$. Predictions for $B^+ \to \rho^0(770)K^+$ will also be presented.

1.4.1 Branching Fraction Predictions

Using the formalisms of the operator product expansion and factorisation, theorists can attempt to make predictions of the branching fraction of $B^+ \to K^{*0}(892)\pi^+$. This decay has no contributions from tree diagrams or from the the scalar operator O_6 (Section 1.2.3.2). So it proceeds only via the left handed penguin diagram

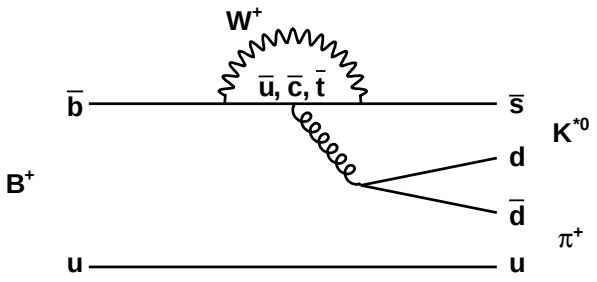

Figure 1.7: *The diagram for the decay* $B^+ \to K^{*0}(892)\pi^+$.

Figure 1.7 and the Eq. (1.36) becomes

$$\left\langle K^{*0}\pi^+ \left|\mathcal{H}_{\text{eff}}\right| B^+ \right\rangle = \frac{G_F}{\sqrt{2}} V_{tb}V_{ts}^* a_4 \left[O_4(K^{*0},\pi^+) + O_4(\pi^+,K^{*0})\right] \tag{1.68}$$

The matrix elements in O_4 can be expressed in terms of experimentally known quantities such as

$$\left\langle \pi^+ \left| u^\dagger \gamma^\mu \gamma_L d \right| 0 \right\rangle = -f_\pi p_\pi^\mu \tag{1.69}$$

$$\left\langle K^{*0} \left| d^\dagger \gamma^\mu \gamma_L s \right| 0 \right\rangle = \frac{1}{\sqrt{2}} f_{K^{*0}} m_{K^{*0}} \epsilon_{K^{*0}}^\mu \tag{1.70}$$

where p_π^μ is the four-momentum of the pion, $\epsilon_{K^{*0}}^\mu$ is the polarisation vector of the K^{*0} meson and the form factors f_π and $f_{K^{*0}}$ are determined from leptonic decays of the pion and from tau lepton decays, respectively, to be $f_\pi = (0.1307 \pm 0.0005)\,\text{GeV}$, $f_{K^{*0}} = (0.22 \pm 0.01)\,\text{GeV}$ [32]. The B meson elements can also be expressed in terms of such form factors. The expressions are simplified because the final state is helicity zero (Section 1.3.3) and are found to be [19]

$$\left\langle \pi^+ \left| u^\dagger \gamma^\mu \gamma_L d \right| 0 \right\rangle \left\langle K^{*0} \left| b^\dagger \gamma^\mu \gamma_L s \right| B^+ \right\rangle = \sqrt{2} m_{K^{*0}} \epsilon_{K^{*0}} \cdot p_\pi f_{K^{*0}} F_1^\pi(m_{K^{*0}}^2) \tag{1.71}$$

$$\left\langle K^{*0} \left| d^\dagger \gamma^\mu \gamma_L s \right| 0 \right\rangle \left\langle \pi^+ \left| u^\dagger \gamma^\mu \gamma_L b \right| B^+ \right\rangle = 2 m_{K^{*0}} \epsilon_{K^{*0}} \cdot p_\pi f_\pi A_0^{K^{*0}}(m_\pi^2) \tag{1.72}$$

The form factors $A_0(0)$ and $F_1(0)$ are obtained from lattice-QCD calculations and are found to be $F_1^\pi(0) = 0.30 \pm 0.04$ and $A_0^{K^{*0}}(0) = 0.39 \pm 0.10$ [19].

Evaluation of the coefficient a_4 gives varying results depending on whether and how certain non-factorisable contributions are included. As such a given publication may contain several different predictions from different models. The predictions from several recent theoretical publications for the branching fractions of both $B^+ \to K^{*0}(892)\pi^+$ and $B^+ \to \rho^0(770)K^+$ are given in Table 1.3. These all use factorisation except for [33], which uses isospin and SU(3) symmetry and is included for comparison.

1.4.2 *CP* Asymmetry Predictions

The direct *CP* asymmetry is defined as in equation Eq. (1.12). As mentioned in the previous section, the decay $B^+ \to K^{*0}(892)\pi^+$ has no tree contributions so the amplitudes can be written as

$$A = P_t V_{tb} V_{ts}^* e^{i\delta_t} + P_c V_{cb} V_{cs}^* e^{i\delta_c} + P_u V_{ub} V_{us}^* e^{i\delta_u} \quad (1.73)$$

$$\bar{A} = P_t V_{tb}^* V_{ts} e^{i\delta_t} + P_c V_{cb}^* V_{cs} e^{i\delta_c} + P_u V_{ub}^* V_{us} e^{i\delta_u} \quad (1.74)$$

where P_i is the amplitude for the penguin diagram with the quark in the loop being of flavour i. These expressions simplify by using the Unitarity relation $V_{ub}V_{us}^* + V_{cb}V_{cs}^* + V_{tb}V_{ts}^* = 1$ and the following definitions

$$P_{tc} e^{i\delta_{tc}} = P_t e^{i\delta_t} + P_c e^{i\delta_c} \quad (1.75)$$

$$P_{uc} e^{i\delta_{uc}} = P_u e^{i\delta_u} + P_c e^{i\delta_c} \quad (1.76)$$

to

$$A = P_{tc} V_{tb} V_{ts}^* e^{i\delta_{tc}} + P_{uc} V_{ub} V_{us}^* e^{i\delta_{uc}} \quad (1.77)$$

$$\bar{A} = P_{tc} V_{tb}^* V_{ts} e^{i\delta_{tc}} + P_{uc} V_{ub}^* V_{us} e^{i\delta_{uc}} \quad (1.78)$$

Furthermore, $\arg(V_{ub}V_{us}^*) = \gamma$ and $\arg(V_{tb}V_{ts}^*) = 0$ from Eq. (1.4), so

$$A_{CP} = \frac{2P_{tc}P_{uc}\left|V_{ub}^* V_{us} V_{tb} V_{ts}^*\right| \sin\gamma \sin\left(\delta_{uc} - \delta_{tc}\right)}{P_{uc}^2 \left|V_{ub}V_{us}^*\right|^2 + P_{tc}^2 \left|V_{tb}V_{ts}^*\right|^2 - 2P_{tc}P_{uc}\left|V_{ub}^* V_{us} V_{tb} V_{ts}^*\right| \cos\gamma \cos\left(\delta_{uc} - \delta_{tc}\right)} \quad (1.79)$$

Table 1.3: *Theoretical predictions of the charmless branching fractions* $B^+ \to K^{*0}(892)\pi^+$ *and* $B^+ \to \rho^0(770)K^+$.

$\mathcal{B}(B^+ \to K^{*0}(892)\pi^+) \times 10^6$	$\mathcal{B}(B^+ \to \rho^0(770)K^+) \times 10^6$	Reference
7.889	1.882	[34]
11.080	5.655	
4.4	2.0	[35]
9.1	4.6	
2.583	0.453	
3.497	0.426	
3.814	0.528	[36]
2.531	0.609	
3.433	0.503	
3.731	0.631	
3.6	2.6	
3.4	1.3	
2.2	6.0	[20]
7.3	4.7	
8.4	4.3	
9.7	4.8	
9.5	4.4	[33]
9.4	4.5	

Since $V_{ub}^* V_{us}$ is small ($|V_{ub}| = (3.67 \pm 0.47) \times 10^{-3}$ and $|V_{us}| = 0.2196 \pm 0.0023$ [2]) this reduces to

$$A_{CP} \approx 2\frac{P_{uc}}{P_{tc}} \left| \frac{V_{ub}V_{us}^*}{V_{tb}V_{ts}^*} \right| \sin\gamma \sin\left(\delta_{uc} - \delta_{tc}\right) \tag{1.80}$$

So the Standard Model asymmetry is less than 6% and will be less than this if $\frac{P_{uc}}{P_{tc}}$ provides further suppression. More precise predictions using factorisation or isospin/SU(3) from several recent theoretical publications for both $B^+ \to K^{*0}(892)\pi^+$

and $B^+ \to \rho^0(770)K^+$ are given in Table 1.4. If a large asymmetry were to be measured in $B^+ \to K^{*0}(892)\pi^+$ it would indicate that new physics processes are entering the penguin diagram loop.

Table 1.4: *Theoretical predictions of CP asymmetries in the charmless decays $B^+ \to K^{*0}(892)\pi^+$ and $B^+ \to \rho^0(770)K^+$.*

$A_{CP}(B^+ \to K^{*0}(892)\pi^+)$	$A_{CP}(B^+ \to \rho^0(770)K^+)$	Reference
–	0.00	[35]
–	0.01	
0.0097	0.0288	
0.0123	−0.8025	[36]
0.0117	0.0287	
0.0149	−0.7931	
0.016	−0.136	
0.017	−0.273	
0.016	−0.093	[20]
0.008	0.266	
0.008	0.317	
0.0	0.24	
0.0	0.21	[33]
0.0	0.19	

2

The *BABAR* Experiment

2.1 Introduction

The *BABAR* experiment was constructed primarily to study time-dependent *CP*-violating asymmetries in the decays of neutral B mesons to CP eigenstates. Secondary goals include precision measurements of the rates of rare decays of the neutral and charged B mesons as well as a range of charm and τ physics. These physics considerations drove the design of the *BABAR* detector and the PEP-II accelerator. This chapter will describe PEP-II and *BABAR*, focusing on how the physics requirements are met by the design and performance of the accelerator and detector.

2.2 The PEP-II Accelerator

2.2.1 Overview

A complete description of the PEP-II machine can be found in [37]. The operational centre of mass (CM) energy of the PEP-II accelerator was chosen to be 10.58 GeV, corresponding to the $\Upsilon(4S)$ resonance, which decays almost exclusively to $B\overline{B}$ pairs. At this energy the cross section for $\Upsilon(4S)$ ($b\overline{b}$) production is approximately 1.1 nb, while that of continuum $q\overline{q}$ production (u,d,s,c) is around 3.4 nb, and that of τ production is 0.9 nb. In addition to the relatively high $B\overline{B}$ cross section, the $\Upsilon(4S)$ energy is just above $B\overline{B}$ production threshold and consequently the B mesons are produced almost at rest in the CM frame. As such, the four momenta of the B mesons are well known and can be used to construct kinematic variables that are used to discriminate against backgrounds (Section 3.5.1). Furthermore the accelerator can run at an energy where there is no $B\overline{B}$ production by reducing the CM energy by only ~ 40 MeV. Approximately 10% of data is taken in this *off-peak* mode and is used to study backgrounds from continuum events.

The $B\overline{B}$ pair produced from the decay of the $\Upsilon(4S)$ is produced in a coherent state, which permits the use of flavour tagging, as described in Section 1.2.2.4. Flavour tagging is essential for time-dependent measurements. Time-dependent measurements also require that the decay vertices of the two B mesons are separated by a measurable distance. This is achieved in the accelerator design by having asymmetric beam energies (9.0 GeV for the e^- beam and 3.1 GeV for the e^+ beam), which leads to the $\Upsilon(4S)$ system having a relativistic boost of $\beta\gamma = 0.56$ in the direction of the e^- beam in the laboratory (detector) frame.

The branching fractions of many of the interesting *CP* eigenstate modes are small, ranging from 10^{-4} to 10^{-6}. Precision measurements of *CP* quantities, as well as branching fraction measurements of potentially very rare processes, require a data sample of several hundred million $B\overline{B}$ pairs. In order for *BABAR* to record such a

large data sample the PEP-II accelerator must achieve extremely high luminosities and have minimal down time. The *BABAR* detector must also operate with very high efficiency.

2.2.2 The Interaction Region

In order to achieve the high luminosities that the physics program requires the beams are divided into a large number of ($\sim$ 1500) low charge bunches, which minimises beam-beam interference. The spacing of these bunches means that secondary collisions would occur 62 cm from the interaction point (IP). To avoid these secondary collisions the beams are horizontally displaced from one another until just before the IP, when they are brought together using separation dipole magnets placed very close to the IP. At the IP the beams collide head-on then are separated once again by the dipoles. At the point of collision the beams make an angle of 20 mrad to the z-axis in the x–z plane. Figure 2.1 shows a plan view of the interaction region, on which the separation dipole magnets are marked B1. The B1 magnets reside within the *BABAR* detector volume and as such have an effect on both the detector acceptance and the background conditions.

Focusing of the beams is achieved using sets of quadrupole magnets. Q4 and Q5 (in Figure 2.1) focus the high energy ring (HER) while Q2 focuses the low energy ring (LER). Q1 is a final focus and affects both beams. Q2, Q4 and Q5 are iron magnets and are located entirely outside the detector volume, while the Q1 magnets are permanent magnets and partially enter the detector volume.

2.2.3 Machine Backgrounds

Machine backgrounds lead to high occupancy in the detector systems and as such can degrade physics measurements. They can also lead to radiation damage in the detector systems, both through short acute doses and long term exposure.

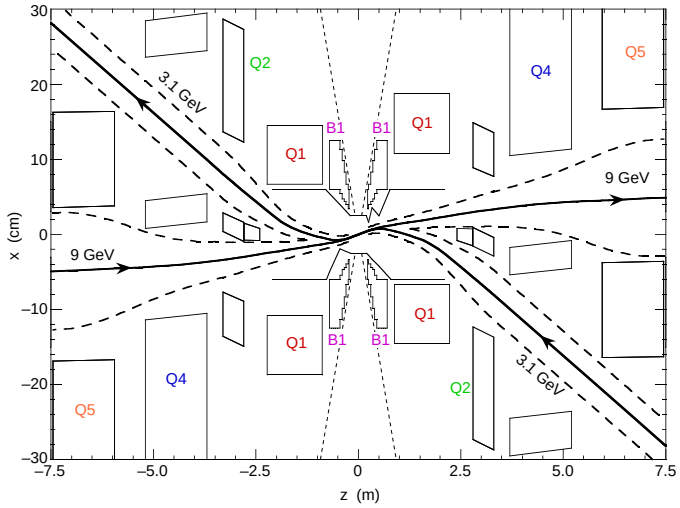

Figure 2.1: *Plan view of the PEP-II interaction region with an exaggerated vertical scale.*

Synchrotron radiation is particularly problematic in PEP-II because of the complicated optics near the IP. The geometry of the interaction region was designed such that the majority of the synchrotron radiation from the extra bending magnets passes through the detector without interaction. Copper masks have also been employed to prevent interaction with the beam pipe.

Beam particles that undergo bremsstrahlung or coulombic interactions with gas molecules in the beam pipe may have momenta that fall outside the maximum range of the storage rings. Such *lost* particles may strike the beam pipe, producing an electromagnetic shower. This background is minimised by keeping a very good vacuum in the beam pipe near the IP.

A final source of background is from radiative Bhabha scattering events where an electron or positron hits material a short distance from the IP causing electromagnetic showers that enter the detector. This background has not caused much problem so far but since it, like the others, scales with luminosity it will become more significant as the experiment goes on.

2.2.4 Trickle Injection

A recent development in the operation of the PEP-II machine is that of trickle injection. The original mode of operation for the accelerator was to fill both beams and then to continue collisions until the instantaneous luminosity reached a certain lower limit. At this point there would be a pause in data taking whilst the beams were topped up by injecting from the SLAC linac. Once the top up was completed and stable beams achieved data taking would continue. This method worked well and protected the detector from backgrounds that occur during injection, since during this period the high voltage of the various systems was ramped down, but it is not optimal as far as delivering integrated luminosity.

The alternative is to continuously inject the rings at a very low rate, $\sim 2 - 3\,\mathrm{Hz}$. This will lead to a much greater efficiency of luminosity delivery but has the potential downside of increased machine backgrounds and also has associated technical difficulties for both the accelerator and the detector teams.

In November 2003 tests were carried out where the LER was continuously trickle injected. The backgrounds were measured and data was recorded, processed and compared with data from normal operation. The increase in backgrounds was found to be manageable and the data compared well with the control samples. From early December the default data taking mode was with LER trickle injection. In March 2004 tests were carried out where the HER was trickle injected instead of the LER. The success of these tests lead on to further tests where both rings were trickle charged, and from mid March the default mode was for both rings to be trickle injected. Figure 2.2 indicates the increase in integrated luminosity since PEP-II has started running in trickle injected mode. For full details of the trickle injection method and performance gain see [38, 39].

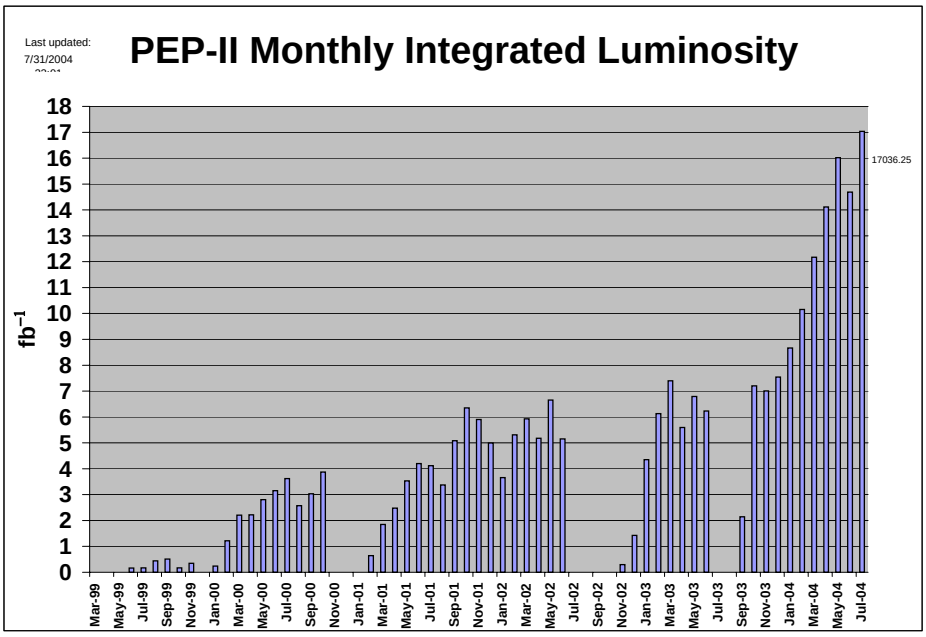

Figure 2.2: *PEP-II integrated luminosity per month.*

2.2.5 Performance

The PEP-II accelerator performance has been excellent to date. Design luminosity, both instantaneous and integrated, was achieved within the first year of operation. The recent progress on trickle injection has seen a dramatic increase in performance and further measures are planned for the future to continue the upward trend. Table 2.1 shows some of the performance records of the PEP-II machine achieved in the period since first collisions in May 1999 up to the end of July 2004. The data used in this analysis were recorded during this period.

Table 2.1: *PEP-II Machine Performance Records*

Parameter	Design	Best achieved
HER Current (A)	0.75	1.55
LER Current (A)	2.14	2.44
Luminosity (10^{33} $\mathrm{cm^{-2}s^{-1}}$)	3	9.213
Luminosity ($\mathrm{pb^{-1}}$/8 hour shift)	—	246.3
Luminosity ($\mathrm{pb^{-1}}$/day)	130	710.5
Luminosity ($\mathrm{fb^{-1}}$/week)	—	4.464
Luminosity ($\mathrm{fb^{-1}}$/month)	—	17.036
Total Delivered Luminosity (on- and off-peak)		$256\,\mathrm{fb^{-1}}$

2.3 The *BABAR* Detector

A complete description of the *BABAR* detector can be found in [40]. As stated in Section 2.1 the main physics goals of the experiment drove the design of the accelerator and the detector. Section 2.2 has shown how the accelerator design has accommodated the physics requirements placed on it. Here I shall outline the requirements on the detector and give an overview of the detector, before the following sections go on to describe the detector systems individually.

BABAR was designed as a general purpose detector optimised for its primary physics goals, which place the following requirements on the detector design:

- ◇ The detector must have uniform, and the greatest possible, angular acceptance in the CM frame.
- ◇ High reconstruction efficiency for both charged and neutral particles.
- ◇ Good position and momentum resolution for charged particles over the momentum range $60\,\mathrm{MeV}/c - 4\,\mathrm{GeV}/c$.

- ◇ Good energy and angular resolution for neutral particles over the energy range $20\,\text{MeV} - 4\,\text{GeV}$. This is essential for detection of π^0 and η particles.
- ◇ Excellent vertex resolution in z direction for measurements of the decay time difference of the two B mesons, and in transverse direction for reconstruction of secondary charm and τ vertices.
- ◇ Excellent particle identification for e, μ, π, K and p over a wide range of momenta. This is essential for flavour tagging and separating important final states such as $K^+\pi^-$ and $\pi^+\pi^-$.
- ◇ The detector must be able to operate under the high background conditions commensurate with the high luminosities.

The *BABAR* detector was designed to satisfy the above requirements imposed by the physics, whilst also satisfying the criteria imposed by the real world, particularly those of cost minimisation and maximisation of reliability. The final design, illustrated in Figure 2.3, consists of a system of five sub-detectors, each of which will be discussed in more detail in the following sections. The sub-detectors are, starting with the innermost, the silicon vertex tracker (SVT), the drift chamber (DCH), the detector of internally reflected Cerenkov radiation (DIRC), the electromagnetic calorimeter (EMC) and the instrumented flux return (IFR). The first four of these systems are enclosed in the 1.5 T magnetic field of the superconducting magnetic coil also marked in Figure 2.3. In order to maximise the angular acceptance in the CM frame the whole detector is offset from the IP by 0.37 m in the direction of the HER, and is asymmetric in design.

2.3.1 The *BABAR* Co-ordinate System

BABAR uses a right-handed co-ordinate system with the origin at the IP. The z-axis corresponds to the principal axis of the drift chamber in the direction of the HER.

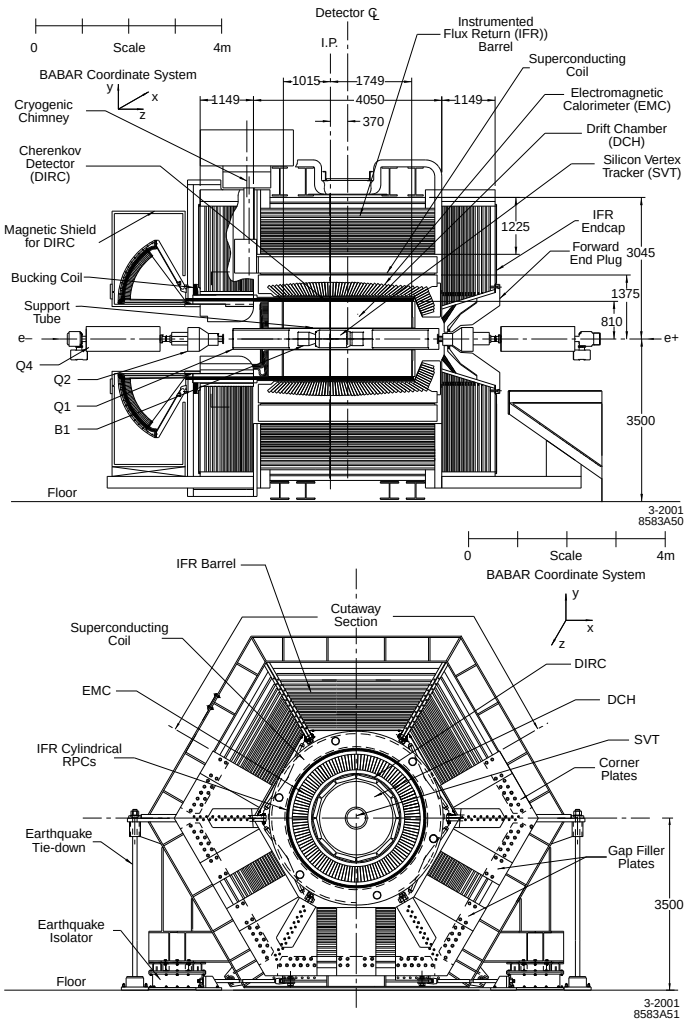

Figure 2.3: *The BABAR Detector.*

The y-axis points vertically upwards while the x-axis points horizontally out from the centre of the of PEP-II ring. The polar (θ) and azimuthal (ϕ) angles are defined as in the standard spherical polar co-ordinate system.

2.4 The Silicon Vertex Tracker (SVT)

2.4.1 SVT Physics Requirements

The primary physics goal of the SVT is to make precise measurements of the z position of tracks in order to provide good measurement of the separation of the two B decay vertices. These are essential for time-dependent CP violation studies, which are the primary physics goal of the *BABAR* experiment. Monte Carlo studies [41] have shown that the resolution required for such measurements is $80\,\mu$m. Other physics goals of the experiment require precision measurements of secondary decay vertices, such as those of D mesons or τ leptons. This places the requirement of a resolution of $100\,\mu$m in the x–y plane on the SVT.

The SVT must also have excellent tracking efficiency for tracks with transverse momenta (p_T) less than $120\,\mathrm{MeV}/c$, since these will not be reliably detected by the DCH, the primary tracking system. These include slow pions from decays of D^* particles, which are very common B-decay products. The achievement of maximum resolution on measurements of the Cerenkov angle in the DIRC are also reliant upon the measurements of track angle made by the SVT for high p_T tracks. Finally the SVT is also used for particle identification, measuring the energy loss ($\mathrm{d}E/\mathrm{d}x$) of particles with momenta less than $700\,\mathrm{MeV}/c$.

2.4.2 SVT Design

In addition to the physics requirements just described there are other factors that effect the design of the SVT. The design of the PEP-II interaction region (discussed in Section 2.2) places constraints on the acceptance of the SVT. Even so, the acceptance in the polar angle (θ) is 20.1° to 150.2° and encompasses 90% of the solid angle in the CM frame. The SVT design must also take into account the high levels of radiation it will be bombarded with during its lifetime. The budget used in the

design was 2 MRad and an instantaneous limit of up to 1 Rad/ms. The design must also limit the amount of material through which the tracks pass in order to reduce multiple scattering and bremsstrahlung.

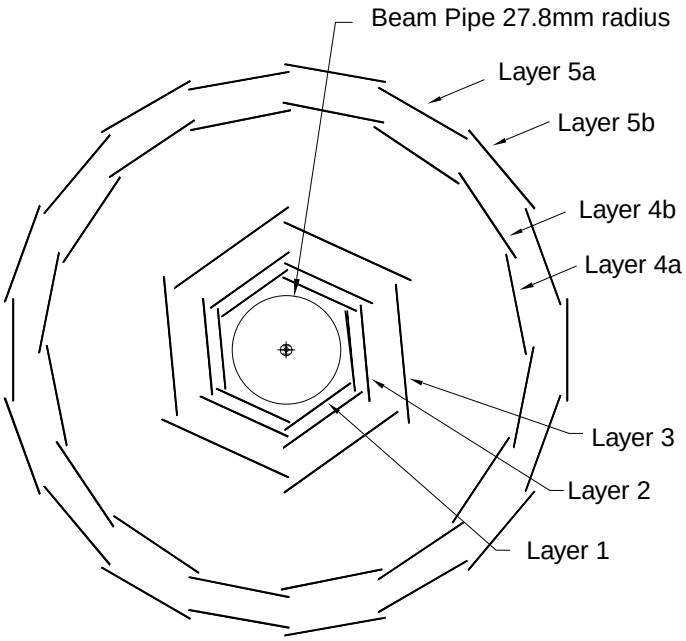

Figure 2.4: *End on view of the SVT showing the five layer structure.*

The design consists of five layers of double sided silicon strip sensors, divided azimuthally into modules, as shown in Figure 2.4. Layers $1-3$ have 6 modules each, which are tilted by 5° in ϕ so that they overlap slightly, both to provide complete coverage and to aid with alignment. Layers 4 and 5 have 16 and 18 modules respectively and as can be seen in Figure 2.5 they are arch shaped in the longitudinal plane to increase angular coverage whilst minimising the amount of material tracks pass through as well as their angles of incidence. This arch design means that these layers cannot be tilted like the inner layers and so overlapping is achieved by splitting the modules between two sub-layers at slightly different radii. The strips on either side of the sensors are arranged orthogonally, with the inner side giving z measurements and the outer side giving ϕ measurements. Layers 1 and 2 have primary responsibility for measuring the track angle, while layers 4 and 5 are mainly

used for alignment with the DCH. Layer 3 provides extra tracking information used for the low p_T tracks that don't make it to the DCH.

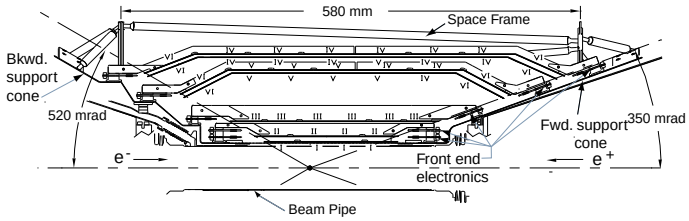

Figure 2.5: *Side on view of the SVT showing the five layer structure, and the arch design of the outer two layers.*

Each module is divided into forward and backward halves each of which are read out by electronics placed outside the detector acceptance. The readout uses a time over threshold (TOT) technique to determine the total charge deposited in a strip. The strip signals are amplified and shaped before being compared with a threshold that depends on background conditions. The TOT has a logarithmic dependence on the deposited charge and so a large range can be covered. Each TOT measurement supplies not only position information but a $\mathrm{d}E/\mathrm{d}x$ measurement, allowing up to ten such measurements in the SVT. The overall SVT measurement of $\mathrm{d}E/\mathrm{d}x$ is taken as the mean of the lowest 60% of the individual measurements from sensors. This truncated mean is used because $\mathrm{d}E/\mathrm{d}x$ is distributed according to a Landau distribution.

Precise knowledge of the alignment of the SVT, both the internal alignment of the modules (local alignment) and the alignment of the whole system with respect to the rest of the detector (global alignment), is essential for achieving the best position and momentum resolution. Local alignment is more complicated and is only necessary after detector access times. It is performed using very high momentum two-prong events, mainly $e^+e^- \to \mu^+\mu^-$, and cosmic ray events. Global alignment is performed on a run-by-run basis by fitting tracks with sufficient numbers of SVT and DCH hits. The fits are performed twice, once using only the DCH information and again

only with the SVT information. The alignment parameters are then obtained by minimising the differences between the track parameters obtained from the two fits. During the period of *BABAR* Runs 1–3 the constants obtained from one run were used to reconstruct data from the next, a procedure known as *rolling calibration*. Since the start of Run 4 a new two-stage procedure has been employed that uses a small sub-sample of events in a run to determine the calibration constants, which are then used to reconstruct the rest of the events in the run.

2.4.3 SVT Performance

The spatial resolution of SVT hits is calculated by comparing the hit position with the trajectory of the track in the plane of the sensor for high momentum two-prong events. For this comparison the track is refitted omitting the layer being studied. The uncertainty on the track trajectory is subtracted from the width of the residual distribution to give the hit resolution. It is found to be better than 40 μm in each of the first three layers (at all angles), which means that the B decay vertex resolution is better than 70 μm. The SVT tracking efficiency as measured in data is 97%, excluding defective readout sections, which account for fewer than 5% of the total (a section is one side of a half module, there being 208 in total). The $\mathrm{d}E/\mathrm{d}x$ resolution for minimum ionising particles (MIPs) is found to be 14%, which makes possible a 2σ separation of pions and kaons up to a momentum of 500 MeV/c and of kaons and protons up to 1 GeV/c.

The lifetime radiation limit of the SVT was expected to be 2 MRad, however recent studies have shown that this should be closer to 5 MRad. The limit is still some distance away but the ever increasing luminosities are raising the radiation dose that the SVT receives, the modules in the horizontal plane receiving the most. As such replacement modules for the SVT are under construction and will be fitted during the next long shutdown, which is currently scheduled to be summer 2005 or 2006.

2.5 The Drift Chamber (DCH)

2.5.1 DCH Physics Requirements

The DCH is the principal charged particle detector in *BABAR*. It is required to make precision measurements of particle momenta and track angles for particles with momenta greater than 120 MeV/c and in the range $0.1 < p_T < 5.0$ GeV/c. It must therefore cover as large a solid angle as possible whilst keeping at a minimum the amount of material that particles must pass through. The DCH also plays an important role in extrapolating charged tracks into the DIRC, EMC and IFR.

In order for exclusive reconstruction of B and D decays to be performed the momentum resolution must be $\sigma_{p_T}/p_T < 0.3\%$ and the spatial hit resolution must be better than 140 μm. The DCH is also the main source of reconstruction information for K^0_S particles, which feature in many of the so called "golden modes" for time dependent *CP* asymmetry studies, such as $B^0 \to J/\psi\, K^0_S$. This places the further requirement of measuring longitudinal position with a resolution better than 1 mm. In addition the DCH has an essential role in performing particle identification for particles with momenta less than 700 MeV/c when the DIRC becomes ineffective, as well as for areas that fall outside the DIRC acceptance. This requires $\mathrm{d}E/\mathrm{d}x$ measurements with a minimum resolution of around 7%. Finally, the DCH must also pass tracking and timing information to the Level 1 Trigger every 269 ns.

2.5.2 DCH Design

Figure 2.6 shows a longitudinal section of the DCH, which is a 2.8 m long cylinder placed asymmetrically about the IP in order to increase coverage in the forward direction. The chamber has an inner radius of 23.6 cm, an outer radius of 80.9 cm and is filled with a low mass gas mixture consisting of helium and isobutane in a ratio of 4:1. This mixture provides good spatial and $\mathrm{d}E/\mathrm{d}x$ resolution and a short drift

time whilst also minimising multiple scattering. A small amount of water vapour (0.3%) is added to the mixture to prolong the life of the chamber.

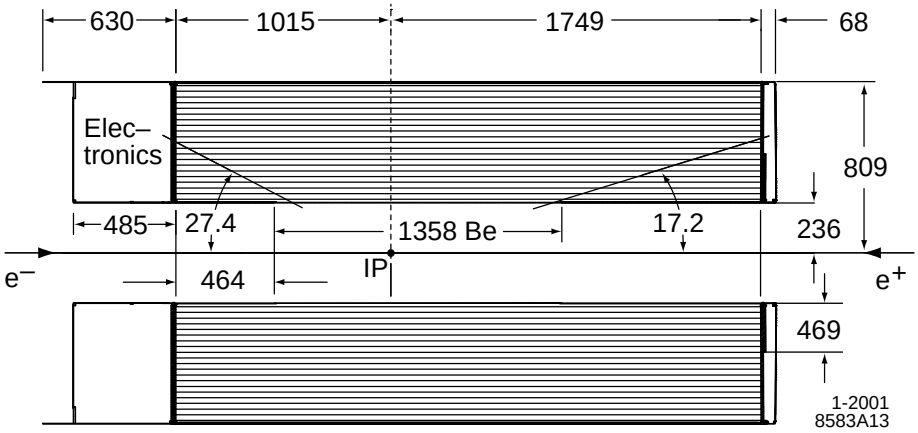

Figure 2.6: *Side on view of the DCH.*

The detection mechanism is built up from 7104 hexagonal drift cells, which are typically $1.2 \times 1.8\,\mathrm{cm}^2$ in size. Each of these cells consists of a single $20\,\mu$m diameter gold plated tungsten-rhenium sense wire surrounded by six $120\,\mu$m or $80\,\mu$m gold plated aluminium field wires. The sense wires are held at a high voltage (design voltage 1960 V) whilst the field wires are grounded, creating a field with almost circular symmetry over most of the cell.These cells form circular layers around the axis of the drift chamber, with a group of four layers forming a "superlayer". There are ten superlayers in the complete DCH. Each sequential layer is staggered by half a cell as shown in Figure 2.7, which permits left-right ambiguities to be resolved within a superlayer even if one out of four signals is missing, as well as allowing local segment finding. Six out of the ten superlayers are orientated at a small angle to the z-axis in order to permit longitudinal position calculation. The superlayers alternate between axial (A) and positive and negative stereo (U,V) from the innermost superlayer outwards according to the following pattern: AUVAUVAUVA. The angle of each stereo layer increases from 45 mrad for the innermost stereo layer to 76 mrad for the outermost. The complete gas and wire system is 0.28% of a radiation length for tracks with normal incidence.

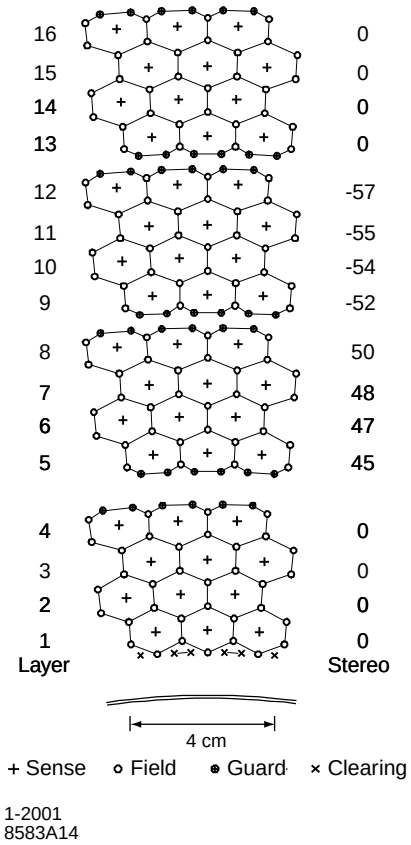

Figure 2.7: *DCH cell layout for the first four superlayers. The stereo angle of the layers in* mrad *is shown in the right hand column.*

Charged particles passing through a drift cell ionise the gas mixture producing electrons, which are accelerated in the field of the cell towards the sense wire. The electrons further ionise the gas causing a charge avalanche (a gain of 5×10^4 for the design voltage of 1960 V) that descends on the sense wire. The leading edge of this signal is detected and digitised with 1 ns resolution to determine the drift time and hence the positional information. The total charge deposited is also used to determine $\mathrm{d}E/\mathrm{d}x$ for the track, using a truncated mean of the lowest 80% of the individual energy loss measurements.

2.5.3 DCH Performance

The drift time to track distance relation is calibrated using high momentum two-prong events. The calibration is performed for each cell, the drift distance being estimated by calculating the distance of closest approach of the best fit to the track in question, where the fit is performed omitting the cell being calibrated. $\mathrm{d}E/\mathrm{d}x$ measurements are also calibrated to remove biases from several sources including changes in gas pressure and temperature.

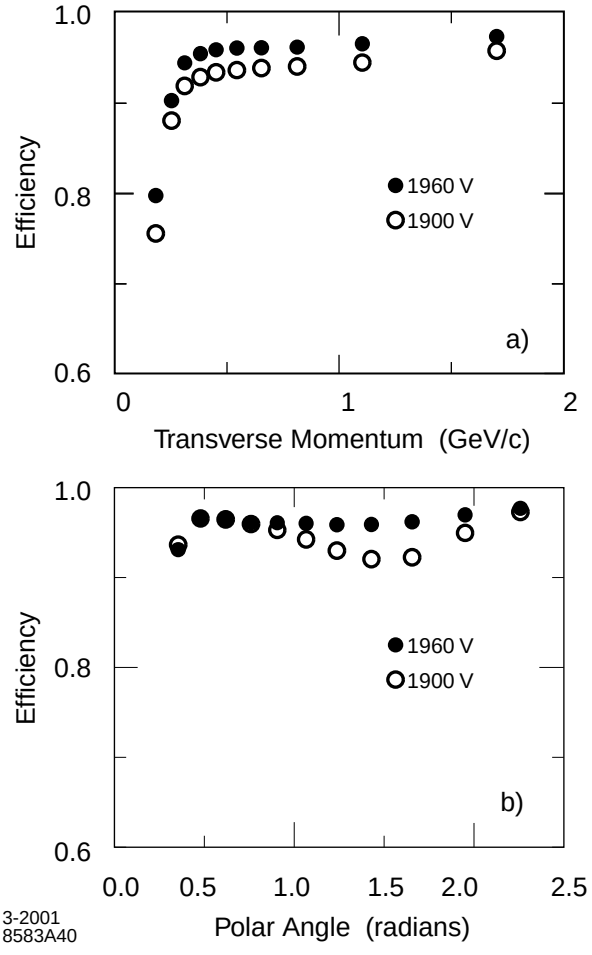

Figure 2.8: *Tracking efficiency for the DCH shown as a function of p_T (top) and of polar angle (bottom). The plot shows points for two voltages used in BABAR Run 1, 1960*V *and 1900*V*.*

Figure 2.8 shows the track reconstruction efficiency calculated by comparing the number of SVT tracks that fall within the DCH acceptance with the number of DCH tracks. This determination is corrected for fake SVT tracks. The figure shows the efficiency as a function of both transverse momentum and polar angle for both the design voltage of 1960 V and for 1900 V. A small section of the DCH was damaged during commissioning and so for the early part of *BABAR* Run 1 the chamber was operated at the reduced voltage. After Run 1 the chamber has been operated consistently at 1930 V. At design voltage and at 1930 V the average tracking efficiency, calculated as described above, is $(96 \pm 1)\%$.

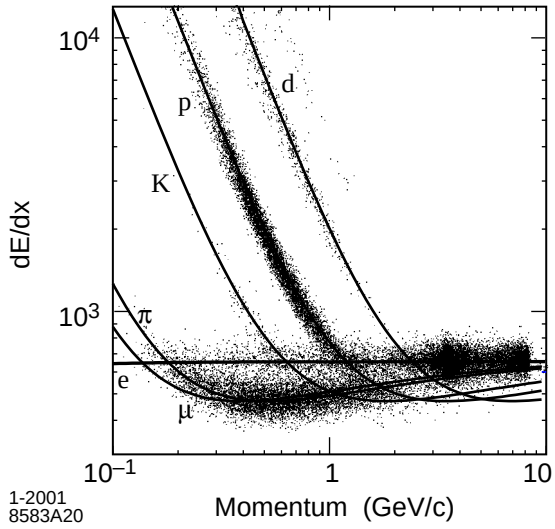

Figure 2.9: $\mathrm{d}E/\mathrm{d}x$ *measurements in the DCH shown as a function of track momentum. The overlaid curves are Bethe–Bloch predictions calculated from control samples of each of the labelled particle types.*

The distribution of $\mathrm{d}E/\mathrm{d}x$ measurements as a function of track momentum is shown in Figure 2.9. The Bethe–Bloch [2] predictions calculated from control samples of each of the labelled particle types are overlaid and demonstrate that good K/π separation can be achieved up to a momentum of 0.6 GeV/c. The $\mathrm{d}E/\mathrm{d}x$ resolution for e^+e^- events is 7.5%, which is almost at the design goal of 7.0%.

The transverse momentum resolution determined from cosmic ray muons is found

to be well described by the function

$$\sigma_{p_T}/p_T = (0.13 \pm 0.01)\% \cdot p_T + (0.45 \pm 0.03)\% \tag{2.1}$$

where p_T is the transverse momentum in units of GeV/c. Furthermore this is in good agreement with Monte Carlo simulations and close to the design resolution.

2.6 The Detector of Internally Reflected Cerenkov light (DIRC)

2.6.1 DIRC Physics Requirements

Time dependent *CP* asymmetry measurements require that the flavour of the other B meson in the event, *i.e.* the one that is not reconstructed in a *CP* eigenstate, be tagged using information about its decay products. One of the best ways of achieving this is to identify charged kaons from the cascade decay $b \to c \to s$. These kaons are produced with momenta up to 2 GeV/c. Kaon-pion separation is essential for rare B decay analyses, such as the one described in this thesis, in order to isolate the correct final state. In these analyses the final state particles can have a wide range of momenta up to around 4 GeV/c. As seen in Section 2.5.3 the DCH can only provide effective separation up to 700 MeV/c and so there must be a further system for providing charged particle identification (PID) in the momentum range $0.7 - 4.2$ GeV/c. This system must also be able to complement the IFR in identifying muons with p_T less than 750 MeV/c where it is less efficient.

This PID detector must be small both in terms of radiation lengths so as not to impact the resolution of the EMC and in terms of physical size in the radial direction so that the EMC does not have too large an internal radius, thereby minimising the cost of the most expensive part of the detector. In order to operate in the high luminosity environment of PEP-II it must have a fast signal response and be able to operate in high backgrounds.

2.6.2 DIRC Design

The DIRC is a ring imaging Cerenkov detector designed primarily to provide 4σ K/π separation over the momentum range $0.7 - 4.2\,\mathrm{GeV}/c$. Its design relies on the principle that the magnitude of an angle is preserved when undergoing reflection from a plane surface. As such, Cerenkov photons produced within the detector volume can be transmitted by total internal reflection to photomultiplier tubes (PMTs) placed outside the detector acceptance.

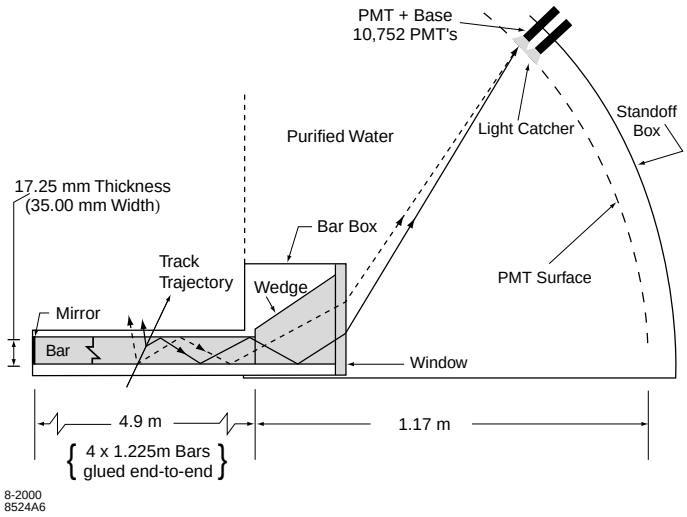

Figure 2.10: *Structure and concept of the DIRC.*

A schematic of the DIRC principle is shown in Figure 2.10. 144 synthetic quartz bars are arranged into a 12-sided barrel. When a charged particle, travelling with velocity βc, passes through one of the bars it will emit Cerenkov photons if $\beta > 1/n$, where $n = 1.473$ is the refractive index of the quartz. These photons will be emitted in a cone with opening angle θ_c, where $\cos\theta_c = 1/n\beta$. The angle ϕ_c is the azimuth angle of an emitted photon around the direction of the track. Some photons will be trapped by total internal reflection and travel forward or backward down the bar depending on the incident angle of the particle. Forward moving photons are reflected by a mirror so that only the backward end of the DIRC is instrumented. This makes room for the EMC forward endcap and reduces the background levels

in the DIRC instrumentation.

Arriving at the backward end of the bar the photons enter an expansion region filled with 6,000 litres of purified water, known as the standoff box. The purified water is chosen because it has a refractive index very close to that of the quartz, thereby minimising total internal reflection at the boundary of the bars and the standoff box. A wedge of quartz placed at the entrance to the standoff box reduces the required size of the detection surface at the cost of introducing an ambiguity by reflecting photons at large angles to the bar axis as well as folding one half of the image onto the other. The photons are detected by an array of 10,752 PMTs surrounded by "light catcher" cones, which increase the active detection area to 90% of the total. The standoff box is shielded from the magnet to reduce its effect on the PMTs. The expected Cerenkov light pattern on the PMT surface is a conic section with the opening angle being the Cerenkov angle modified by refraction at the quartz/water boundary. The Cerenkov angles θ_c and ϕ_c are determined up to a 16-fold ambiguity: top/bottom, left/right, forward/backward and wedge reflection/no wedge reflection. The arrival time of the signal is used to resolve the forward/backward and wedge ambiguities as well as to suppress hits from beam background and other tracks in the event. Pattern matching during reconstruction can further reduce the ambiguity.

The DIRC has an acceptance of 83% in the polar angle and 94% in the azimuth. It has a thickness (including supports) of just 8 cm in the radial direction and accounts for only 17% of a radiation length for tracks with normal incidence.

2.6.3 DIRC Performance

Di-muon events can be used to determine the Cerenkov angle and time resolutions. These can then be used to infer the K/π separation power of the DIRC by using the expected Cerenkov angles of kaons and pions. The angular resolution of a single DIRC photon is 10.2 mrad and the timing resolution is 1.7 ns, which is close to the intrinsic transit time spread of the PMTs (1.5 ns). The Cerenkov angle resolution

for a track is 2.5 mrad, which gives a K/π separation of just over 4σ at 3 GeV/c. The K/π separation as a function of track momentum can be seen in Figure 2.11.

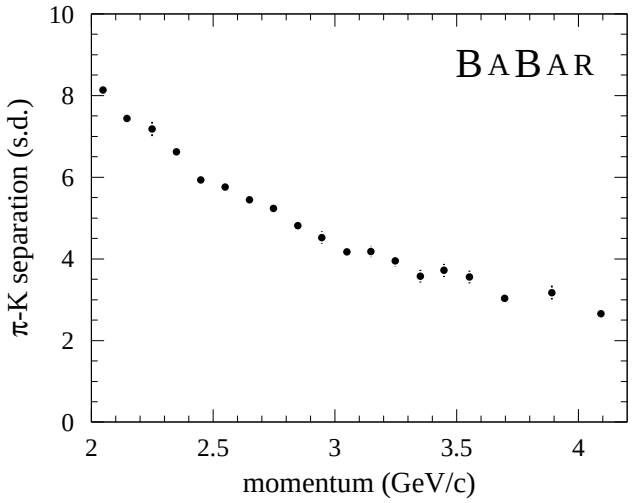

Figure 2.11: *DIRC K/π separation as a function of track momentum.*

Figure 2.12 shows the effect of using the DIRC information in kaon identification. The peak in the $K\ \pi$ spectrum corresponds to the decay $\overline{D}^0 \to K^+\pi^-$. The combinatorial background is seen to greatly reduce when DIRC information is used, while the signal is unaffected.

2.7 The Electromagnetic Calorimeter (EMC)

2.7.1 EMC Physics Requirements

There are many important B decay modes which include one or more π^0 or η particles, which in turn decay to photons. 50% of the time these photons have energies less than 200 MeV. As such the EMC must be able to detect and measure photons down to 20 MeV. At the other extreme the photons produced in processes such as $e^+e^- \to e^+e^-\gamma$ and $e^+e^- \to \gamma\gamma$, which are important for calibration and luminosity

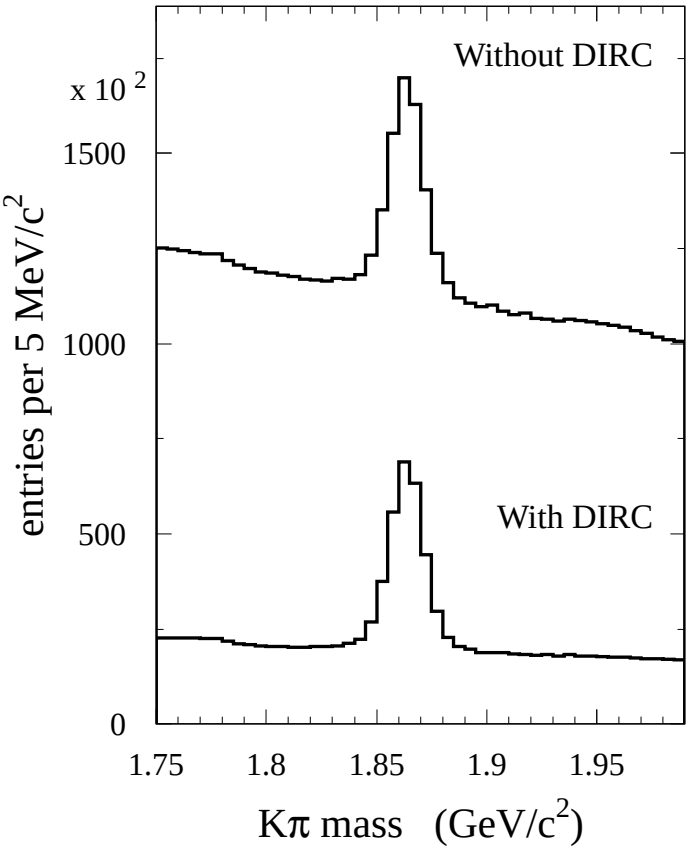

Figure 2.12: *Reconstructed $K\ \pi$ mass with and without the use of DIRC information for kaon ID. The peak corresponds to the decay $\overline{D}^0 \to K^+\pi^-$.*

monitoring, can have energies as high as 9 GeV in the laboratory frame. Consequently the EMC is required to detect electromagnetic showers with good energy and angular resolution and with excellent efficiency over a wide range of energies. The EMC also has a very important role in electron identification, which is essential for flavour tagging in time dependent *CP* asymmetry measurements and in semi-leptonic B decays.

2.7.2 EMC Design

The EMC consists of 6580 Caesium Iodide crystals doped with Thallium formed into a barrel and forward endcap as shown in Figure 2.13. CsI (Tl) was chosen

because it has a high light yield, providing excellent energy resolution, and a small Molière radius, which provides excellent angular resolution. The EMC has complete coverage in the azimuthal angle and covers 90% of the solid angle in the CM frame. All crystals are angled to point back to the IP. The 5760 barrel crystals are arranged into 48 rows in θ and 120 rows in ϕ. To prevent shower leakage from the more energetic Lorentz boosted particles in the forward direction the crystals are longer, 17.5 radiation lengths (32.4 cm) as opposed to 16 radiation lengths (29.6 cm) in the backward direction. The 820 endcap crystals are arranged into 8 rows in θ, 3 of which have 120 rows in ϕ, 3 of which have 100 rows and 2 of which have 80 rows. All the endcap crystals are 17.5 radiation lengths except for those in the innermost ring, which are shorter by 1 radiation length due to space constraints. There is another ring inside the innermost ring of crystals that contains lead shielding to reduce the effect of machine background on the endcap crystals. The face size of the crystals is $\sim 5\,\mathrm{cm}^2$ to correspond to the Molière radius and as such the electromagnetic showers will spread over several adjacent crystals, forming a "cluster".

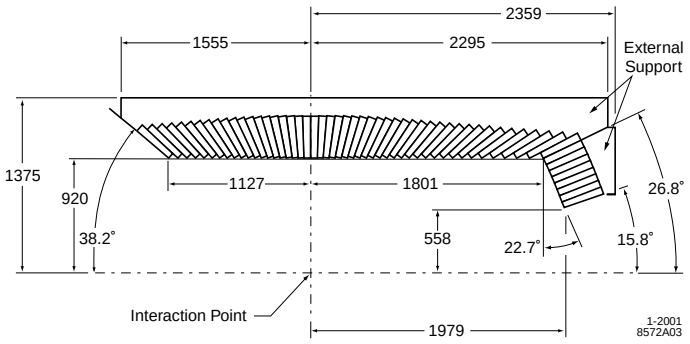

Figure 2.13: *Side on view of the EMC showing only the top half - the detector is rotationally symmetric about the z-axis.*

The crystals are read out using a pair of silicon PIN diodes glued to the back of the crystal. The diodes, which have a quantum efficiency of 85%, are connected to low-noise preamplifiers that shape and filter the signal, which is then digitised and read out in a continuous stream. On receipt of a trigger the data in a $1\,\mu$s window undergoes processing to determine the crystal energy and peak time. The EMC

crystal data is also continuously summed into blocks of crystals called "towers" and passed, every 269 ns, to the Level 1 Trigger system.

2.7.3 EMC Performance

Calibration of the EMC system occurs in two stages. The first determines the relation between the measured signal in each crystal and the actual deposited energy. Light yields can vary significantly from crystal to crystal, as well as being non-uniform as a function of energy. Radiation damage can also affect this relation over the life of the detector. Low energy calibration is performed using 6.13 MeV photons generated from a radioactive source within the detector. High energy calibration is performed using Bhabha events where the $e^{\pm}$ energy can be predicted from its polar angle. The second stage determines the relation between the cluster energy and the energy of the incident particle. Corrections must be applied for crystal leakage, absorption in material in front of the EMC and between crystals, as well as energy in the crystals that is not associated with the incident particle. This correction is applied as part of the offline reconstruction process (Section 3.2) and is derived, as a function of cluster energy and polar angle from π^0 and η decays.

The energy resolution of the EMC can be described by the empirical relation

$$\frac{\sigma_E}{E} = \frac{a}{\sqrt[4]{E(\,\mathrm{GeV})}} \oplus b \tag{2.2}$$

where E and σ_E are the energy of a photon and its RMS error measured in GeV and a and b are constants to be determined. The energy dependent term results mainly from fluctuations in photon statistics but also from electronics noise. The constant term results from crystal leakage, absorption, non-uniformities and uncertainties in the calibration methods. As with the calibrations, the resolution is measured using the radioactive source at low energies and Bhabha events at high energies, while in the intermediate range physics processes such as π^0 decays are used. Figure 2.14 shows the EMC energy resolution as a function of energy for some of these processes.

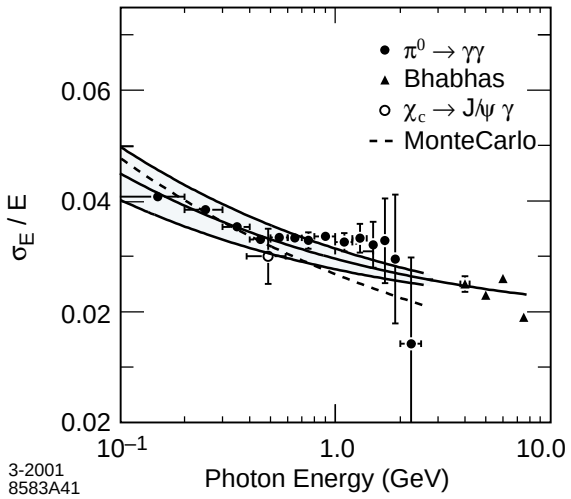

Figure 2.14: *Energy resolution of the EMC measured for photons and electrons as a function of energy. The middle solid curve is a fit to Eq. (2.2) while the upper and lower solid curves are the RMS error on the fit.*

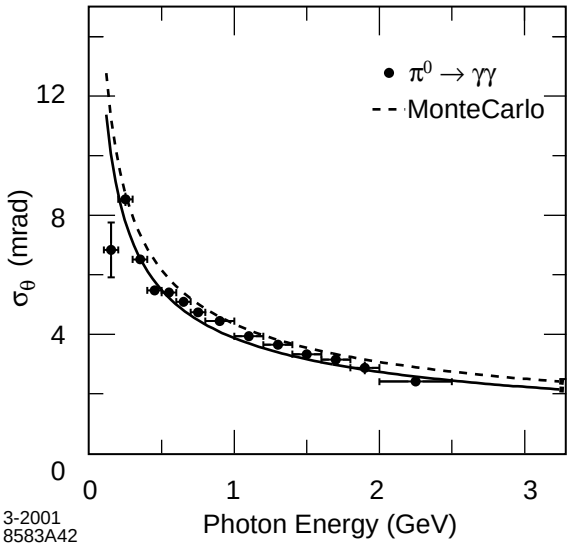

Figure 2.15: *Angular resolution of the EMC for photons from π^0 decays measured as a function of energy. The solid curve is a fit to Eq. (2.3).*

Fitting Eq. (2.2) to these data yields the following values for the constants: $a = (2.3 \pm 0.4)\%$, $b = (1.9 \pm 0.1)\%$. These values are slightly worse than the design goals but agree quite well with detailed Monte Carlo studies which include the effects of

machine backgrounds and electronics noise.

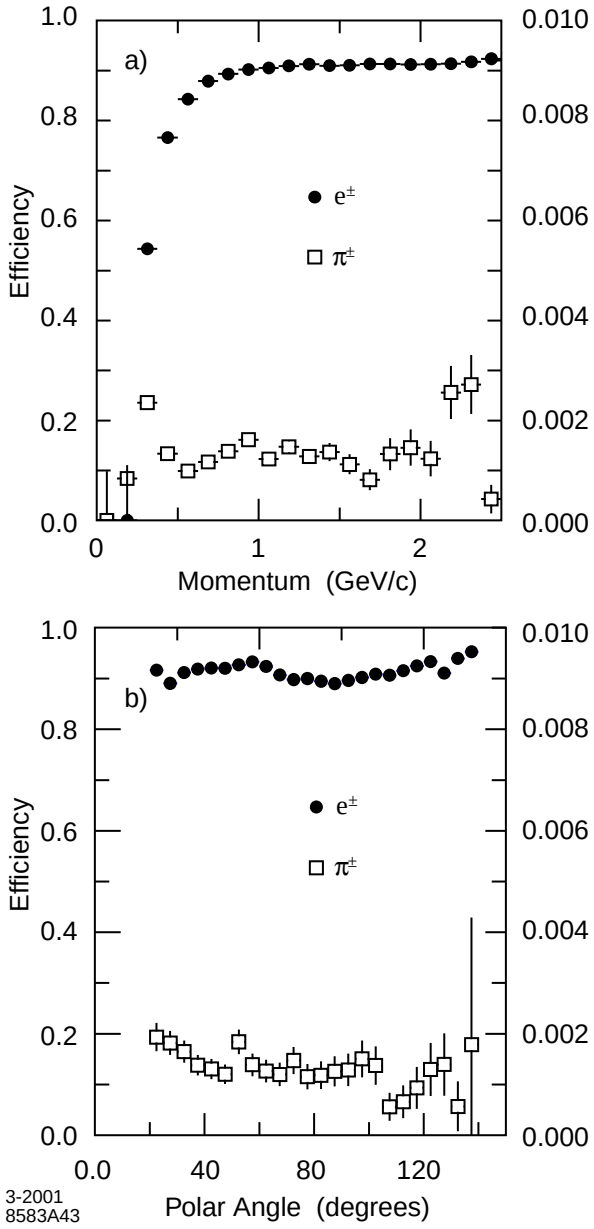

Figure 2.16: *Electron efficiency (left scale) and pion misidentification probability (right scale) as a function of a) the particle momentum and b) the polar angle in the laboratory frame.*

The angular resolution of the EMC is governed by the crystal size and the distance

from the IP. It can be described by the empirical relation

$$\sigma_\theta = \sigma_\phi = \frac{c}{E(\,\mathrm{GeV})} + d \tag{2.3}$$

where c and d are constants to be determined. Analysis of π^0 decays to two photons of approximately equal energy is used to determine the constants. Figure 2.15 shows the angular resolution as a function of photon energy. Fitting Eq. (2.3) to these data yields the following values for the constants: $c = (3.9 \pm 0.1)\,\mathrm{mrad}$, $d = (0.00 \pm 0.04)\,\mathrm{mrad}$. These values are slightly better than those predicted from the Monte Carlo studies.

Electron identification uses information from the measurements of shower energies, shower shapes and track momentum. The most important variable is E/p, the ratio of the recorded calorimeter energy (E) to the track momentum (p) measured in the SVT and/or DCH. Electrons have a value of E/p of around 1 since on entering the EMC they produce an electromagnetic shower consisting of photons, electrons and positrons, which combined deposit the full energy of the original electron. Since electrons are very light this full energy is approximately equal to their momentum

$$E^2 = p^2 + m^2 \tag{2.4}$$

$$E^2 \approx p^2 \tag{2.5}$$

$$\frac{E}{|p|} \approx 1 \tag{2.6}$$

Muons are the other extreme and only deposit energy as minimum ionising particles (MIPs). Charged hadrons, such as pions, can pass through simply as MIPs or can interact, producing an hadronic shower that deposits a fraction of their energy. The behaviour of hadrons has a strong energy dependence. Hadronic showers and electromagnetic showers have different longitudinal and lateral shapes, permitting further discrimination. Figure 2.16 shows electron efficiency and pion misidentification probabilities derived from radiative Bhabha events and reconstructed K^0_S and τ decays.

2.8 The Instrumented Flux Return (IFR)

2.8.1 IFR Physics Requirements

Identification of muons is essential for many time dependent *CP* asymmetry analyses since the J/ψ is reconstructed in its decay to e^+e^- or $\mu^+\mu^-$. Muons are also used in flavour tagging of the other B meson through semi-leptonic decays. Detection of neutral hadrons, particularly K^0_L, is also very important for *CP* analyses since it increases the number of *CP* eigenstates that can be reconstructed. This both increases the statistics available from a given data set and allows study of eigenstates with opposite eigenvalue, such as $J/\psi\, K^0_S$ and $J/\psi\, K^0_L$.

The IFR is required to identify muons, with good efficiency and high background rejection, with a minimum momentum of $1\,\mathrm{GeV}/c$. It must also be able to detect neutral hadrons with high efficiency and good angular resolution. The solid angle coverage must be good and due to the size and inaccessibility of the detector it must have high reliability and extensive monitoring of the detector systems and electronics.

2.8.2 IFR Design

The IFR acts as both a flux return for the 1.5 T magnetic field and a support structure for the rest of the *BABAR* detector. The steel of the flux return is segmented into layers from 2 cm thickness at the inner radius to 10 cm thickness at the outer radius. These thicknesses were chosen after extensive Monte Carlo simulation studies to optimise muon filtering and hadron absorption. The steel layers are interleaved with resistive plate chambers (RPCs). The detector is arranged in a hexagonal barrel with a forward and backward endcap, as shown in Figure 2.17. The detector covers a solid angle extending to 300 mrad in the forward direction and to 400 mrad in the backward direction. There are 19 RPC layers in the barrel, each layer in each

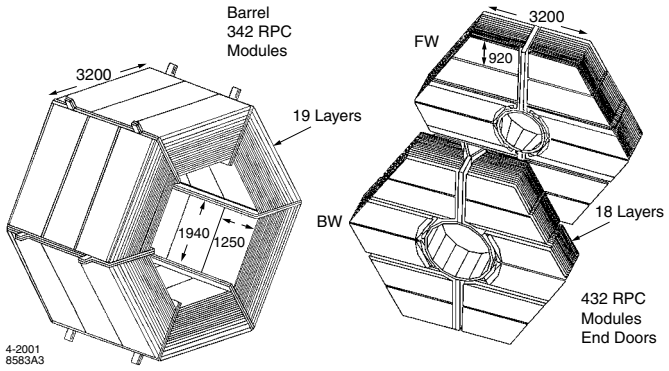

Figure 2.17: *Mechanical structure of the IFR, showing the hexagonal barrel (left) and forward (FW) and backward (BW) endcaps.*

side of the barrel is split into 3 modules in the z direction. In the endcaps there are 18 layers split vertically in half, with each half containing 6 modules. In addition to these there are two cylindrical RPC layers between the EMC and the magnet cryostat in order to detect particles leaving the EMC and link tracks and/or EMC clusters to IFR clusters. These layers are split into 4 quarter cylinder modules.

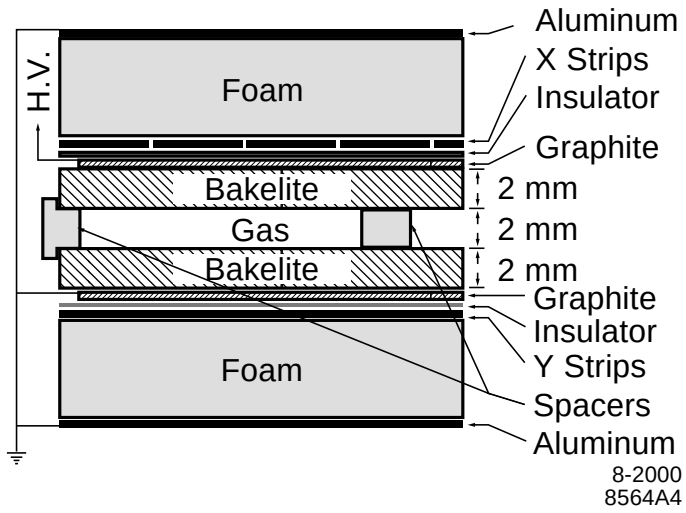

Figure 2.18: *Cross section of an RPC.*

Figure 2.18 shows a cross-sectional view of an RPC, which detect streamers from ionising particles via capacitive readout strips. The electrodes are 2 mm thick plates

of graphite coated Bakelite. The lower electrode is grounded while the upper electrode has an 8 kV high voltage applied to it. A PVC insulator keeps the electrodes separated and parallel, the gap being filled with a gas mixture: 57% argon, 39% freon-134a and 4% isobutane. The aluminium readout strips (labelled X and Y Strips in Figure 2.18) are arranged orthogonally to give, together with the finite radial thickness of the RPC, three dimensional position information. In the barrel the strips measuring z position have a pitch of 3.85 cm while those measuring position in ϕ have a pitch of between 1.97 and 33.5 cm. In the endcaps the x strips have a pitch of 3.8 cm while the y strips have one of 2.83 cm.

The signals from 16 readout strips are passed to a Front End readout Card (FEC), which shapes the signals and then compares them to a threshold to determine whether the channel is active. Signals from active channels are then digitised. Hit information is passed every 269 ns to the Level 1 Trigger.

2.8.3 IFR Performance

The muon efficiency and pion misidentification probability can be determined using clean control samples of these particles gathered from data. Figure 2.19 shows these quantities for *BABAR* Run 1. A mean muon efficiency of around 90% with a pion mis-ID rate of less than 8% was achieved for the momentum range 1.5 to 3.0 GeV/c.

Neutral hadrons, such as K_L^0, are detected as IFR clusters that are not associated with a charged track. These have a detection efficiency that varies quite considerably from 20 to 40% over the momentum range 1 to 4 GeV/c. The process $e^+e^- \to \phi\gamma \to K_S^0 K_L^0 \gamma$ is used to determine the angular resolution for K_L^0 particles, which is found to be 60 mrad. Matching production angles in the EMC and in the cylindrical RPCs with the IFR clusters can improve this resolution by up to a factor of two.

Over the course of Run 1 it was seen that the muon efficiency was degrading rapidly in many RPCs. Initially the problem was traced to overheating and some RPCs

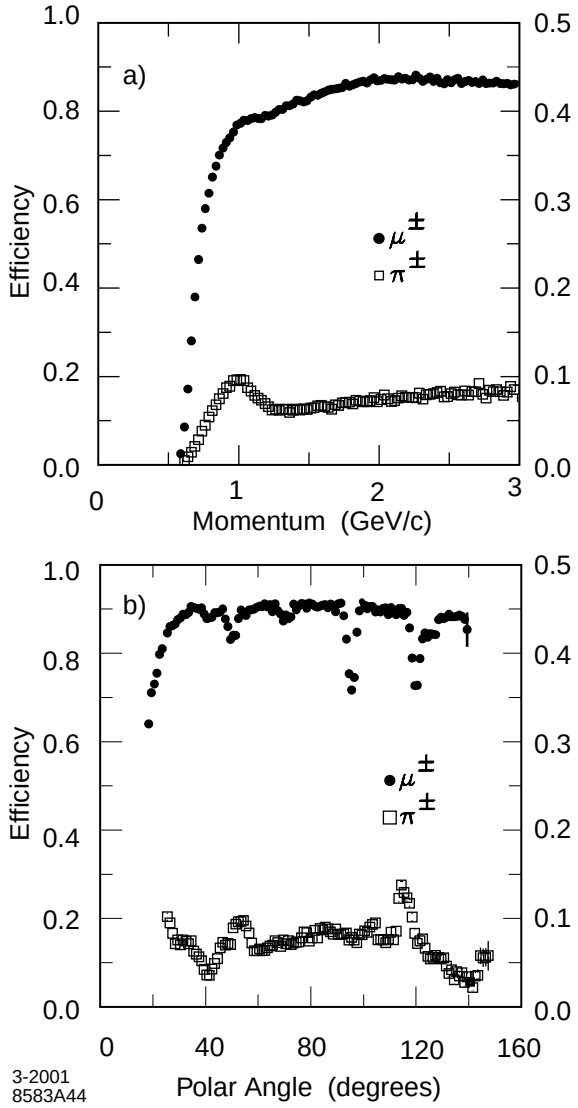

Figure 2.19: *Muon efficiency (left scale) and pion misidentification probability (right scale) as a function of momentum (top) and polar angle (bottom).*

were disconnected before additional cooling was installed. However, even after this a growing number of RPCs continued to show reductions in efficiency, some of which eventually became "dead", *i.e.* had less than 10% efficiency. During the shutdown between Run 1 and Run 2 the dead RPCs in the forward endcap were replaced. The RPCs removed from the detector were closely inspected to try and determine the cause of the degradation. The Bakelite in the RPCs was treated with linseed oil

and in some of the dead chambers it showed signs of having formed droplets which could have caused sparking. However, not all chambers exhibited this behaviour. Others were found to have gas supply problems but no complete understanding of the problems was achieved.

During Run 2 the problem continued and so attempts at remediation were made. These involved flushing the chambers with pure argon whilst applying a very high voltage (500 kV) with the opposite polarity to normal running. This was found to help RPCs that had only degraded a little but offered no help to already badly affected chambers. By the end of Run 2 the muon efficiency had dropped to around 65%. A long term solution clearly had to be sought out quickly.

Two different approaches were taken for the endcap and the barrel. For the endcap the RPCs were replaced with more efficient double-gap chambers and several active layers were replaced with brass in order to increase the absorbency. This was intended to lead to improved muon detection without badly impacting the K_L^0 detection. This upgrade was performed during the summer shutdown in 2002. For the barrel it was decided also to replace six active layers with brass and the remaining RPC layers with Limited Streamer Tubes, which are described in [42]. The installation of the first two sextants was completed during the 2004 summer shutdown and the remaining four sextants will be installed during the next long shutdown, originally scheduled for summer 2005 but which may now be delayed until summer 2006.

2.9 The Trigger (TRG)

The *BABAR* trigger is designed to accept interesting physics events with a high, stable and well understood efficiency whilst rejecting background, thereby reducing the data flow to a manageable rate for logging and storage. *CP* violation studies require that the trigger efficiency for $B\overline{B}$ events be greater than 99% and that for

$q\overline{q}$ events be greater than 95%. Secondary physics goals require that the trigger efficiency for $\tau^+\tau^-$ events also be greater than 95%. Processes such as Bhabha scattering, which are important for luminosity measurements must have a trigger efficiency which is known to better than 0.5%.

The trigger is implemented in two stages, the Level 1 hardware trigger that is designed to retain nearly all physics events whilst rejecting background, and the Level 3 software trigger that then selects the physics events of interest. The system is designed to accommodate up to ten times the PEP-II background rates at design luminosity and to degrade slowly above this rate. Triggers are produced within a fixed latency window of $11 - 12\,\mu$s after bunch crossing.

2.9.1 Level 1 Trigger (L1T)

The Level 1 Trigger is designed to select events with a rate of around 1 kHz at design luminosity. It consists of a DCH trigger (DCT), an EMC trigger (EMT), an IFR trigger (IFT) and a global trigger (GLT). The DCT, EMT and IFT constantly receive data from their parent systems and produce trigger *primitives*, which are summaries of the data in terms of position and energy or momentum. These primitives are passed to the GLT which combines them to form trigger lines that are indicators of certain physics processes. Any active triggers that correspond to the time of a bunch crossing are sent to the Fast Control and Timing System (FCTS), which has the ability to prescale or mask triggers. If any trigger remains then a Level 1 Accept (L1A) is issued, causing all the detector subsystems (including the trigger itself) to read out their event buffers. The 24 trigger lines are arranged to give priority to high multiplicity multi-hadronic events while processes such as Bhabhas, which occur more frequently and are required only for calibrations, are prescaled in order to reduce the Level 1 rate. The trigger logic, masks and prescales are all configurable on a run-by-run basis.

The DCT contains three different types of trigger board, the Track Segment Finder

(TSF), the Binary Link Tracker (BLT) and p_T Discriminant (PTD). The TSF looks for sets of adjacent DCH hits in a group of eight cells in a superlayer known as a *pivot group*. The BLT tries to link track segments to form tracks. If a track can be formed that reaches the outermost superlayer it is called a long track, whilst one that reaches at least half way through the chamber is called a short track. The PTD examines segments found in axial superlayers to determine whether they are consistent with being part of a track with p_T greater than a threshold value, typically 800 MeV/c. The primitive definitions for the DCT are listed in Table 2.2 along with those for the EMT.

Table 2.2: *Definition of DCT and EMT trigger primitives. The threshold values are configurable and those shown here are typical values.*

Primitive	Origin	Description	ϕ Segmentation	Threshold
B	DCT	Short track reaching superlayer 5	16	120 MeV/c
A	DCT	Long track reaching superlayer 10	16	180 MeV/c
A′	DCT	High p_T track	16	800 MeV/c
M	EMT	All-θ MIP energy	20	120 MeV
G	EMT	All-θ intermediate energy	20	307 MeV
E	EMT	All-θ high energy	20	768 MeV
X	EMT	Forward endcap MIP energy	20	100 MeV
Y	EMT	Backward barrel high energy	10	922 MeV

The EMT has only one type of trigger board, the Trigger Processor Board (TPB). The TPBs receive energy samples from 280 EMC towers (Section 2.7.2). These are summed over the polar angle to form 40 "ϕ strips", which are then summed with their nearest neighbour and a simple feature extraction is applied to find the energy and time of the peak in the waveform. The peak energy is then compared to thresholds corresponding to physics processes as defined in Table 2.2 in order to

define three trigger primitives. Two further primitives are defined that additionally discriminate position in the polar angle. Specifically they single out MIP hits in the forward endcap and high energy hits in the backward barrel.

The IFT is only used to trigger on $\mu^+\mu^-$ events and cosmic ray muons for calibration and diagnostic purposes. The IFT primitives simply correspond to single clusters or pairs of back to back clusters with the further information of whether they are located in the barrel or endcap.

The DCT and EMT each nearly satisfy the trigger requirements independently, each having an efficiency for $B\overline{B}$ events of over 99%. This allows their efficiencies to be studied in detail by using events triggered by the other system. Together they have an efficiency of over 99.9%.

2.9.2 Level 3 Trigger (L3T)

The goal of the Level 3 Trigger is to reduce the 1 kHz Level 1 rate to around 100 Hz at design luminosity. The Level 3 code runs on the large Online Event Processing (OEP) computing farm, events being distributed one per node at any given time. The OEP farm also performs data quality monitoring of the events.

All the event information is available to the Level 3 Trigger, meaning that it is able to employ more sophisticated algorithms to the event data, which contain better positional information and increased energy and momentum resolution, in order to make its decision. Timing information is used to reject backgrounds from other beam crossings while analysis of track impact parameters can help reject machine backgrounds that do not originate from the primary vertex. A series of algorithms are run that the event passes or fails, thereby classifying the event into various physics categories as well as cosmic ray, Bhabha and other types used for calibration and monitoring. The Level 3 output lines are then formed from logical combinations of the algorithm outputs, much as the GLT forms trigger lines from the Level 1

primitives.

Level 3 output lines can be prescaled to reduce the rate at which certain processes are recorded, for example Bhabha events are required for calibration and luminosity measurements but not at the rate at which they occur and so prescaling is applied. In order to allow calculations of efficiency some events that do not pass Level 3 are accepted anyhow at a certain prescaled rate. These events are known as "L1 Pass-Through" events. All events that are accepted by Level 3 are logged to disk.

2.10 The Data Acquisition System (DAQ)

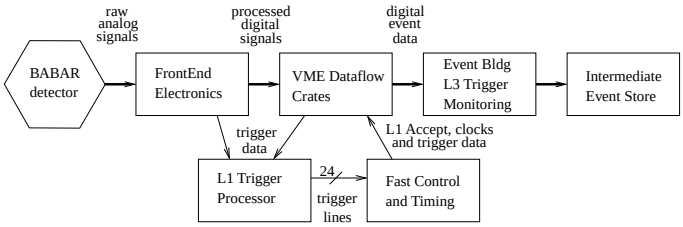

Figure 2.20: *Schematic of the BABAR DAQ system.*

Figure 2.20 shows a schematic of the *BABAR* DAQ. Following the initial processing of the raw detector output by the subsystem Front End Electronics, briefly described in the previous sections, the digitised signals are sent over fast fibre optic links to VME dataflow crates containing the dataflow Read Out Modules (ROMs). For the DCH and IFR these digitised signals are also continuously sent to the DCT and IFT respectively. For all systems except for the EMC the ROMs contain Triggered Personality Cards (TPCs), meaning that the signals are only collected from the FEE on receipt of an L1A from the FCTS. For the EMC however, the ROMs connected to the FEE contain Untriggered Personality Cards (UPCs), meaning that the signals are continuously received from the FEE, processed and, on receipt of an L1A, passed to another TPC ROM. The UPCs also create the tower sums that are continuously sent to the EMT.

The TPC ROMs run subsystem specific software that performs a feature extraction (FEX) that attempts to isolate signals and suppress background and noise. The ROMs and other boards in the dataflow crates are configurable on a run by run basis. This is achieved by using the configuration database in which system specific configuration objects are stored. The data are then passed to the OEP farm for further processing by the Level 3 Trigger and data quality monitoring. Events passed by Level 3 are written to temporary files, which are then picked up by the Offline Prompt Reconstruction (OPR) farms. Information on detector conditions, such as temperature, voltages, gas supply and humidity are extracted from the ROMs and placed in the conditions database for later use in the event reconstruction by OPR. Both the conditions and configuration databases use Objectivity^{TM} [43] technology.

3

Analysis Techniques

3.1 Introduction

This chapter will describe the various tools and techniques used in this analysis. Many of these are used in most *BABAR* analyses, and some throughout the high energy physics community.

The scale and complexity of the *BABAR* detector combined with the high luminosities provided by PEP-II mean that the volume of recorded data is immense. Without a centrally managed processing system it would be impossible for individual members of the collaboration to analyse the full data sample. Interpretation of the data also requires large numbers of simulated events for comparison.

The small branching fractions that are expected in charmless B decays mean that very small numbers of signal events have to be isolated from often large numbers of background events. In order to achieve this several powerfully discriminating variables have been devised along with statistical techniques for employing them.

3.2 Reconstruction

Reconstruction of events takes place in two parts. The first part is known as Offline Prompt Reconstruction (OPR) during which charged tracks and calorimeter clusters are reconstructed from the raw detector hits. Particle identification selectors are also formed using the information from the tracking system and the DIRC. Data quality monitoring and rolling calibrations are also performed. The OPR processing is performed in two stages on several large computer farms. The first stage, which simply runs the rolling calibrations and some data quality monitoring is run within a few hours of the events being logged to disk. The second stage, which runs the full reconstruction routines, is usually completed within a few days of the events being logged. At the end of this stage the data are stored in an object-oriented database system, which formerly made use of Objectivity$^{\text{TM}}$ technology but now uses a *BABAR* designed system based on `Root`. These are collectively known as the "event store". The second part of the reconstruction process involves combining the information from OPR to form particle candidates from their decay products. This is achieved using a series of analysis packages based on a common framework.

3.2.1 Tracking Algorithms

The track reconstruction algorithms employed in OPR use the data from the SVT and DCH as well as the tracks formed by the Level 3 trigger. Charged tracks are described using five quantities, all of which are defined at the point of closest approach (POCA) of the track to the z-axis

- z_0 - the distance in the z direction to the co-ordinate system origin
- d_0 - the distance in the x–y plane to the z-axis
- ϕ_0 - the azimuthal angle of the track
- $\tan\lambda$ - the tangent of the dip angle of the track with respect to the x–y plane
- $\omega = 1/p_T$ - the track curvature

The Level 3 tracks are used as a starting point for the OPR algorithm. A Kalman fitting technique [44] that accounts for detector material distribution and local magnetic field variations is used on the hits that make up the L3 tracks. Further DCH hits that are consistent with these tracks are added to them and the fit is performed again. This yields a refined value for the collision time t_0. After this the remaining DCH hits are searched in order to find tracks that did not originate from the IP (such as those from secondary particles *e.g.* K^0_S) or do not cross the whole chamber.

All DCH tracks are then extrapolated into the SVT, accounting for material and magnetic field, and all consistent SVT hits are added to them. An SVT track finder is then run on the remaining SVT hits in order to find low momentum, SVT-only tracks. Finally these SVT tracks are projected into the DCH in an attempt to combine tracks that were scattered by the support structure of the SVT. The efficiency and performance of these tracking algorithms is discussed in Section 2.5.3. The tracks are placed into "lists" in the event database entry depending on the quality of the track. The track list used in this analysis is the `GoodTracksLoose` list which has the following requirements:

- A minimum transverse momentum of $0.1\,\mathrm{GeV}/c$,
- a maximum momentum of $10.0\,\mathrm{GeV}/c$,
- at least 12 hits in the drift chamber,
- $d_0 < 1.5\,\mathrm{cm}$

- $z_0 < 10\,\mathrm{cm}$

3.2.2 Calorimeter Algorithms

The EMC reconstruction algorithms attempt to combine crystals into clusters that correspond to individual particle showers. They begin by searching for crystals with energy greater than 10 MeV. Any neighbouring crystals with energies greater than 1 MeV are added to the cluster. Further crystals are then added if they meet this energy requirement or if they neighbour a crystal that is already included in the cluster that has an energy greater than 3 MeV. This process is iterated until no further crystals meet the requirements.

Once the cluster is completed a "bump" finding algorithm is run over all its constituent crystals. This algorithm is designed to find local maxima within the cluster since a single cluster may be caused by two or more overlapping showers. Charged tracks, reconstructed as in Section 3.2.1, are projected onto the inner face of the EMC. There is then an attempt to associate each track with a bump by comparing their separation distance with a threshold. If a track and a bump are associated in this way then they are considered together in all further reconstruction routines. Bumps not associated with tracks are considered to originate from neutral particles and are placed in a list analogous to the `GoodTracksLoose` list for tracks.

3.2.3 Particle Identification (PID)

The next stage in the reconstruction process is particle identification. The five types of particle that may be detected as a charged track in the *BABAR* detector are pions, kaons, electrons, muons and protons. PID can potentially use data from all of the detector subsystems, which are combined to form particle *selectors*. Each selector uses probability density functions (PDFs) to form a per-track likelihood for

its particle type.[1] There is no specific selector for pions, which are the vast majority of charged tracks in a multi-hadronic event, and so tracks that fail the kaon selector are generally assumed to be pions. The analysis described in this thesis only makes use of the kaon and electron selectors, which are described briefly here. All PID selectors have been developed and maintained by the *BABAR* PID group. Further details can be found in [45, 46].

3.2.3.1 Kaon Identification Selector

The kaon identification algorithms make use of the Cerenkov angle and measured number of photons in the DIRC as well as $\mathrm{d}E/\mathrm{d}x$ information from the SVT and DCH. It is assumed that the PDFs from these sources are uncorrelated with one another and that the total likelihood can be formed by taking their product.

The Cerenkov angle is used by comparing the measured angle and the expected angle (Section 2.6.2) for the given particle type and track momentum. The difference in these two quantities is divided by the experimental error on the angle measurement to give a "pull". The distribution of this pull is Gaussian and the PDF is calculated using control samples, such as $\phi \to K^+K^-$. For low momentum tracks, which are near the Cerenkov emission threshold, there will be a much smaller number of photons emitted, making it hard to get a good measurement of the Cerenkov angle. Instead, the number of measured photons is used to form a likelihood since this follows a Poisson distribution whose mean depends on particle type, momentum and polar angle.

The $\mathrm{d}E/\mathrm{d}x$ PDFs are also derived from Gaussian pull distributions of the measured and expected quantities. The expected values are modelled as a function of momentum by approximate Bethe–Bloch functions as seen in Figure 2.9. The pull distributions are again obtained from data control samples.

The *BABAR* "SMSKaonSelector" forms a combined DIRC likelihood from the prod-

[1] Section 3.6 contains more information on PDFs and likelihood methods.

uct of the Cerenkov and photon likelihoods. It then creates likelihood ratios from each of the SVT, DCH and DIRC PDFs for different particle hypotheses. Tracks then pass or fail the selector depending on whether they satisfy particular cuts on these ratios. The values of the cuts depend on what mode the selector is running in: *NotAPion*, *VLoose*, *Loose*, *Tight* or *VeryTight*. These modes represent increasingly tight cuts on the likelihood ratios, leading to a reduced efficiency of the selection but an increased purity of the resulting sample. The performance of the $K\pi$ separation for each of the subsystems is discussed in their relevant sections: 2.4.3, 2.5.3 and 2.6.3.

3.2.3.2 Electron Identification Selector

The electron identification algorithms use $\mathrm{d}E/\mathrm{d}x$ from the DCH, the Cerenkov angle from the DIRC (for tracks with momenta less than $1.5\,\mathrm{GeV}/c$) as well as E/p and the electromagnetic lateral and longitudinal shower shape from the EMC. The EMC variables have been discussed in Section 2.7.3. Loose selections are applied to these variables to separate muons before distributions are determined for each of them using control samples of pions, kaons, electrons and protons.

The DCH $\mathrm{d}E/\mathrm{d}x$ is modelled as it is in the kaon selector (Section 3.2.3.1). The E/p distribution is modelled as a Gaussian with an exponential tail, while the shower shape variables are described by double Gaussian PDFs. For hadrons, correlations between these variables have to be accounted for but for electrons it is reasonable to take them as being uncorrelated. The Cerenkov angle is modelled as in the kaon selector for kaons and protons while for electrons and pions double and triple Gaussians are used, respectively. This is done to account for deviations in the flight direction of the electrons due to bremsstrahlung and for the possibility that pions may decay to muons or emit electrons as they traverse the DIRC. The performance of the electron selector is discussed in Section 2.7.3.

3.2.4 Vertexing of Composite Candidates

Composite candidates are particles that are not directly detected in *BABAR* but are inferred from their decay products. Since this thesis analysis is examining the inclusive decay mode $B^+ \to K^+\pi^-\pi^+$ the only composite candidate that we want to vertex is the B itself. Possible intermediate charmless resonances such as $K^{*0}(892)$ are so short lived that their vertex is indistinguishable from that of the B, their presence can only be inferred by structure in the Dalitz phase space. As such it is expected that the three charged tracks should all originate from the B decay vertex position and that their invariant mass will peak at the B mass.

The *BABAR* vertex fitting routine, `Geokin`, uses an iterative χ^2 minimisation procedure to find the vertex and performs both *geometric* fits (require that the tracks originate from the same point in space) and *kinematic* fits (require that momentum is conserved at the vertex). The fits adjust the track momenta within their measured errors, improving energy and momentum resolution. In this analysis the fits are performed using both pion and kaon hypotheses for each of the tracks. The quantities that are subsequently used are those that result from the fit performed with the hypothesis that matches the chosen PID selector output.

Since the values of the daughter track momenta determine the position of the event in the Dalitz plot it is possible that reconstructed events can fall outside the true kinematic boundary of the plot, which leads to difficulties in performing the amplitude analysis. In order to resolve this situation a second vertex fit is performed to each set of three tracks where they are further constrained to have the invariant mass exactly equal to the world average [2] B mass. This has the effect that the Dalitz plot kinematic constraints are observed by the reconstructed particles and also serves to improve the resolution on the masses of the intermediate resonances. The mass constraint, by construction, makes continuum events appear more B-like in terms of their kinematics. As such, the kinematic variables that are used to discriminate against continuum events (described in detail in Section 3.5.1), are cal-

culated from the unconstrained fit values. Event topology variables (Section 3.5.2) and the Dalitz variables are calculated from the constrained fit values.

3.3 Monte Carlo Simulation

Interpretation of the large amounts of data recorded by the *BABAR* detector is made possible by the use of Monte Carlo (MC) simulated data. This simulated data is the result of full detector simulation followed by the application of the same reconstruction routines as are applied to the actual data. The detector simulation can be considered in three specific parts: generation of the event; simulation of the passage of the event particles through the fabric of the detector and the response of the detection material; response of the detector electronics, including the trigger system.

The first stage is handled by the `EvtGen` package, which simulates the decays of B mesons and other particles and resonances. The detail level is very high, permitting effects of *e.g. CP* violation and interference to be included if requested for certain decay modes. `EvtGen` also interfaces to the `Jetset` program that is used to generate continuum events as well as some B events for which `EvtGen` does not have an implementation.

The second stage is handled by *BABAR* code that makes extensive use of the `GEANT 4` package. This includes a highly detailed model of the *BABAR* detector in terms of geometry and of materials. The behaviour of the particles as they traverse the detector material is simulated including how they trigger the actual detection systems. Each interaction with a detector system is recorded as a "gHit", which allows simulation of the detector signals as well as truth matching to be performed.

The third stage of the model is a full software implementation of the *BABAR* electronics. This simulates the processing of the detector signals through the front end electronics and the dataflow crates to the data acquisition system. It also includes

a full software simulation of the trigger system allowing determination of when an event would be triggered on and stored.

Under the conditions of actual operation of the detector there are machine backgrounds and electronic noise present as well as the physics events. These must also be simulated correctly in order for the MC to provide a good benchmark for comparison with the data. During normal operations the *BABAR* trigger system issues so called cyclic triggers at regular intervals, typically 1 Hz, causing the DAQ system to read out its event buffers. It is unlikely that a physics event is in progress in these randomly selected windows and so they represent a good sample of the background conditions in the detector. These "events" are stored and their data is overlaid with the simulated physics data in order to create a full simulated event.

The final stage of the MC simulation is the reconstruction, which shares code with and is almost identical to the data reconstruction. MC events are also placed in the event store and are used in exactly the same way as data events by the analysis packages except for the presence of the additional truth information.

3.3.1 Efficiency Corrections

A small difference in efficiency is observed when the reconstruction algorithms are applied to samples of MC and to samples of data, most notably in the tracking and PID algorithms. In order to correct for these differences control samples are studied and the efficiency of reconstruction is tabulated for both the data and MC samples in bins of momentum, polar and azimuthal angles and track multiplicity. When MC events are reconstructed these tables are retrieved from a database and used to correct the efficiency for the event. Each such correction has an associated systematic error.

In the case of the tracking tables the value of the ratio of the data to MC efficiency is stored for each track along with the rest of the event information. This number

is used later to correct the reconstruction efficiency. The average value of this correction for the $B^+ \to K^+\pi^-\pi^+$ mode is 0.984 ± 0.024, where the error is a linear addition of 0.8% per track. For PID there are several possible procedures each of which is slightly different; we will discuss here the "tweaking" method. For each track, the data and MC efficiencies are compared. If the MC efficiency is higher than the data efficiency and the track was accepted by the given selector then it will be rejected with a probability of $1 - \frac{\epsilon_{data}}{\epsilon_{MC}}$. If the track had already been rejected by the selector nothing is done. If, conversely, the data efficiency exceeds that of the MC and the track was rejected by the selector then it will be accepted with a probability of $1 - \frac{1-\epsilon_{data}}{1-\epsilon_{MC}}$. Again, if the track had already been accepted then nothing is done. The systematic error for the PID correction is calculated from control sample studies and is found to be 1.4% per corrected track, which add linearly to give a total of 4.2% for the final state which is the subject of this thesis.

3.4 B Counting

For all branching fraction analyses, including the one described in this thesis, it is essential that the total number of $B\overline{B}$ pairs ($N_{B\overline{B}}$) be accurately determined. Since the cross section for $\Upsilon(4S)$ production is not sufficiently well known it is necessary to calculate $N_{B\overline{B}}$ by a method known as "B Counting".

The B Counting method is essentially a weighted subtraction of the number of multi-hadronic events ($N_{\rm MH}$) recorded 40 MeV below the $\Upsilon(4S)$ resonance from the number recorded at the $\Upsilon(4S)$ resonance (CM energy of 10.58 GeV). Since lowering by 40 MeV takes the energy below the $B\overline{B}$ production threshold this difference must be entirely due to $\Upsilon(4S)$ production, once any energy dependence of the continuum cross section has been factored in. Since the on-peak and off-peak samples have different integrated luminosities the ratio of these quantities must also be included in the determination. This is taken as the ratio of the number of $\mu^+\mu^-$ pairs ($N_{\mu\mu}$).

It is assumed that the branching ratio of $\Upsilon(4S) \to B\overline{B}$ is 100%. So $N_{B\overline{B}}$ is given by

$$N_{B\overline{B}} = \frac{1}{\epsilon_{B\overline{B}}} \left(N_{\rm MH}({\rm on}) - N_{\rm MH}({\rm off}) \kappa \frac{N_{\mu\mu}({\rm on})}{N_{\mu\mu}({\rm off})} \right) \tag{3.1}$$

where $\epsilon_{B\overline{B}}$ is the efficiency with which $B\overline{B}$ events pass the multi-hadronic selection cuts (determined from MC simulation) and $\kappa \sim 1$ is a constant that accounts for the energy dependence of the continuum cross section and selection efficiency.

Applying this procedure to the data used in this analysis yields a value of

$$N_{B\overline{B}} = (231.8 \pm 2.6) \times 10^6 \tag{3.2}$$

For further details, including the error calculation, see [47].

3.5 Discriminating Variables

The high levels of background events present in analyses of charmless B decays mean that it is necessary to develop well understood discriminating variables in order to separate the signal from the background. Those that are generally used in *BABAR* analyses, including this one, fall into two categories, kinematic and topological, which are described below.

These variables can be used in one of two ways:

- ◇ If the distribution of a variable lies in a certain range for signal events and in a different range for background events then one can apply a "cut" to the distribution. The cut should be applied at a particular value such that events greater (or less) than the value, which are rejected, are mostly background events and consequently the remainder have an increased signal to background ratio.

- ◇ If the distributions of a variable for signal and background have different shapes then the approach of fitting can be applied. This approach can be applied even

when the previous consideration of favoured range is not met. The method of maximum likelihood fitting is described in detail in Section 3.6.

3.5.1 Kinematic Variables

The reconstructed mass of the candidate B meson

$$m_B = \sqrt{E_B^2 - \vec{p}_B^2} \tag{3.3}$$

is an obvious discriminating variable since for correctly reconstructed candidates this should be distributed around the actual B mass, 5.279 GeV. However, since B candidates are generally reconstructed from many tracks and/or neutral clusters they suffer from the detector resolution on each of these and the distribution becomes very wide ($\sim$ 25 MeV). Operating at the $\Upsilon(4S)$ energy, the four momenta of the B mesons are actually very well constrained by the beam energy, which is in turn very well measured in comparison with the detector energy resolution. As such it becomes possible to construct two, mostly uncorrelated, variables that are much better constrained [48, 49]. These are the difference between the reconstructed and expected B meson energy (ΔE) and the beam-energy substituted mass ($m_{\rm ES}$), which are given by

$$\Delta E = E_B - E_X \tag{3.4}$$

$$m_{\rm ES} = \sqrt{E_X^2 - \vec{p}_B^2} \tag{3.5}$$

where $(E_B, \vec{p}_B)$ is the four momentum of the reconstructed B meson and E_X is the beam-energy constrained derived energy for the B defined by

$$E_X = \frac{E_{\rm beam}^2 - \vec{p}_{\rm beam}^2 + 2\vec{p}_{\rm beam} \cdot \vec{p}_B}{2E_{\rm beam}} \tag{3.6}$$

where $(E_{\rm beam}, \vec{p}_{\rm beam})$ is the four momentum of the beams. All of these quantities are defined in the laboratory frame. Since $m_{\rm ES}$ is calculated only from the beam four-momentum and the momentum of the B candidate it is independent of the mass hypothesis of the B daughter tracks. ΔE, however, does depend on the mass

hypothesis since it uses the reconstructed energy of the B candidate. For well reconstructed B mesons $m_{\rm ES}$ should peak at the B mass, 5.279 GeV, and ΔE should peak at zero. For the decay mode $B^+ \to K^+\pi^-\pi^+$ the typical resolutions on these quantities are around 2.6 MeV and 19 MeV respectively.

3.5.2 Topological Variables

The topology of events is another way in which it is possible to distinguish between signal and background in the analysis of rare decays. Since the mass difference between the $B\overline{B}$ pair and the $\Upsilon(4S)$ is very small the $B\overline{B}$ pair is produced almost at rest in the CM frame, resulting in an isotropic distribution of their decay products. In continuum events, on the other hand, the mesons are produced with large kinetic energy and the decay products form highly collimated jets around the axes of the original quark and anti-quark. There are several variables that can be used to distinguish between these different behaviours. For the purposes of constructing some of these variables it is necessary to divide the final state particles into those that form the reconstructed B candidate and those that make up the "rest of the event" (ROE). All of these variables are calculated in the CM frame.

3.5.2.1 Thrust

The first topological variable is the cosine of the angle between the thrust axis of the reconstructed B candidate and the thrust axis of the ROE ($\cos\theta_T$). The thrust axis of a collection of particles is the axis along which the total longitudinal momentum is maximised. The absolute value ($|\cos\theta_T|$) peaks at 1 for jet-like events while the distribution for B events is almost uniform, as illustrated in Figure 3.1.

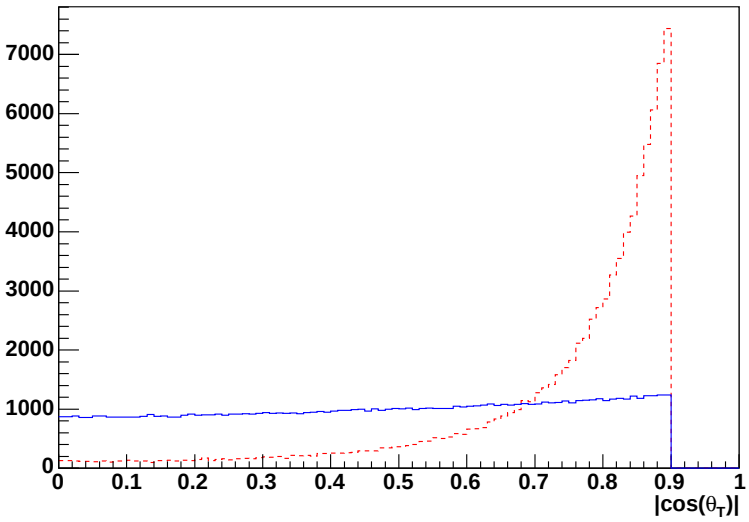

Figure 3.1: *Distribution of the topological variable* $|\cos\theta_T|$ *for* $B^+ \to K^+\pi^-\pi^+$ *non resonant MC (blue/solid line) and off-peak data (red/dashed line). The samples have been normalised to the same number of events. The cut off at 0.9 is applied in the pre-selection (Section 4.3.2).*

3.5.2.2 Energy/Momentum Flow

A further discriminating set of variables are those that describe the momentum or energy flow of the ROE. There are two such sets of variables commonly used in *BABAR* analyses.

The first set are dubbed the "CLEO Cones" [50]. To construct these, a 90° cone around the thrust axis of the reconstructed B is defined and split into 9 independent concentric 10° cones. The energy flow of all charged tracks and neutral candidates in the ROE into these cones (in both forward and backward hemispheres) is summed. The distributions of these cones are shown in Figure 3.2.

The second set of variables are based on the zero and second order Legendre polynomials and are defined as

$$L_0 = \sum_i^{\mathrm{ROE}} p_i \tag{3.7}$$

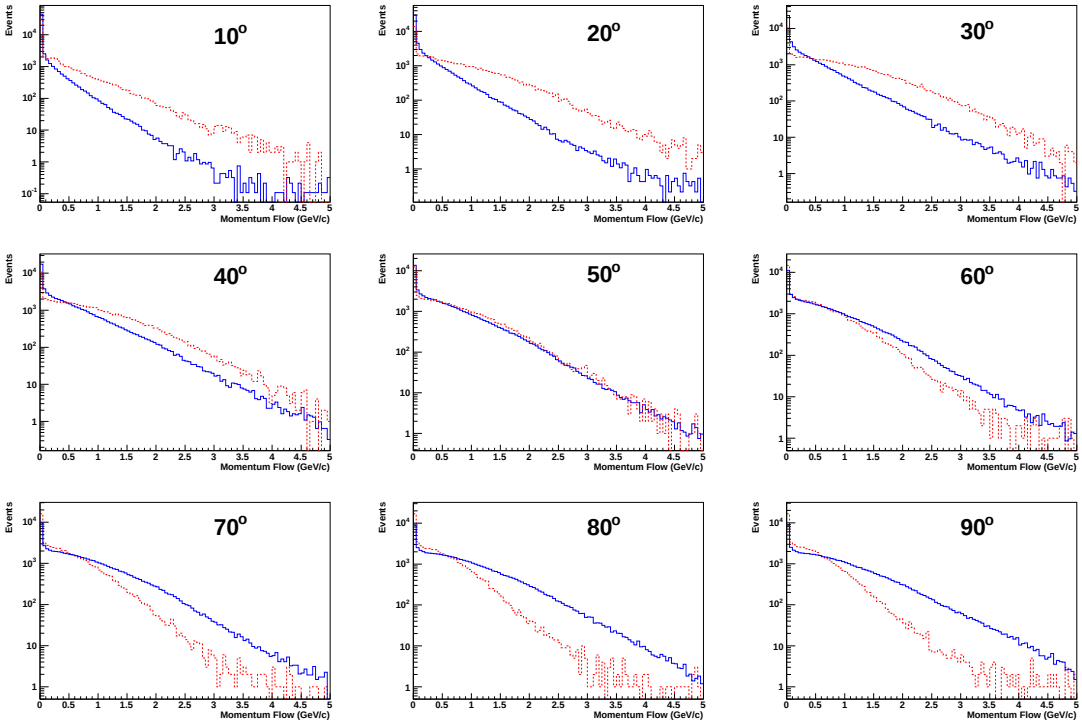

Figure 3.2: *The distribution of the CLEO Cones for $B^+ \to K^+\pi^-\pi^+$ non resonant MC (blue, solid) and off-peak data (red, dashed). The y-axis scale is logarithmic.*

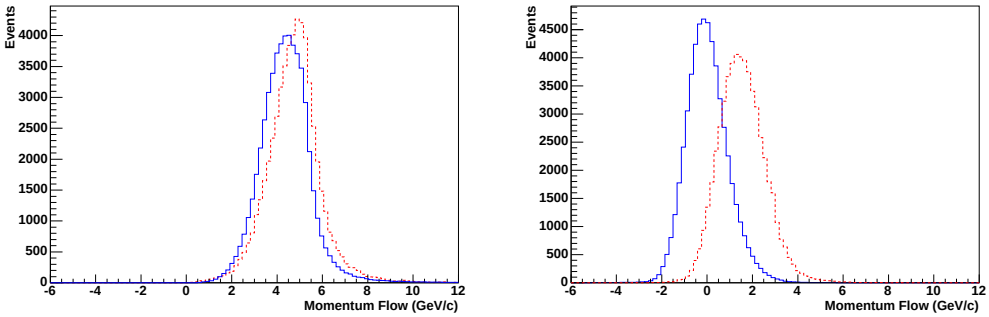

Figure 3.3: *The distribution of the L_0 and L_2 variables for $B^+ \to K^+\pi^-\pi^+$ non resonant MC (blue, solid) and off-peak data (red, dashed).*

$$L_2 = \sum_i^{\text{ROE}} p_i \times \frac{1}{2}(3\cos^2(\theta_i) - 1) \tag{3.8}$$

where p_i and θ_i are the momentum and polar angle of each track and neutral cluster in the ROE. The distributions of these variables are shown in Figure 3.3.

Individually these variables do not provide a large amount of discrimination but using a Fisher discriminant (Section 3.5.3) or Neural Net [51] to combine them yields a powerfully separating variable.

3.5.2.3 Conservation of Angular Momentum

A final pair of variables can be found by considering conservation of angular momentum. The first of these is $\cos\theta_{Bmom}$ the angle between the momentum of the reconstructed B candidate and the z-axis. For true B events, the angular distribution of the decay of the spin one $\Upsilon(4S)$ to two spin zero B mesons is proportional to $\sin^2(\theta_{Bmom})$, while for $q\overline{q}$ events the distribution is approximately uniform. The second variable is $\cos\theta_{Bthr}$ the angle between the thrust axis of the reconstructed B candidate and the z-axis. For true B events the distribution should be uniform due to the spherical nature of B decays, while for $q\overline{q}$ events it will show a distribution proportional to $1 + \cos\theta_{Bthr}$. The distributions of these variables are shown in Figure 3.4 for $B^+ \to K^+\pi^-\pi^+$ non resonant MC and off-peak data. The distri-

butions differ somewhat from the descriptions above due to acceptance effects from the detector and selection requirements.

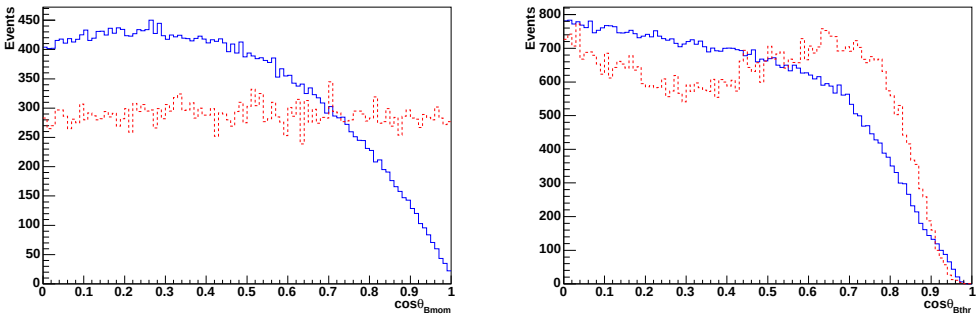

Figure 3.4: *The distribution of* $\cos(\theta_{Bmom})$ *and* $\cos(\theta_{Bthr})$ *for* $B^+ \to K^+\pi^-\pi^+$ *non resonant MC (blue, solid) and off-peak data (red, dashed).*

Again, these variables do not provide a large amount of discrimination when considered individually but they add further power to the momentum flow variables when combined with them in a Fisher discriminant.

3.5.3 Fisher Discriminant

As mentioned in the descriptions of the momentum flow and angular momentum variables, they are not particularly powerful on their own. It is therefore necessary to use some method to combine several variables into one more powerful variable. There are several such methods available, including Neural Nets [51], but we choose to use the method of the Fisher discriminant [52].

The Fisher discriminant is a linear discriminant and can be defined as:

$$\mathcal{F} = \sum_i a_i x_i = \vec{a}^T \vec{x}, \tag{3.9}$$

where x_i are some discriminating variables and a_i are coefficients chosen to maximise the separation of the signal and background distributions. In order to perform this

maximisation it is necessary to first define what is meant by the separation of the distributions:

$$D = \frac{(\bar{\mathcal{F}}_S - \bar{\mathcal{F}}_B)^2}{\sigma_S^2 + \sigma_B^2} \tag{3.10}$$

where $\bar{\mathcal{F}}_{S/B}$ and $\sigma^2_{S/B}$ are the mean and variance of the Fisher variable for either signal or continuum background.

The mean and variance of the Fisher variable can be written in terms of the means, $\vec{\mu}_{S/B}$, and covariance matrices, $E_{S/B}$, of the distributions of the discriminating variables, $\vec{x}$, by:

$$\bar{\mathcal{F}}_{S/B} = \vec{a}^T \vec{\mu}_{S/B}, \tag{3.11}$$

$$\sigma^2_{S/B} = \vec{a}^T E_{S/B} \vec{a}. \tag{3.12}$$

Writing $\vec{d} = \vec{\mu}_S - \vec{\mu}_B$ and $W = E_S + E_B$ then

$$D = \frac{\vec{a}^T \vec{d} \vec{d}^T \vec{a}}{\vec{a}^T W \vec{a}} \tag{3.13}$$

and setting the derivatives of D with respect to each a_i to zero gives

$$\vec{a} = W^{-1} \vec{d}. \tag{3.14}$$

Therefore by determining the means and variances of the variables' distributions and solving the above linear matrix equation, the coefficients can be determined.

Studies [53] have shown that combining L_0, L_2, $|\cos\theta_{Bmom}|$ and $|\cos\theta_{Bthr}|$ in a discriminant gives excellent discrimination power between signal and continuum background events. It is also seen in these studies that the difference between using a linear discriminant, such as a Fisher, and using a non-linear approach, such as a neural net, is minimal. Another study [54] has shown that adding the variable `TFlv` can further improve the separation power. `TFlv` is the output of the tagging algorithm. It can provide separation because in general the tagging algorithm will not be able to make a good determination of the flavour for continuum events since the decay is not a B decay and therefore does not contain the processes that the algorithm has been designed to look for. For B events there will be many that have

strong tags and a smaller proportion will have failed to be tagged. The distribution of |TFlv| is shown in Figure 3.5. A value towards 0 indicates that a tag could not be determined while a value of 1 indicates that a good tag was found.

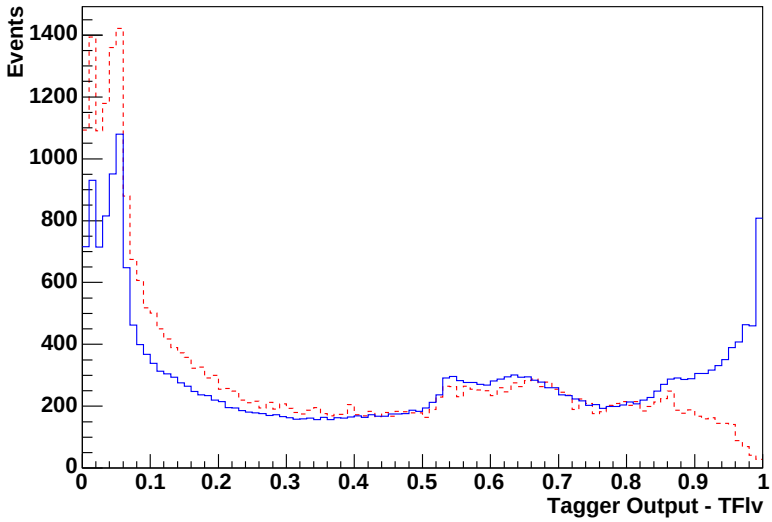

Figure 3.5: *The distribution of* |TFlv| *for* $B^+ \to K^+\pi^-\pi^+$ *non resonant MC (blue, solid) and off-peak data (red, dashed).*

A study was performed to determine if the five variables L_0, L_2, $|\cos\theta_{Bmom}|$, $|\cos\theta_{Bthr}|$ and |TFlv| give better discrimination than various other sets of variables used in previous analyses. The Fisher coefficients were calculated using a sample of off-peak data and $K^+\pi^-\pi^+$ non resonant Monte Carlo. Then using a second sample of each of these data types the relative discrimination of each of the Fisher types was tested. The chosen five variables were seen to be superior since for a given signal efficiency they provide a greater level of background rejection. The distributions of the Fisher discriminant for $B^+ \to K^+\pi^-\pi^+$ non resonant MC and off-peak data are shown in Figure 3.6.

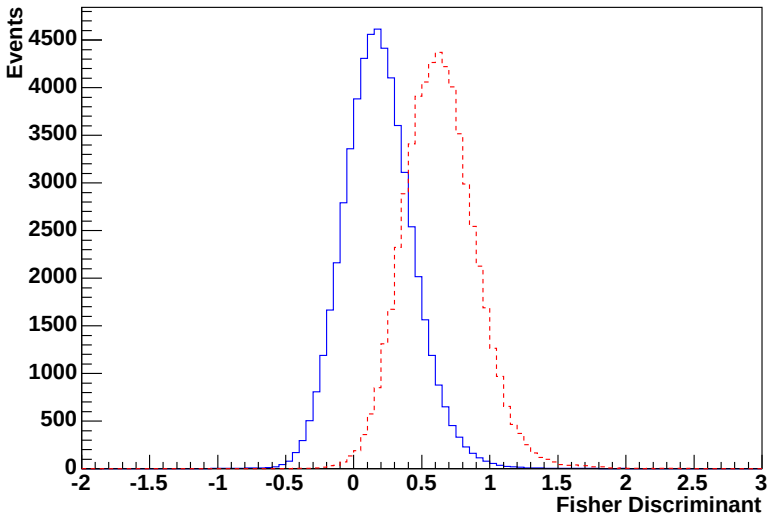

Figure 3.6: *Distribution of the Fisher discriminant for $B^+ \to K^+\pi^-\pi^+$ non resonant MC (blue/solid line) and off-peak data (red/dashed line). The samples have been normalised to the same number of events.*

3.6 Maximum Likelihood Fitting

The method of maximum likelihood fitting is a very powerful statistical method for determining a number of parameters from a given data set. It has many advantages over other methods such as χ^2 fitting, the most important of which is that it treats each event individually and so there is no need to bin the data. This eliminates the need to choose bin sizes, which can lead to bias and inaccuracy. A detailed description of the method can be found in [55].

If the distribution of a given variable x has a particular shape, such as a Gaussian distribution, then it is possible to express this as a normalised Probability Density Function (PDF) with parameters $\vec{\alpha}$, $P(x, \vec{\alpha})$. If N measurements are made of the variable x then the following likelihood function can be constructed, which will be a maximum when the parameters best describe the data

$$\mathcal{L}(\vec{\alpha}) = \prod_{i=1}^{N} P(x_i, \vec{\alpha}) \tag{3.15}$$

This can be generalised to the situation where P is a combination (by product or addition) of a number of normalised PDFs, each a function of one or more variables. For example, consider the situation of a fit being performed to three uncorrelated variables (x, y and z) where there are M different hypotheses for the events, *e.g.* signal and background. So P becomes

$$P(x, y, z, \vec{\alpha}) = \sum_{j=1}^{M} Q_j(x)\, R_j(y)\, S_j(z) \tag{3.16}$$

and the likelihood equation becomes

$$\mathcal{L}(\vec{\alpha}) = \prod_{i=1}^{N} \left(\sum_{j=1}^{M} Q_j(x_i)\, R_j(y_i)\, S_j(z_i) \right) \tag{3.17}$$

In practice the functional forms of the PDFs are fixed and many of the parameters are fixed to values determined from fitting the individual PDF to a MC or data control sample. It is also computationally more convenient to minimise the negative

log-likelihood rather than maximising the likelihood since the product over the N measurements in Eq. (3.15) becomes a summation

$$-l = -\log \mathcal{L} = -\sum_{i=1}^{N} \log P(\vec{x}_i, \vec{\alpha}) \tag{3.18}$$

3.6.1 Error Calculation

The error on a parameter can be calculated in two different ways during the fitting procedure. The first involves calculating the covariance matrix of the fit parameters, which is given by

$$H_{ij} = \frac{\partial^2 l}{\partial \alpha_i \, \partial \alpha_j} \tag{3.19}$$

and then inverting it to give the error matrix, $E = H^{-1}$. The vector of errors is then given by

$$\vec{\sigma_\alpha} = E\vec{\alpha} = H^{-1}\vec{\alpha} \tag{3.20}$$

The second method uses the Taylor expansion of l about its maximum $l_{\max}$

$$l = l_{\max} + l'(\delta\alpha_i) + \frac{l''(\delta\alpha_i^2)}{2!} + \cdots \tag{3.21}$$

In the region of $l_{\max}$ the first derivative must be zero and so neglecting higher terms by assuming that the second derivative is constant it is seen that the log-likelihood is parabolic in terms of its parameters close to its maximum. In turn this means that the likelihood $\mathcal{L}$ is Gaussian in the region of its maximum and that consequently the error on a parameter (σ_{α_i}) is given by

$$l(\alpha_i \pm \sigma_{\alpha_i}) = l_{\max} - \tfrac{1}{2} \tag{3.22}$$

3.6.2 Extended Maximum Likelihood Fitting

The above descriptions all take the normalisation of the PDFs to be unity. In fact it is often the case that the normalisation depends on an event yield, which is

distributed according to a Poisson distribution with mean ν. In these circumstances it is better to use the *extended* likelihood function

$$\mathcal{L}(\nu, \vec{\alpha}) = \frac{\nu^N e^{-\nu}}{N!} \prod_{i=1}^{N} P(\vec{x}_i, \vec{\alpha}) \tag{3.23}$$

$$= \frac{e^{-\nu}}{N!} \prod_{i=1}^{N} \nu\, P(\vec{x}_i, \vec{\alpha}) \tag{3.24}$$

In the case illustrated in Eq. (3.17), omitting constant factors, this becomes

$$\mathcal{L}(\vec{\alpha}, \vec{n}) = \exp\left(-\sum_{k=1}^{M} n_k\right) \prod_{i=1}^{N} \left(\sum_{j=1}^{M} n_j P_j(\vec{\alpha}, \vec{x_i})\right) \tag{3.25}$$

where the n_j are the number of events in hypothesis j.

3.6.3 Fitting Packages

Maximum likelihood fitting is a very widely used technique and as such dedicated packages have been developed for performing such fits. `Minuit` [56, 57] is an example of such package, which is capable of minimising a user-defined function and returning the values of its parameters and their errors at the minimum value. It has several routines: MIGRAD is the most commonly used minimisation routine, which finds the function minimum and makes a first attempt at calculating parameter errors; HESSE makes more precise calculations of parameter errors using the matrix inversion technique of Eq. (3.20); MINOS makes even more precise calculations of the errors, including any possible asymmetric errors using an iterative process based on Eq. (3.22).

`RooFit` [58] is a package developed within *BABAR*, which provides an interface to `Minuit` via `Root` [59], and also uses `Root` for histogram plotting and data manipulation. The normalisation of the likelihood function is automatically performed within the `RooFit` framework, either analytically (if possible) or numerically, before the function is passed to `Minuit`. A large number of possible PDF shapes are included in the `RooFit` package. These can be combined by addition, multiplication or convolution as well as being extended by the technique in Section 3.6.2.

`CharmlessFitter` is a package that simplifies the interface to `RooFit` for implementing certain common fitting tasks. It also has classes for performing event selection and calculation of Fisher coefficients.

`Laura++` [60] is a package for performing the Dalitz amplitude fit and as such contains definitions of the likelihood functions particular to such analyses. The resonance forms described in Section 1.3 are included as classes and there are further classes for describing the effects of background and acceptance. These models will be discussed in more detail in Section 4.7.

3.6.3.1 Toy Monte Carlo and Pull Distributions

As well as using the PDFs for fitting the `RooFit` and `Laura++` packages can also use them for generating "toy" Monte Carlo events. This is a very useful technique, that allows a particular fit to be tested for any biases that may exist in the likelihood function.

Toy MC events are often generated using the Von Neumann accept/reject algorithm [61]. Firstly, random numbers are thrown to determine where in the N-dimensional space the event is to be generated. The probability that the event will be accepted at this point in the variable space, $\vec{x}$, is given by:

$$P_{\text{accept}}(\vec{x}) = \frac{\mathcal{L}(\vec{x})}{\mathcal{L}_{\text{max}}} \tag{3.26}$$

where $\mathcal{L}(\vec{x})$ is the value of the likelihood function at that position and $\mathcal{L}_{\text{max}}$ is the maximum value of the likelihood in the variable space. A final random number is thrown and if this is less than P_{accept} then the event is accepted, otherwise it is rejected. This process is continued until the requested number of events have been accepted. In the limit of infinite statistics the events would be perfectly modelled by the PDFs. However, with a poorly constructed likelihood function or simply because of very low statistics biases may be present that have to be removed or accounted for.

To test for fit biases a number of toy MC events can be generated and then fitted, the same PDF being used at both stages. This experiment is repeated a large number of times, say 500 or 1000, and the fitted values of any free parameters are recorded. If the PDF is extended then the number of events generated for each hypothesis for each experiment is varied according to a Poisson distribution. The residual of the fitted value and the truth value is then constructed

$$\text{residual} = \alpha_{gen} - \alpha_{fit} \tag{3.27}$$

where α_{gen} is the mean of the Poisson distribution if the parameter is a yield. This residual is then divided by the error returned by the fit to give the "pull"

$$\text{pull} = \frac{\text{residual}}{\sigma_{\alpha_{fit}}} \tag{3.28}$$

A well constructed likelihood function, with no biases should give a pull distribution which is a Gaussian centred on zero and with unit width.

4

Analysis Method

4.1 Introduction

The next three chapters describe the amplitude analysis of the decay $B^+ \to K^+\pi^-\pi^+$ at the *BABAR* experiment. This chapter will describe the method of the analysis that has been performed for this thesis. The method will be presented in an overview before being fully described, including how the techniques and tools outlined in Chapter 3 are employed to their best effect. The analysis results are presented in Chapter 5 and their implications are discussed with reference to theoretical predictions and results from other experiments in Chapter 6.

4.2 Overview

This analysis is the first full Dalitz plot analysis of the mode $B^+ \to K^+\pi^-\pi^+$ at the *BABAR* experiment. A previous quasi-two-body analysis of the mode was carried out, by the author and three others, using a data set corresponding to an integrated luminosity of $56\,\text{fb}^{-1}$ [1, 62]. This analysis uses an on-peak data sample of 231.8 million $B\overline{B}$ pairs, which corresponds to an integrated luminosity of $210.6\,\text{fb}^{-1}$, along with $21.6\,\text{fb}^{-1}$ of off-peak data, which is used for background characterisation. The whole of the Dalitz plot will be considered, and a maximum likelihood technique will be used to extract the relative magnitudes and phases of the contributing resonant and non resonant components. The signal model for the analysis was established containing the following modes:

- $B^+ \to K^{*0}(892)\pi^+$, $K^{*0} \to K^+\pi^-$
- $B^+ \to K_0^{*0}(1430)\pi^+$, $K_0^{*0}(1430) \to K^+\pi^-$
- $B^+ \to \rho^0(770)K^+$, $\rho^0(770) \to \pi^+\pi^-$
- $B^+ \to f_0(980)K^+$, $f_0(980) \to \pi^+\pi^-$
- $B^+ \to \chi_{c0}K^+$, $\chi_{c0} \to \pi^+\pi^-$
- $B^+ \to K^+\pi^-\pi^+$ non resonant

Other intermediate resonances are also considered in extended models, but are not included in the nominal signal model.

Events are selected using a number of kinematic and event shape variables, as well as particle ID selectors, which have all been described in Chapter 3. In particular kaon candidates are required to pass the SMSKaonSelector in tight mode and two oppositely charged pion candidates are required to fail the SMSKaonSelector in tight mode. Vetoes that attempt to remove any events with a J/ψ, $\psi(2S)$, or $\overline{D}^0$ candidate are also implemented at this stage.

Backgrounds are divided into a number of categories that are evaluated and incorporated within the analysis in the following manners:

- ◇ Continuum $q\overline{q}$ Background: Background events from light quark production have a very different topology to those arising from a B-meson decay, and event shape variable cuts are effective at removing a large proportion of these events. The remaining events are incorporated in the fit by means of a 2-D histogram of their distribution in the Dalitz plot.

- ◇ $B\overline{B}$ Background: These are events that contain a $B\overline{B}$ pair but neither decay to the final state $K^+\pi^-\pi^+$. However, during the reconstruction process three tracks are still found that successfully fake the $K^+\pi^-\pi^+$ final state. Potential contributing modes are identified by studying generic $B\overline{B}$ Monte Carlo simulations (MC). The expected number of events and their distribution in the Dalitz plot is determined from exclusive MC samples for each identified mode. The individual contributions are combined into a 2-D histogram, which is then used in the Dalitz plot fit.

- ◇ Self Cross Feed (SCF): These are misreconstructed signal events, where one or more of the reconstructed particles truly originates from the second B-decay in the event or where a double particle mis-ID has occurred. The fraction of self cross feed in the signal is determined from $B^+ \to K^+\pi^-\pi^+$ non resonant MC events. It is found to be of negligible size ($< 2\%$) and as such is not accounted for in the fit.

The final selected events form a signal strip in the ΔE–$m_{\rm ES}$ plane. A fit to $m_{\rm ES}$ is performed to extract the fraction of $q\overline{q}$ events. This fit contains PDFs for signal, $q\overline{q}$ events and $B\overline{B}$ background events. The signal PDF is obtained from truth-matched $B^+ \to K^+\pi^-\pi^+$ non resonant MC events, the $q\overline{q}$ PDF is obtained from off-peak data and the $B\overline{B}$ background PDF is obtained from combining exclusive MC samples. The $m_{\rm ES}$ fit is performed using the `CharmlessFitter` package.

A further $m_{\rm ES}$ cut is then applied to select a signal box. The events in the signal box are used in the Dalitz plot amplitude fit, which uses the `Laura++` package. The free parameters of the amplitude fit are the magnitudes and phases of each of the signal components. Due to the highly complex nature of the likelihood function there are many local minima in the parameter space and as such the fit result has a large dependence on its initial values. Therefore the amplitude fit is repeated using many different initial values for the fit parameters and the results from the fit(s) with the best likelihood are selected. The legitimacy of this process is tested with toy MC studies. Fits are also carried out for different experimental hypotheses, including omission and addition of signal components.

Systematic errors due to uncertainties on the shape of the background distributions in the Dalitz plot, the normalisation of each of the backgrounds, the variation of the signal efficiency over the Dalitz plot and uncertainties on some of the resonance masses, widths and other parameters are investigated and evaluated.

4.3 Event Selection

The selection of events for this analysis is broadly divided into three parts. The first procedure reads events from the event store, which is written at the end of the OPR process (Section 3.2), and "skims" them for events that could contain a B decay to three charged tracks. The events that pass the skim are written back to the event store. The second procedure reads the skimmed events and places more demanding criteria on them as well as calculating various quantities that can be used in further analysis, such as the event shape variables described in Section 3.5.2. The final stage selects out the $K^+\pi^-\pi^+$ final state and imposes very tight requirements on the events.

4.3.1 Event Preselection

The data are read from the event store and passed through a filter algorithm which selects inclusively B decays to final states with three "stable" charged particles. The algorithm forms all distinct combinations of three tracks from the `GoodTracksLoose` list as defined in Section 3.2.1. For each reconstructed B candidate, the following requirements are made:

- ◇ The total charge of the B candidate is required to be ± 1.
- ◇ The total number of tracks in the event is required to be ≥ 4. This ensures that there is at least one track from the other B in the event, which can help with subsequent analysis.
- ◇ The total energy of the event is required to be $< 20\,\mathrm{GeV}$. This is a basic sanity check, and removes fewer than 1% of events.
- ◇ The beam-energy substituted mass m_{ES}, defined in Section 3.5.1, is required to be within $0.1\,\mathrm{GeV}/c^2$ of $\frac{\sqrt{s}}{2}$ $(5.29\,\mathrm{GeV}/c^2)$.
- ◇ The variable denoted ΔE, also defined in Section 3.5.1, is required to have an absolute value less than $0.45\,\mathrm{GeV}$. This constraint is tested for all final-state track mass assignments, and the event is selected if any such candidate passes this requirement.

The skim algorithm is defined by the *BABAR* Charmless Three Body working group and the skims are run centrally within the collaboration.

4.3.2 Batch Level Pre-Analysis

The output from the skims is further refined and the data placed into `Root` [59] ntuples using the `NonCharm3BodyUser` package [63], which is based on the common *BABAR* framework. During this stage the following selection criteria are applied:

- ◇ Vertexing of B candidates, after which $m_{\rm ES}$ and ΔE are recalculated.
- ◇ Vertexing then re-performed with mass constraint applied to the fitted B candidate (all combinations of π and K track hypotheses are considered in these fits).
- ◇ Particle ID selectors are run.
- ◇ Event shape variables are calculated.
- ◇ Calculation of Dalitz plot quantities such as invariant mass and cosine of the helicity angle
- ◇ ΔE is required to have an absolute value less that 0.35 GeV. The constraint is tested for all final-state track assignments and the event is selected if any such candidate passes this requirement.
- ◇ The magnitude of $\cos\theta_T$ (Section 3.5.2.1) must be < 0.9.

At this stage the resulting ntuples are entirely general to any three-charged-track mode.

4.3.3 Final Selection for $B^+ \to K^+\pi^-\pi^+$

After the skims and ntuple stages have been run a further selection is performed on the charge track combinations to single out the $K^+\pi^-\pi^+$ final state and further suppress backgrounds. This final selection takes as its input the `Root` files from the pre-analysis just described and writes reduced `Root` files as its output, which contain a smaller number of variables as well as fewer events. The code to perform this selection is based on the `CharmlessFitter` package. The selections applied in this $B^+ \to K^+\pi^-\pi^+$ analysis are:

- ◇ Candidate must have a successful kinematic fit for a $K^\pm\pi^\mp\pi^\pm$ track hypothesis.

- ◇ Kaon candidate track must pass the SMSKaonSelector in tight mode.
- ◇ Pion candidate tracks must fail the SMSKaonSelector in tight mode.
- ◇ All tracks must fail the electron LHSelector.
- ◇ Pion candidate tracks must have opposite charges.
- ◇ The magnitude of the cosine of the angle between the thrust axis of the B candidate and the thrust axis of the rest of the event must be < 0.7
- ◇ The value of the Fisher discriminant must be < 0.21.
- ◇ The value of $m_{\rm ES}$ must be less than $\frac{\sqrt{s}}{2}$ ($5.29\,{\rm GeV}/c^2$).
- ◇ The value of ΔE must be between -0.0349 and 0.0551.
  These numbers derive from a selection of the magnitude of ΔE being less than $0.06\,{\rm GeV}$ (approx. 3σ of the signal distribution). However, the mean of the signal ΔE distribution in $B^+ \to \overline{D}^0\pi^+$ data is found to be shifted from zero by -4.9 MeV and so the selection window is shifted by the same amount. Finally, the lower edge of the window is tightened by 30 MeV in order to reduce the amount of $B\overline{B}$ background passing the selection.
- ◇ The requirement of a single candidate per event is then imposed. In the event of multiple candidates existing, which occurs in fewer than 3% of events, the single candidate is chosen randomly so as not to bias the $m_{\rm ES}$ and Dalitz plot distributions.
- ◇ Certain potential $B\overline{B}$ backgrounds are also vetoed at this stage:
  - $B^+ \to J/\psi\, K^+$, $J/\psi \to \mu^+\mu^-$ (or $J/\psi \to \pi^+\pi^-$)
    $2.97 < m_{\pi^+\pi^-} < 3.17\,{\rm GeV}$
  - $B^+ \to \psi(2S)K^+$, $\psi(2S) \to \mu^+\mu^-$ (or $\psi(2S) \to \pi^+\pi^-$)
    $3.56 < m_{\pi^+\pi^-} < 3.76\,{\rm GeV}$

– $B^+ \to \overline{D}^0\pi^+$, $\overline{D}^0 \to K^+\pi^-$
$1.80 < m_{K^+\pi^-} < 1.90\,\text{GeV}$ and $1.80 < m_{\pi^+\pi^-} < 1.90\,\text{GeV}$

A summary of the selection requirements and their efficiencies for $B^+ \to K^+\pi^-\pi^+$ non resonant MC are shown in Table 4.1.

4.3.4 Definition of Fitting Regions

A signal strip, sideband and signal box are defined in Table 4.1 and illustrated in Figure 4.1. The final average selection efficiency, for each of these regions, obtained from $B^+ \to K^+\pi^-\pi^+$ non resonant MC, plus the number of on-peak data events selected are given in Table 4.1.

The signal strip is used for performing a 1D fit to m_{ES} in order to determine the fraction of $q\overline{q}$ events in the signal box. This fit is described in detail in Section 4.6. The sideband is used to characterise the shape of the $q\overline{q}$ background in the Dalitz plot (Section 4.5.2). The signal box is then used for the amplitude fit as described in Section 4.7.

4.3.5 Selection Optimisation

Many of the selection requirements mentioned above are derived from previous analyses of the $B^+ \to K^+\pi^-\pi^+$ mode and were shown to be optimal in those analyses [64, 65]. However, the Fisher discriminant used in this analysis is new and as such had to be optimised. The event shape variables in the Fisher are highly correlated with $\cos\theta_T$ and as such the selections on these two variables must be optimised together in a combined procedure.

Various values of the $|\cos\theta_T|$ cut are tried and for each one the Fisher coefficients are recalculated using the method described in Section 3.5.3. For each of the $|\cos\theta_T|$ cuts various values of the Fisher cut are tried. The expected numbers of background

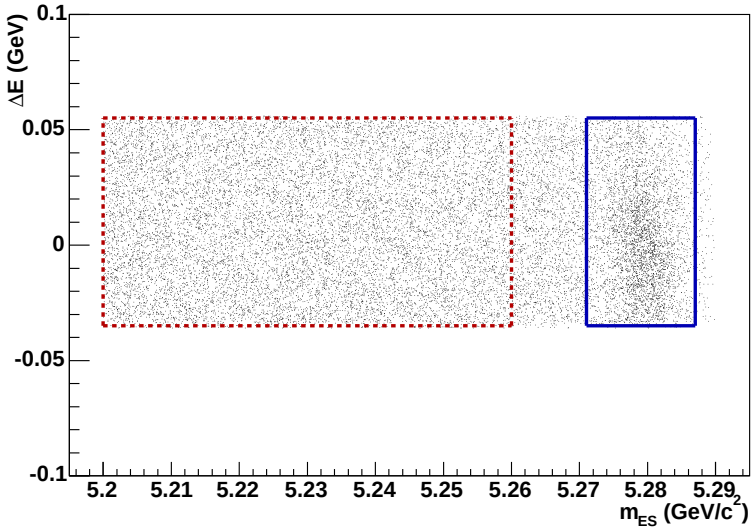

Figure 4.1: *ΔE–$m_{\rm ES}$ plane, showing signal strip, sideband and signal box. The area populated by events (these are on-resonance data events) is the signal strip, the sideband is defined by the dashed, red lines, and the signal box by the solid, blue lines.*

Table 4.1: *Summary of average selection efficiencies. The Monte Carlo study used 1.299 million signal events. The cut-by-cut efficiencies are calculated with respect to the previously applied cut. The total efficiencies are the total number of events passing the selection criteria divided by the total number of input/generated events. Also shown are the number of events selected from the on-peak data sample following each cut.*

Cut	Signal MC Selection Efficiency	No. of On-Peak Data Events
Reconstruction and preselection	0.698	16,119,010
Valid $K^+\pi^-\pi^+$ vertex fit hypothesis	0.980	11,529,700
Kaon PID requirements (SMSSelector)	0.746	2,885,729
Electron veto (LHSelector)	1.000	2,731,391
$q_{\pi_1} \times q_{\pi_2} = -1$	0.974	2,022,370
$\lvert\cos\theta_T\rvert < 0.7$	0.706	354,070
Fisher < 0.21	0.727	100,697
$5.20 < m_{\rm ES} < 5.29\,{\rm GeV}/c^2$	0.994	91,061
$-0.0349 < \Delta E < 0.0551\,{\rm GeV}$	0.813	36,002
Veto $\overline{D}^0$, J/ψ and $\psi(2S)$	0.831	21,660
Signal Strip:	0.17137 $\pm\ 3.6 \times 10^{-4}$	21,660
Signal Box: $5.271 < m_{\rm ES} < 5.287\,{\rm GeV}/c^2$	0.16664 $\pm\ 3.6 \times 10^{-4}$	4,704
Sideband: $5.20 < m_{\rm ES} < 5.26\,{\rm GeV}/c^2$	3.013×10^{-3} $\pm\ 4.8 \times 10^{-5}$	14,491

and signal events are calculated for each of the Fisher cuts and an estimator of signal significance $\frac{S}{\sqrt{S+B}}$ is calculated; where S and B are estimates of the number of signal and background events passing the cuts in the final data sample. The combination of cuts that maximises this estimator is chosen as the optimal set.

The expected number of signal events is calculated by assuming the current world average for the inclusive branching fraction for the decay $B^+ \to K^+\pi^-\pi^+$and using phase space signal MC to determine the efficiency of the cuts. These two quantities

are used in conjunction with the number of $B\overline{B}$ pairs, measured using the B-counting procedure outlined in Section 3.4, to calculate the number of expected signal events:

$$S = \epsilon \, N_{B\overline{B}} \, \mathcal{B} \tag{4.1}$$

The expected number of background events is calculated by looking at an on-peak data sideband which covers the same range of $m_{\rm ES}$ as the signal strip defined in Table 4.1 but is shifted in ΔE so that it contains no signal events ($0.1 < \Delta E < 0.3\,\text{GeV}$). This is designated the "upper sideband". The equivalent "lower sideband" ($-0.3 < \Delta E < -0.1\,\text{GeV}$) cannot be used since it is highly polluted by B-backgrounds. A fit is performed to the events in the upper sideband and the function that is fitted is integrated over the $m_{\rm ES}$ range of the sideband and signal box that are defined in Table 4.1 to form a ratio of these two regions. This ratio, $\mathcal{R}$, along with the number of events found in the sideband yields the expected number of background events in the signal box:

$$B = \mathcal{R} \, N_{\rm sideband} \tag{4.2}$$

This procedure results in several plots like Figure 4.2, which is the plot for the cut $|\cos\theta_T| < 0.7$ used in this analysis. It can be seen from this plot that the Fisher < 0.21 cut gives the maximum value of $\frac{S}{\sqrt{S+B}}$.

4.4 Efficiency, Self Cross Feed and Migration

Signal reconstruction efficiency is the fraction of signal events that pass the event reconstruction and selection criteria enumerated in Section 4.3. Table 4.1 gives the average reconstruction efficiency for $B^+ \to K^+\pi^-\pi^+$ events generated according to phase space. However, the reconstruction efficiency of signal events is a function of the angular and momentum distributions of the daughter particles in the detector and as such will vary across the Dalitz plot. This variation must be taken into

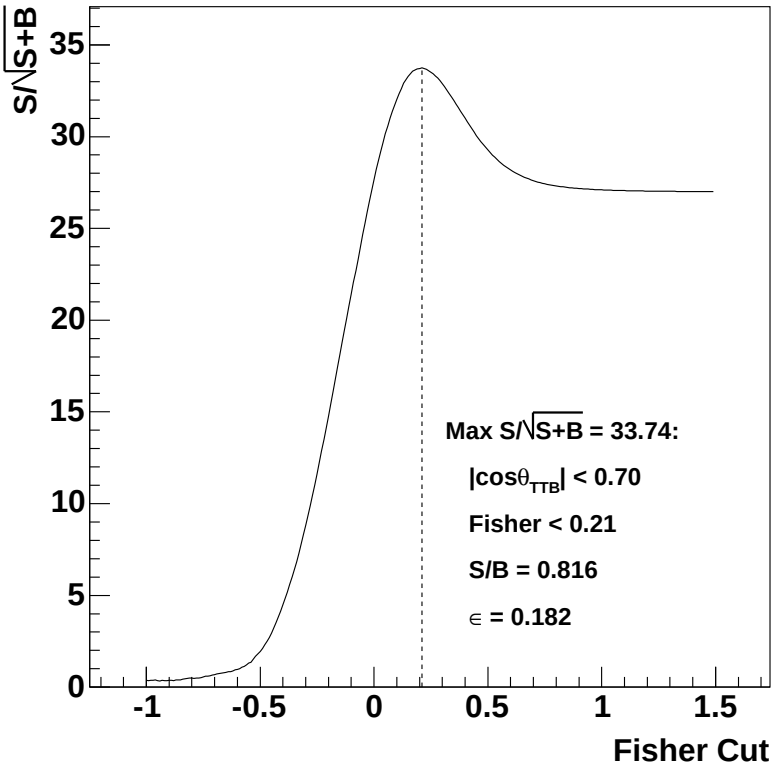

Figure 4.2: *Signal significance as a function of Fisher selection.*

account in the amplitude fit in order for the observed distribution of signal events to be correctly modelled.

4.4.1 Efficiency Variation across the Dalitz plot

In order to study the variation in efficiency for reconstructing signal events, a Monte Carlo sample, consisting of 1,299,000 $B^+ \to K^+\pi^-\pi^+$ non resonant events, was generated. These events were subjected to the analysis reconstruction and selection criteria summarised in Table 4.1, however, none of the charm vetoes were applied to the MC sample in order that the variation be modelled over the whole of the kinematically allowed area. This resulted in a reconstructed sample of 267,991 events in the signal box. A further constraint was then applied that the reconstructed event must be truth-matched, i.e. the three daughters must originate from the same B-meson and that they must be the only daughters of that B-meson. This reduced sample, of 258,945 events, was used to construct a 2-dimensional histogram showing the efficiency variation across the Dalitz plot. Firstly a denominator histogram is produced by binning the true distribution of the 1,299,000 MC events as determined from the MC truth information. Then a numerator histogram is produced by binning the reconstructed events, each weighted by the efficiency corrections due to tracking, which were described in Section 3.3.1. It is the quotient of these histograms that is used in the amplitude fit. An example plot is shown in Figure 4.3.

The efficiency is relatively flat across most of the Dalitz plot, but with some smooth decrease in the corners. There are some edge effects visible in Figure 4.3, which are due to the bins being intersected by the kinematic boundary. Such bins may have a very low content in both the numerator and denominator histograms, causing a large statistical error on that bin. To reduce any errors this may introduce these bins with a low number of events are merged with a neighbouring bin (for both truth and reconstructed events) and the efficiency for the double sized bin is calculated. The effect of these corrections can be seen in Figure 4.4. In the amplitude fit linear

interpolation will be applied to help smooth out any other statistical fluctuations. The choice of bin size for these histograms depends on the migration of events across the Dalitz plot (Section 4.4.3), and a desire to limit the number of bins with large statistical errors. It can also be seen from Figure 4.5 that the efficiency variation is the same for both B^+ and B^- events. As such, the histogram for the combined charges is used to boost the statistical precision.

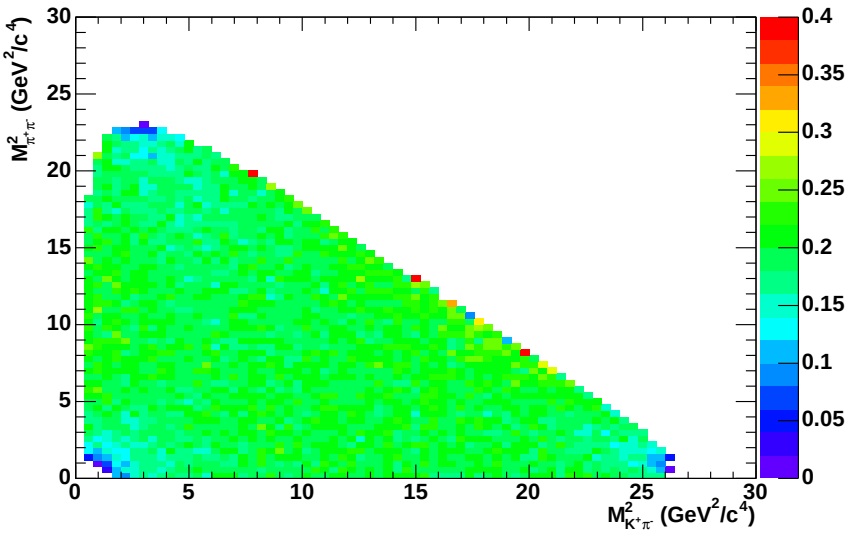

Figure 4.3: *Efficiency variation across the Dalitz plot.*

4.4.2 Self Cross Feed

Self cross feed (SCF) is where signal events have been misreconstructed by switching one or more particles from the decay of the signal B-meson with particles from the other B-meson in the event. The amount of self cross feed present in this decay mode is estimated from MC studies, using the same sample as used for determining the efficiency histograms. The MC events were subjected to the same reconstruction and selection criteria as for the efficiency study, but with the orthogonal constraint that the reconstructed event lacked a truth-match. Of the 1,299,000 $B^+ \to K^+\pi^-\pi^+$ non resonant MC events used, a total of 267,991 passed the reconstruction, of which

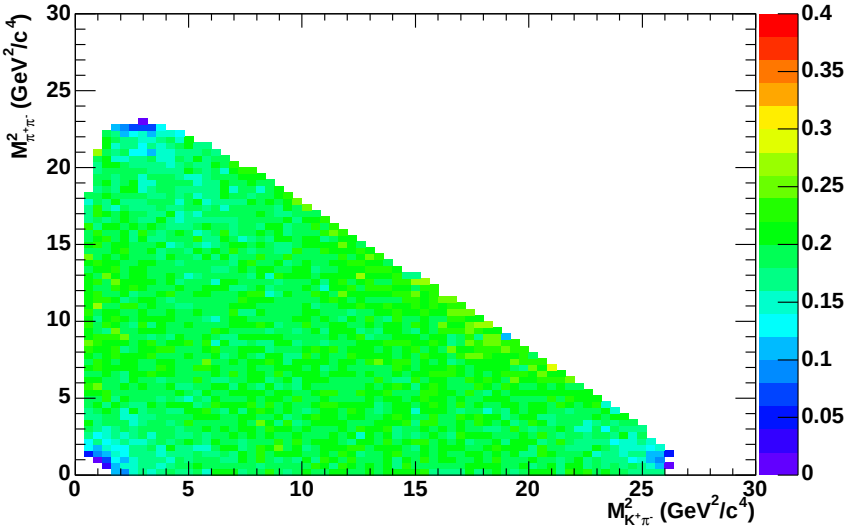

Figure 4.4: *Efficiency variation, corrected for low statistics bins.*

9046 lacked a truth-match and so are considered to be Self Cross Feed. This corresponds to SCF making up 3.4% of the signal in the Signal Strip. For the Signal Box SCF is 3401 events out of 260,924, which is a mere 1.3%. The SCF distribution in the Dalitz plot can be seen in Figure 4.6, which also shows the fraction of events that are SCF. From this is can be seen than even in the corners of the Dalitz plot SCF is not dominant and as such its effect will be neglected in this analysis. These assumptions have be tested using full MC fits, which are described in Section 5.4. Separate plots are also produced for B^+ and B^- decays, as shown in Figure 4.7.

4.4.3 Migration

The migration of events in the Dalitz plot is the difference between the true position of an event and the position where it is reconstructed. A large level of migration would mean that events could move in and out of resonance bands and interference regions in such a way as to blur the interference effects and resonance shapes. This would greatly limit the accuracy with which the various amplitude parameters could

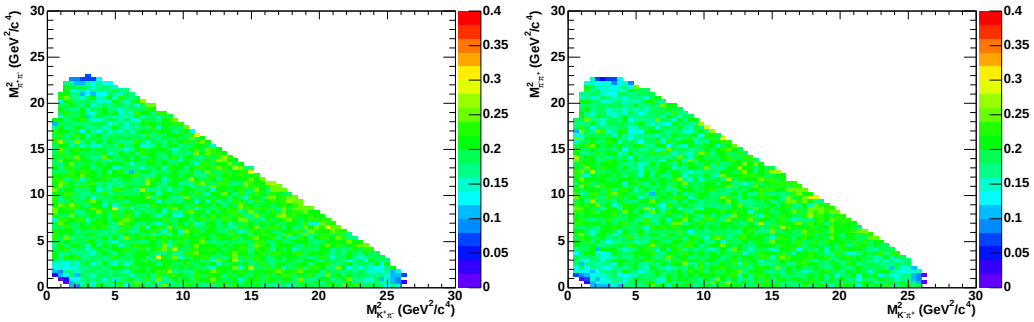

Figure 4.5: *Efficiency variation across the Dalitz plot; the left hand plot shows B^+ events, the right hand plot shows B^- events.*

be determined. This effect is also very important in determining the maximum "safe" binning for the efficiency histogram since the bins must be larger than the average size of the migration.

In order to study the migration, a sample of Monte Carlo events was generated, and the difference between the truth values and the reconstructed values was calculated. For a single event the migration distance was defined as:

$$d_{\text{migration}} = \sqrt{\left(m^2_{13\,\text{truth}} - m^2_{13\,\text{reco}}\right)^2 + \left(m^2_{23\,\text{truth}} - m^2_{23\,\text{reco}}\right)^2} \tag{4.3}$$

Each event was then plotted, one histogram weighted by the value of $d_{\text{migration}}$ and another histogram without the weight. The ratio of these two histograms gives a histogram that shows the average value of $d_{\text{migration}}$ over the Dalitz plot. Two different categories of this histogram were constructed:

- ◇ Outflow Histograms: Events are plotted at their MC truth co-ordinates, to show **from** where in the Dalitz plot events move.
- ◇ Inflow Histograms: Events are plotted at their reconstructed co-ordinates, to show **to** where in the Dalitz plot events move.

Inflow and outflow histograms for truth matched events are shown in Figure 4.8. For comparison, histograms for Self Cross Feed events are shown in Figure 4.9. It

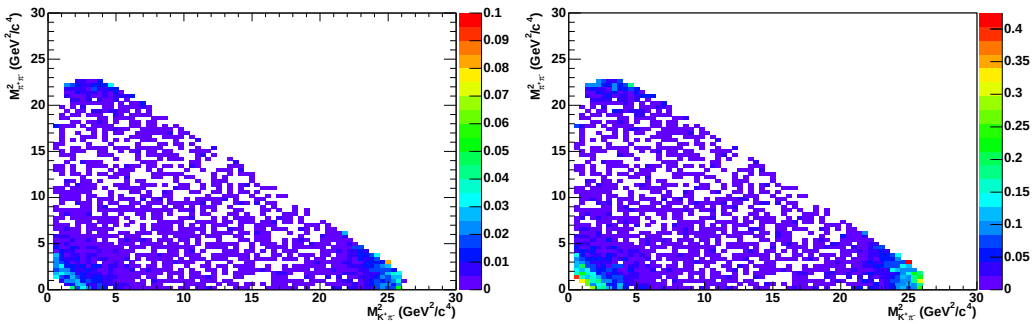

Figure 4.6: *Dalitz distribution of Self Cross Feed Events (left hand plot), and ratio of SCF to all events (right hand plot). The vertical scale on the left hand plot is the ratio of the number of SCF events in the bin to the number of generated events in the bin. In the right hand plot it is the ratio of the number of SCF events in the bin to the total number of reconstructed events in the bin, i.e. SCF plus truth-matched.*

can be seen from the truth matched histograms that the migration is at a very low level and furthermore that it is uniform across the Dalitz plot. As such its effect can be neglected from the amplitude fit.

4.5 Background Determination

Dalitz plot analyses of charmless B-meson decays have a very high proportion of background compared with, say, analyses of D-meson decays. As such, the accurate determination of the background fractions and distributions in the Dalitz plot is essential. This section describes the backgrounds present in this analysis and the techniques employed to first reduce and then model them.

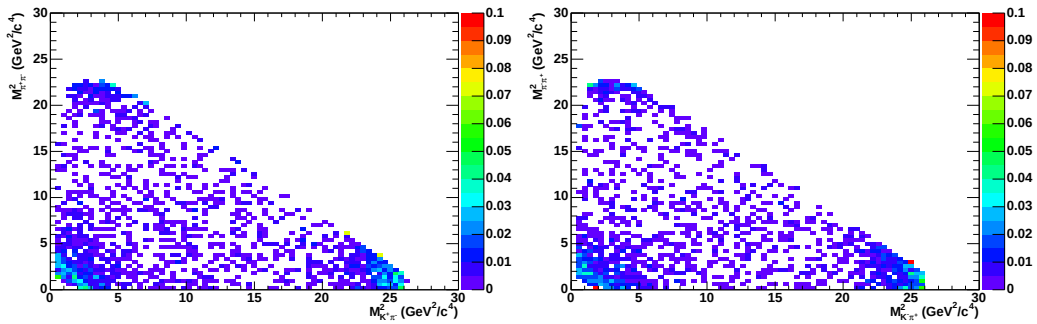

Figure 4.7: *Dalitz distribution of Self Cross Feed Events; the left hand plot shows B^+ events, the right hand plot shows B^- events.*

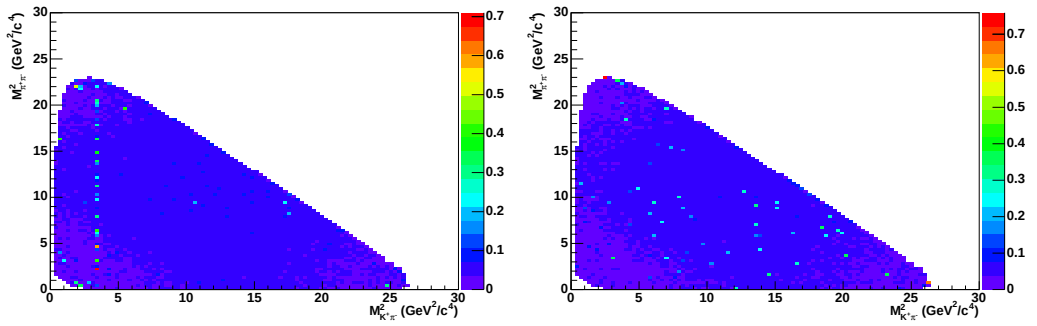

Figure 4.8: *Migration of truth matched events within the Dalitz plot; the left hand plot shows inflow, the right hand plot shows outflow.*

4.5.1 $B\overline{B}$ background

The first source of background in this analysis to be discussed is that from B-meson decays to modes other than our signal mode ($B^+ \to K^+\pi^-\pi^+$). To investigate these $B\overline{B}$ backgrounds we used MC truth information from a sample of 174 million generic B^+B^- decays and a sample of 148 million generic $B^0\overline{B}^0$ decays to identify the particular contributing modes. These modes fall into several categories:

- **Pure combinatorics:** where a $B\overline{B}$ event happens to have 3 unrelated tracks which are successfully reconstructed as signal. These events are very similar in nature to continuum background events in both their $m_{\rm ES}$ and Dalitz plot

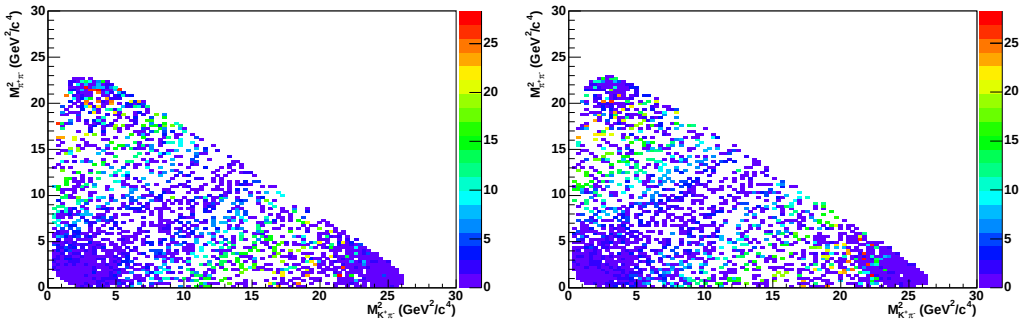

Figure 4.9: *Migration of self cross feed events within the Dalitz plot; the left hand plot shows inflow, the right hand plot shows outflow.*

distributions.

◇ **Signal combinatorics:** from mis-reconstructed signal events. This has been shown in Section 4.4.2 to be a very small effect and is consequently neglected in this analysis.

◇ **Particle misidentification:** which includes pion/kaon misidentification and that of a muon or electron as a pion. The feed through from $B^+ \to \pi^+\pi^-\pi^+$ is small due to the tight PID on the kaon, while that from $B^+ \to K^+K^-\pi^+$ is low due to the very small branching fraction for this mode [64]. However, both of these modes are considered explicitly as well as $B^+ \to K^+K^-K^+$. The largest potential contributors in this category are $B^+ \to J/\psi\, K^+$, $J/\psi \to \mu^+\mu^-$ and $B^+ \to \psi(2S)K^+$, $\psi(2S) \to \mu^+\mu^-$, however, the vetoes against these modes, enumerated in Section 4.3.3, are extremely effective at removing these backgrounds.

◇ **Specific $B \to D$ decays:** the comparatively high branching fraction of these decays make them a large contributor to our $B\overline{B}$ backgrounds. Most of these decays are wrongly reconstructed, with either a low momentum π^0 or γ being lost, a kaon being mis-identified as a pion or an electron or muon being mis-identified as a pion. All these effects lead to the ΔE distribution of these

modes being peaked towards negative values. Tightening the lower edge of the ΔE cut (Section 4.3.3) almost completely eliminates the lepton mis-ID modes and greatly reduces the efficiencies of the others.

- ◇ **2 and 4-body charmless decays:** such as $B^+ \to \eta' K^+$ with $\eta' \to \rho^0\gamma$, $\rho^0 \to \pi^+\pi^-$ where the γ is lost, and $B^0 \to K^+\pi^-$ where a pion from the other B in the event is incorrectly attributed to this decay.

The $B\overline{B}$ backgrounds that remain after the selection cuts must be modelled in the likelihood fit. Exclusive MC samples of these decays are used to quantify these backgrounds and obtain their $m_{\rm ES}$ and Dalitz plot distributions. All the modes examined are listed in Tables 4.2-4.5 along with their branching fractions, efficiencies and number of expected events. The $m_{\rm ES}$ distribution of the $B\overline{B}$ backgrounds can be seen in Figure 4.14. The Dalitz plot histogram from the signal box, which is used in the likelihood fit, can be seen in Figure 4.16. The number of $B\overline{B}$ events expected in both the signal box and sideband is determined using the reconstruction efficiencies measured from the MC samples and the current world average branching fractions for each of the modes, taken either from the Particle Data Group tables [2] or those of the Heavy Flavor Averaging Group [66].

Table 4.2: *Charm B^+B^- background modes, with branching fractions, efficiencies and number of expected events.*

Mode	BF	Signal Box Efficiency			Number of Expected Events in Signal Box		
	(10^{-6})	All	B^+	B^-	All	B^+	B^-
$B^+ \to \overline{D}^0 K^+$; $\overline{D}^0 \to K^+\pi^-$	14.1 ± 2.3	0.545 ± 0.012	0.2762 ± 0.0087	0.2691 ± 0.0086	17.8 ± 3.0	9.0 ± 1.5	8.8 ± 1.5
$B^+ \to \overline{D}^0 K^+$; $\overline{D}^0 \to K^+\pi^-\pi^0$	48.1 ± 8.3	0.0149 ± 0.0033	0.0060 ± 0.0021	0.0090 ± 0.0026	1.66 ± 0.47	0.66 ± 0.26	1.00 ± 0.34
$B^+ \to \overline{D}^0 \pi^+$; $\overline{D}^0 \to K^+K^-$	19.4 ± 1.3	0.530 ± 0.051	0.260 ± 0.036	0.270 ± 0.037	23.8 ± 2.8	11.7 ± 1.8	12.1 ± 1.9
$B^+ \to \overline{D}^0 \pi^+$; $\overline{D}^0 \to K^+\pi^-$	189.2 ± 11.9	0.238 ± 0.010	0.1259 ± 0.0076	0.1116 ± 0.0072	104.2 ± 8.1	55.2± 4.9	48.9± 4.4
$B^+ \to \overline{D}^0 \pi^+$; $\overline{D}^0 \to K^+\pi^-\pi^0$	647.4 ± 54.8	0.035 ± 0.0037	0.0169 ± 0.0026	0.0181 ± 0.0027	52.4 ± 7.2	25.3 ± 4.5	27.1 ± 4.7
$B^+ \to \overline{D}^0 \rho^+$; $\overline{D}^0 \to K^+\pi^-$	509.2 ± 69.5	0.0253 ± 0.0025	0.0128 ± 0.0018	0.0125 ± 0.0017	29.9 ± 5.0	15.1 ± 2.9	14.8 ± 2.9
$B^+ \to \overline{D}^0 \rho^+$; $\overline{D}^0 \to K^+\pi^-\pi^0$	1742 ± 257	0.0048 ± 0.0013	0.00238 ± 0.00090	0.00238 ± 0.00090	19.2 ± 5.9	9.6 ± 3.9	9.6 ± 3.9
$B^+ \to \overline{D}^{*0} \pi^+$; $\overline{D}^{*0} \to \overline{D}^0\gamma$; $\overline{D}^0 \to K^+\pi^-$	66.6 ± 7.9	0.0913 ± 0.0083	0.0377 ± 0.0053	0.0536 ± 0.0064	14.1 ± 2.1	5.8 ± 1.1	8.3 ± 1.4
$B^+ \to \overline{D}^{*0} \pi^+$; $\overline{D}^{*0} \to \overline{D}^0\gamma$; $\overline{D}^0 \to K^+\pi^-\pi^0$	227.8 ± 29.8	0.0076 ± 0.0025	0.0059 ± 0.0022	0.0017 ± 0.0012	4.0 ± 1.4	3.1 ± 1.2	0.89 ± 0.64
$B^+ \to \overline{D}^{*0} \pi^+$; $\overline{D}^{*0} \to \overline{D}^0\pi^0$; $\overline{D}^0 \to K^+\pi^-$	108.2 ± 11.0	0.0785 ± 0.0068	0.0471 ± 0.0052	0.0314 ± 0.0043	19.7 ± 2.6	11.8 ± 1.8	7.9 ± 1.3
$B^+ \to \overline{D}^{*0} \pi^+$; $\overline{D}^{*0} \to \overline{D}^0\pi^0$; $\overline{D}^0 \to K^+\pi^-\pi^0$	370.2 ± 43.1	0.0060 ± 0.0016	0.0034 ± 0.0012	0.0026 ± 0.0011	5.2 ± 1.5	3.0 ± 1.1	2.22 ± 0.94
$B^+ \to \overline{D}^0 e^+\nu_e$; $\overline{D}^0 \to K^+\pi^-$	817.0 ± 85.8	0.00272 ± 0.00096	0.00136 ± 0.00068	0.00136 ± 0.00068	5.2 ± 1.9	2.6 ± 1.3	2.6 ± 1.3
$B^+ \to \overline{D}^0 e^+\nu_e$; $\overline{D}^0 \to K^+\pi^-\pi^0$	2795 ± 334	0.00136 ± 0.00068	0.00 ± 0.00	0.00136 ± 0.00068	8.8 ± 4.5	0.0 ± 0.0	8.8 ± 4.5
$B^+ \to \overline{D}^0 \mu^+\nu_\mu$; $\overline{D}^0 \to K^+\pi^-$	817.0 ± 85.8	0.0044 ± 0.0012	0.00170 ± 0.00076	0.00272 ± 0.00096	8.4 ± 2.5	3.2 ± 1.5	5.2 ± 1.9
$B^+ \to \overline{D}^0 \mu^+\nu_\mu$; $\overline{D}^0 \to K^+\pi^-\pi^0$	2795 ± 334	0.00206 ± 0.00084	0.00069 ± 0.00048	0.00137 ± 0.00069	13.3 ± 5.7	4.4 ± 3.2	8.9 ± 4.6
$B^+ \to \overline{D}^{*0} e^+\nu_e$; $\overline{D}^{*0} \to \overline{D}^0\gamma$; $\overline{D}^0 \to K^+\pi^-$	941.1 ± 104.2	0.00138 ± 0.00069	0.00138 ± 0.00069	0.00 ± 0.00	3.0 ± 1.5	3.0 ± 1.5	0.0 ± 0.0
$B^+ \to \overline{D}^{*0} e^+\nu_e$; $\overline{D}^{*0} \to \overline{D}^0\gamma$; $\overline{D}^0 \to K^+\pi^-\pi^0$	3219 ± 401	0.00282 ± 0.00010	0.00247 ± 0.00094	0.00035 ± 0.00035	21.1 ± 7.9	18.4 ± 7.3	2.6 ± 2.7
$B^+ \to \overline{D}^{*0} \mu^+\nu_\mu$; $\overline{D}^{*0} \to \overline{D}^0\gamma$; $\overline{D}^0 \to K^+\pi^-$	941.1 ± 104.2	0.0031 ± 0.0010	0.00139 ± 0.00069	0.00174 ± 0.00078	6.8 ± 2.4	3.0 ± 1.6	3.8 ± 1.7
$B^+ \to \overline{D}^{*0} \mu^+\nu_\mu$; $\overline{D}^{*0} \to \overline{D}^0\gamma$; $\overline{D}^0 \to K^+\pi^-\pi^0$	3219 ± 401	0.00068 ± 0.00048	0.00 ± 0.00	0.00068 ± 0.00048	5.1 ± 3.6	0.0 ± 0.0	5.1 ± 3.6
$B^+ \to \overline{D}^{*0} e^+\nu_e$; $\overline{D}^{*0} \to \overline{D}^0\pi^0$; $\overline{D}^0 \to K^+\pi^-$	1529 ± 142	0.00102 ± 0.00059	0.00068 ± 0.00048	0.00034 ± 0.00034	3.6 ± 2.1	2.4 ± 1.7	1.2 ± 1.2
$B^+ \to \overline{D}^{*0} e^+\nu_e$; $\overline{D}^{*0} \to \overline{D}^0\pi^0$; $\overline{D}^0 \to K^+\pi^-\pi^0$	5231 ± 571	0.00206 ± 0.00084	0.00103 ± 0.00059	0.00103 ± 0.00059	24.9 ± 10.5	12.5 ± 7.3	12.5 ± 7.3
$B^+ \to \overline{D}^{*0} \mu^+\nu_\mu$; $\overline{D}^{*0} \to \overline{D}^0\pi^0$; $\overline{D}^0 \to K^+\pi^-$	1529 ± 142	0.00204 ± 0.00083	0.00034 ± 0.00034	0.00170 ± 0.00076	7.2 ± 3.0	1.2 ± 1.2	6.0 ± 2.8
$B^+ \to \overline{D}^{*0} \mu^+\nu_\mu$; $\overline{D}^{*0} \to \overline{D}^0\pi^0$; $\overline{D}^0 \to K^+\pi^-\pi^0$	5231 ± 571	0.00068 ± 0.00048	0.00034 ± 0.00034	0.00034 ± 0.00034	8.3 ± 5.9	4.1 ± 4.1	4.1 ± 4.1
Total Charm Charged B backgrounds					407 ± 23	205 ± 15	202 ± 15

Table 4.3: *Charmless B^+B^- background modes, with branching fractions, efficiencies and number of expected events. For vector-vector modes only the longitudinal polarisation is found to contribute significantly.*

Mode	BF	Signal Box Efficiency			Number of Expected Events in Signal Box		
	(10^{-6})	All	B^+	B^-	All	B^+	B^-
$B^+ \to K^+K^-K^+$	30.1 ± 1.9	0.0339 ± 0.0016	0.0177 ± 0.0012	0.0162 ± 0.0011	2.36 ± 0.19	1.23 ± 0.11	1.13 ± 0.11
$B^+ \to K^+K^-\pi^+$	< 6.3	0.7813 ± 0.0077	0.3880 ± 0.0055	0.3834 ± 0.0054	5.7 ± 5.7	2.9 ± 2.9	2.8 ± 2.8
$B^+ \to \pi^+\pi^-\pi^+$	16.2 ± 2.5	0.4859 ± 0.0047	0.2437 ± 0.0033	0.2422 ± 0.0033	18.2 ± 2.8	9.2 ± 1.2	9.1 ± 1.4
$B^+ \to K^{*+}\gamma$	40.3 ± 2.6	0.00275 ± 0.00080	0.00115 ± 0.00051	0.00161 ± 0.00061	0.257 ± 0.076	0.107 ± 0.048	0.150 ± 0.058
$B^+ \to K^{*+}K^{*0}$; $K^{*+} \to K^0\pi^+$; $K^{*0} \to K^+\pi^-$	< 15.8	0.0172 ± 0.0038	0.0090 ± 0.0027	0.0082 ± 0.0026	0.31 ± 0.32	0.16 ± 0.17	0.15 ± 0.15
$B^+ \to K^{*+}K^{*0}$; $K^{*+} \to K^+\pi^0$; $K^{*0} \to K^+\pi^-$	< 7.9	0.0397 ± 0.0056	0.0206 ± 0.0040	0.0290 ± 0.0039	0.36 ± 0.37	0.19 ± 0.19	0.17 ± 0.18
$B^+ \to \rho^+K^{*0}$; $K^{*0} \to K^+\pi^-$	3.07 ± 0.67	0.0905 ± 0.0034	0.0458 ± 0.0024	0.0448 ± 0.0024	0.64 ± 0.14	0.325 ± 0.073	0.318 ± 0.071
$B^+ \to \rho^0K^{*+}$; $K^{*+} \to K^+\pi^0$	1.8 ± 0.6	0.1811 ± 0.0095	0.0856 ± 0.0065	0.0955 ± 0.0069	0.74 ± 0.26	0.35 ± 0.12	0.39 ± 0.14
$B^+ \to \rho^+\rho^0$	26.4 ± 6.2	0.0588 ± 0.0041	0.0341 ± 0.0031	0.0247 ± 0.0026	3.60 ± 0.88	2.09 ± 0.53	1.51 ± 0.39
$B^+ \to \eta' K^+$; $\eta' \to \pi^+\pi^-\gamma$	22.9 ± 1.6	0.710 ± 0.022	0.371 ± 0.016	0.339 ± 0.015	37.7 ± 2.9	19.7± 1.6	18.0± 1.5
$B^+ \to \eta'\pi^+$; $\eta' \to \pi^+\pi^-\gamma$	1.24 ± 0.33	0.1158 ± 0.0089	0.0603 ± 0.0064	0.0555 ± 0.0062	0.332± 0.092	0.173 ± 0.049	0.159 ± 0.046
$B^+ \to K_s^0K^+$;	0.14 ± 0.14	6.175 ± 0.0056	3.134 ± 0.0041	3.141 ± 0.0040	5.9 ± 5.9	3.0 ± 3.0	2.9 ± 2.9
$B^+ \to K_s^0\pi^+$;	8.31 ± 0.45	0.228 ± 0.010	0.1160 ± 0.0072	0.1132 ± 0.0072	4.40 ± 0.31	2.23 ± 0.19	2.16 ± 0.18
Total Charmless Charged B backgrounds					81 ± 9	42 ± 5	39 ± 5

118

Table 4.4: *Charm $B^0\overline{B}^0$ background modes, with branching fractions, efficiencies and number of expected events.*

Mode	BF	Signal Box Efficiency (%)			Number of Expected Events in Signal Box		
	(10^{-6})	All	B^+	B^-	All	B^+	B^-
$B^0 \to D^- K^+$; $D^- \to \pi^-\pi^0$	0.52 ± 0.21	0.1417 ± 0.0069	0.0664 ± 0.0047	0.0753 ± 0.0050	0.171 ± 0.069	0.080 ± 0.033	0.091 ± 0.038
$B^0 \to \overline{D}^0\rho^0$; $\overline{D}^0 \to K^+\pi^-$	11.0 ± 4.2	0.0300 ± 0.0065	0.0214 ± 0.0055	0.0086 ± 0.0035	0.77 ± 0.34	0.55 ± 0.25	0.22 ± 0.12
$B^0 \to D^{*-}\pi^+$; $D^{*-} \to \overline{D}^0\pi^-$; $\overline{D}^0 \to X$	1870 ± 143	0.00431 ± 0.00032	0.00232 ± 0.00023	0.00199 ± 0.00022	18.7 ± 2.0	10.0 ± 1.3	8.6 ± 1.2
$B^0 \to D^{*-}\rho^+$; $D^{*-} \to \overline{D}^0\pi^-$; $\overline{D}^0 \to X$	4600 ± 610	0.00019 ± 0.00013	0.00 ± 0.00	0.00019 ± 0.00013	2.0 ± 1.5	0.00 ± 0.00	2.0 ± 1.5
$B^0 \to \overline{D}^{*0}\rho^0$; $\overline{D}^{*0} \to \overline{D}^0\gamma$ or $\overline{D}^0\pi^0$; $\overline{D}^0 \to K^+\pi^-$	9.69 ± 9.69	0.0021 ± 0.0012	0.00 ± 0.00	0.0021 ± 0.0012	0.048 ± 0.056	0.00 ± 0.00	0.048 ± 0.056
Total Charm Neutral B backgrounds					22 ± 2	11 ± 1	11 ± 2

Table 4.5: *Charmless $B^0\overline{B}^0$ background modes, with branching fractions, efficiencies and number of expected events. For vector-vector modes only the longitudinal polarisation is found to contribute significantly.*

Mode	BF	Signal Box Efficiency (%)			Number of Expected Events in Signal Box		
	(10^{-6})	All	B^+	B^-	All	B^+	B^-
$B^0 \to K^+K^-\pi^0$	< 19	0.0373 ± 0.0054	0.0222 ± 0.0042	0.0151 ± 0.0035	0.82 ± 0.83	0.49 ± 0.49	0.33 ± 0.34
$B^0 \to K^+\pi^-\pi^0$	35.6 ± 3.4	0.0905 ± 0.0020	0.0446 ± 0.0014	0.0459 ± 0.0014	7.47 ± 0.74	3.68 ± 0.37	3.79 ± 0.38
$B^0 \to \pi^+\pi^-\pi^0$	< 72	0.0261 ± 0.0011	0.01324 ± 0.00079	0.01282 ± 0.00078	2.2 ± 2.2	1.1 ± 1.1	1.1 ± 1.1
$B^0 \to K_2^{*0}(1430)\gamma$	12.4 ± 2.4	0.0092 ± 0.0022	0.0049 ± 0.0016	0.0044 ± 0.0015	0.266 ± 0.083	0.141 ± 0.054	0.125 ± 0.050
$B^0 \to K^{*0}(1410)\gamma$	< 130	0.00208 ± 0.00085	0.00139 ± 0.00069	0.00069 ± 0.00049	0.32 ± 0.34	0.21 ± 0.23	0.10 ± 0.13
$B^0 \to K^{*0}\gamma$	40.1 ± 2.1	0.0099 ± 0.0016	0.0059 ± 0.0012	0.0041 ± 0.0010	0.92 ± 0.16	0.55 ± 0.12	0.379 ± 0.097
$B^0 \to K^{*0}\overline{K}^{*0}$; $K^{*0} \to K^+\pi^-$; $\overline{K}^{*0} \to K^-\pi^+$	< 4.9	0.0475 ± 0.0062	0.0189 ± 0.0039	0.0287 ± 0.0048	0.27 ± 0.27	0.11 ± 0.11	0.16 ± 0.16
$B^0 \to K^+\pi^-$	18.2 ± 0.8	0.0646 ± 0.0019	0.0335 ± 0.0013	0.0311 ± 0.0013	2.72 ± 0.15	1.414 ± 0.085	1.311 ± 0.081
$B^0 \to \rho^+K^-$	9.9 ± 1.6	0.766 ± 0.011	0.3978 ± 0.0078	0.3686 ± 0.0075	17.6 ± 2.9	9.1 ± 1.5	8.5 ± 1.4
$B^0 \to \rho^+K^{*-}$; $K^{*+} \to K^+\pi^0$	< 8	0.125 ± 0.032	0.083 ± 0.026	0.042 ± 0.019	1.2 ± 1.2	0.77 ± 0.81	0.39 ± 0.42
$B^0 \to \rho^0K^{*0}$; $K^{*0} \to K^+\pi^-$	< 0.86	0.1708 ± 0.0092	0.0842 ± 0.0065	0.0866 ± 0.0065	0.17 ± 0.17	0.085 ± 0.085	0.087 ± 0.087
$B^0 \to \rho^+\rho^-$	30.0 ± 6.0	0.0486 ± 0.0010	0.02553 ± 0.00076	0.02307 ± 0.00073	3.38 ± 0.68	1.78 ± 0.36	1.60 ± 0.33
$B^0 \to \rho^0\rho^0$	< 1.1	0.0970 ± 0.0069	0.0434 ± 0.0046	0.0537 ± 0.0051	0.12 ± 0.12	0.055 ± 0.056	0.069 ± 0.069
Total Charmless Neutral B backgrounds					37 ± 4	19 ± 2	18 ± 2

4.5.2 $q\overline{q}$ background

Light quark, or continuum, background is by far the dominant source of background in most charmless decays and the $B^+ \to K^+\pi^-\pi^+$ mode is no exception. For a B event, in the $\Upsilon(4S)$ rest frame, the two B mesons are produced almost at rest and there is no preferred direction for their decay products. The event is therefore said to be "spherical". Continuum events however are produced with momentum and their decay products form two highly collimated, back-to-back jets. As such event topology variables are used to discriminate between signal and continuum events. These variables have been described in Section 3.5.2 and the selection criteria applied to $|\cos\theta_T|$ and the Fisher discriminant have been enumerated in Table 4.1.

The $q\overline{q}$ background that remains after the selection cuts must be modelled in the amplitude fit. The off-peak data sample is used to characterise the distribution of these events in the Dalitz plot. However, the off-peak statistics are small and this would lead to large systematic uncertainties on the continuum Dalitz plot distribution, so the events from the on-peak $m_{\rm ES}$ sideband (defined in Table 4.1) are used to boost the statistics. However, the on-peak sideband will, in addition to $q\overline{q}$ events, contain background from B-meson decays and so it is first necessary to subtract this contribution. This is done by forming a Dalitz plot histogram from the events in the MC samples of the $B\overline{B}$ backgrounds that fall in the $m_{\rm ES}$ sideband. This histogram is then subtracted from the on-peak sideband histogram to form a distribution that is purely due to $q\overline{q}$ background events. The shape of the distribution is checked against that of the off-peak data and is found to be in excellent agreement. The comparison between the B-background subtracted on-peak data and the off-peak data can be seen in Figure 4.10 and Figure 4.11. The combined off-peak and $B\overline{B}$ background subtracted on-peak distribution can be seen in Figure 4.15. A fit to the variable $m_{\rm ES}$, which is described fully in Section 4.6, determines the number of $q\overline{q}$ events present in the signal box.

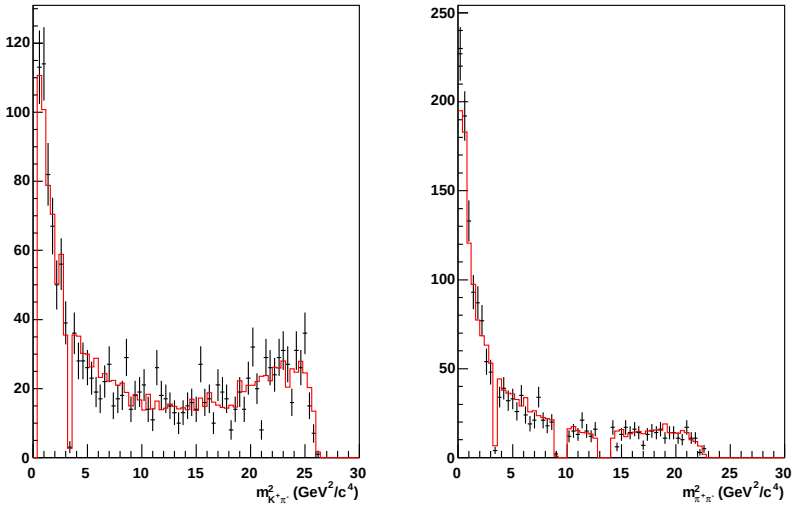

Figure 4.10: *Dalitz plot projections comparing the $B\overline{B}$ subtracted on-peak sideband (red/solid histogram) with off-peak data (black points).*

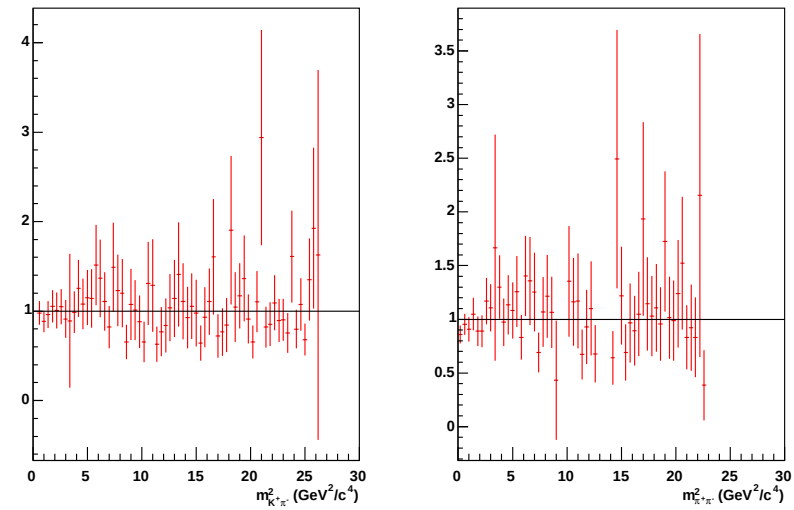

Figure 4.11: *The ratio of the $B\overline{B}$ subtracted on-peak sideband and off-peak data Dalitz projections.*

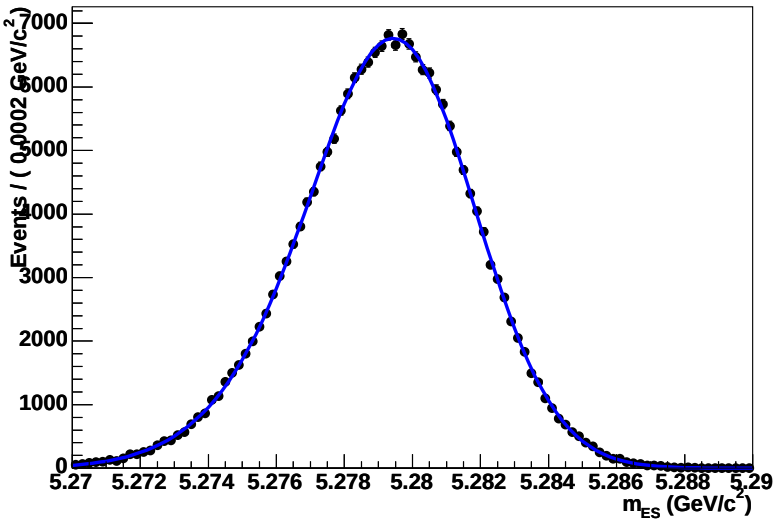

Figure 4.12: *The $m_{\rm ES}$ distribution of $B^+ \to K^+\pi^-\pi^+$ non resonant events fitted with a Double Gaussian.*

4.6 Determination of Signal and $q\overline{q}$ Background Yields

The fraction of events in the signal box due to continuum background is determined from a 1-dimensional fit to the $m_{\rm ES}$ (Eq. (3.5)) distribution of the events in the signal strip defined in Table 4.1. The fit is performed using the `CharmlessFitter` package (Section 3.6.3).

The signal $m_{\rm ES}$ distribution is modelled by a Double Gaussian function, the parameters of which are obtained from truth matched $B^+ \to K^+\pi^-\pi^+$ non resonant MC, see Figure 4.12. These parameters are fixed except for the mean of the core Gaussian. The continuum distribution is modelled by the experimentally motivated Argus function [67], shown in Figure 4.13. The endpoint of the Argus function is fixed to the beam energy, while the shape parameter is allowed to float. The number of signal and continuum events are floated in the fit. The $m_{\rm ES}$ distributions of the various $B\overline{B}$ backgrounds are found to have both peaking and non-peaking parts. As

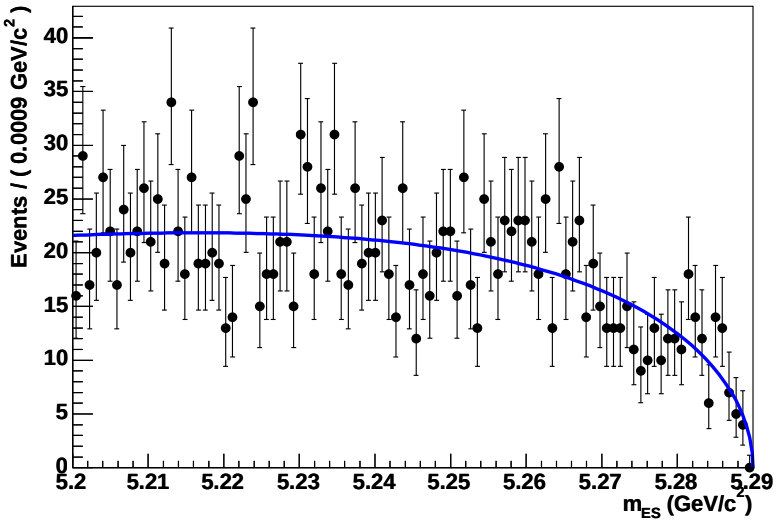

Figure 4.13: *The m_{ES} distribution of off-peak data events fitted with an Argus function.*

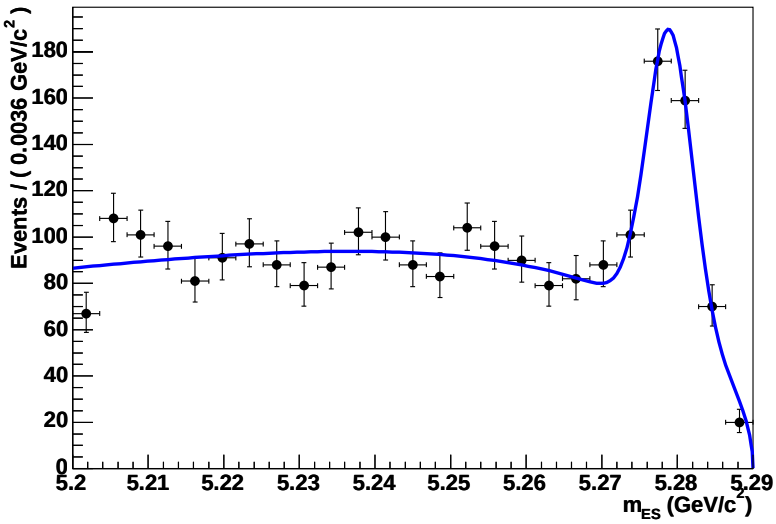

Figure 4.14: *The m_{ES} distribution of $B\overline{B}$ background events fitted with the sum of an Argus function and a Gaussian.*

such they are parameterised by the sum of an Argus function and a Gaussian, see Figure 4.14. All the $B\overline{B}$ parameters are fixed from the MC and the number of expected events is also fixed from the MC efficiencies and the world average branching fractions. However, as a cross check, the fit was performed allowing the number of $B\overline{B}$ events to float. The number of signal and continuum events obtained from this fit agreed very well with those from the nominal fit. In addition, the number of fitted $B\overline{B}$ events agreed very well with the number expected from MC. The parameters of each of the PDFs are given in Appendix A. The results of the fit to data are presented in Section 5.2.

4.7 Dalitz Plot Amplitude Fitting

The concept of the interference of modes within a Dalitz plot was introduced in Section 1.3.4. Here I will show how this complex interaction can be modelled in the amplitude fit. The amplitude fit is performed using the `Laura++` package [60], which is a `Root` based package designed to study 3-body charmless B-decay Dalitz plots.

In terms of a Dalitz-plot analysis of the decay $B^+ \to K^+\pi^-\pi^+$ a number of intermediate states contribute and the total rate can be represented in the form:

$$\frac{d\Gamma}{dm^2_{K^+\pi^-}dm^2_{\pi^+\pi^-}} = |\mathcal{M}|^2 = \left|\sum_j c_j e^{i\theta_j} F_j(m^2_{K^+\pi^-}, m^2_{\pi^+\pi^-})\right|^2 \tag{4.4}$$

where $m^2_{K^+\pi^-}$ and $m^2_{\pi^+\pi^-}$ are the squares of the invariant masses of the $K^+\pi^-$ and $\pi^+\pi^-$ pairs. The amplitude for a given decay mode is $c_j e^{i\theta_j} F_j(m^2_{K^+\pi^-}, m^2_{\pi^+\pi^-})$, where c_j and θ_j are the unknown real parameters of each partial decay mode, while F_j describes the dynamics of the amplitudes. These F_j consist of a product of the invariant mass and angular distribution probabilities:

$$F_j = R_j(m) \times T_j(\cos\theta_H) \tag{4.5}$$

where $R_j(m)$ is the resonance mass distribution (Section 1.3.2) and $T_j(\cos\theta_H)$ is the angular probability distribution (Section 1.3.3).

4.7.1 The Likelihood Function

To fit the data in the signal box, an unbinned likelihood function for one event is defined to have the form:

$$\mathcal{L}(m^2_{K^+\pi^-}, m^2_{\pi^+\pi^-}) = (1 - f_{q\bar{q}} - f_{B\bar{B}}) \tag{4.6}$$
$$\frac{\left|\sum_{j=1}^{N} c_j e^{i\theta_j} F_j(m^2_{K^+\pi^-}, m^2_{\pi^+\pi^-})\right|^2 \epsilon(m^2_{K^+\pi^-}, m^2_{\pi^+\pi^-})}{\int\int_{DP} \left|\sum_{j=1}^{N} c_j e^{i\theta_j} F_j(m^2_{K^+\pi^-}, m^2_{\pi^+\pi^-})\right|^2 \epsilon(m^2_{K^+\pi^-}, m^2_{\pi^+\pi^-}) dm^2_{K^+\pi^-} dm^2_{\pi^+\pi^-}}$$
$$+ f_{q\bar{q}} \frac{Q(m^2_{K^+\pi^-}, m^2_{\pi^+\pi^-})}{\int\int_{DP} Q(m^2_{K^+\pi^-}, m^2_{\pi^+\pi^-})\, dm^2_{K^+\pi^-} dm^2_{\pi^+\pi^-}}$$
$$+ f_{B\bar{B}} \frac{B(m^2_{K^+\pi^-}, m^2_{\pi^+\pi^-})}{\int\int_{DP} B(m^2_{K^+\pi^-}, m^2_{\pi^+\pi^-})\, dm^2_{K^+\pi^-} dm^2_{\pi^+\pi^-}}$$

where

- N is the number of resonant and non resonant contributions to the plot;
- $\epsilon(m^2_{K^+\pi^-}, m^2_{\pi^+\pi^-})$ is the reconstruction efficiency defined for all points in the Dalitz plot;
- $Q(m^2_{K^+\pi^-}, m^2_{\pi^+\pi^-})$ is the distribution of $q\overline{q}$ continuum background;
- $B(m^2_{K^+\pi^-}, m^2_{\pi^+\pi^-})$ is the distribution of $B\overline{B}$ background; and
- $f_{q\overline{q}}$ and $f_{B\overline{B}}$ are the fractions of $q\overline{q}$ and $B\overline{B}$ background events, respectively.

The fit is performed allowing the amplitude magnitudes (c_j) and the phases (θ_j) to vary. The first term on the right-hand-side in Eq. (4.6) corresponds to the signal probability density function (PDF) multiplied by the signal fraction $(1 - f_{q\overline{q}} - f_{B\overline{B}})$. Since a common factor can always be applied to both the numerator and denominator of the signal PDF, this analysis will only be sensitive to relative phases and magnitudes, and hence it is possible to fix the magnitude and phase of one component. In this analysis the well measured mode $B^+ \to K^{*0}(892)\pi^+$, $K^{*0}(892) \to K^+\pi^-$ is chosen to be fixed.

As the choice of normalisation, phase convention and amplitude formalism may not always be the same for different experiments, "Fit Fractions" are presented instead of amplitude magnitudes to allow a more meaningful comparison of results. The fit fraction is defined as the integral of a single decay amplitude squared divided by the coherent matrix element squared for the complete Dalitz plot:

$$FF_j = \frac{\int\int_{DP} \left| c_j e^{i\theta_j} F_j(m^2_{K^+\pi^-}, m^2_{\pi^+\pi^-}) \right|^2 dm^2_{K^+\pi^-} dm^2_{\pi^+\pi^-}}{\int\int_{DP} \left| \sum_j c_j e^{i\theta_j} F_j(m^2_{K^+\pi^-}, m^2_{\pi^+\pi^-}) \right|^2 dm^2_{K^+\pi^-} dm^2_{\pi^+\pi^-}} \tag{4.7}$$

Note that the sum of these fit fractions is not necessarily unity due to the potential presence of net constructive or destructive interference.

Similarly the fit fraction for the conjugate $B^- \to K^-\pi^+\pi^-$ process is defined to be:

$$\overline{FF}_j = \frac{\int\int_{DP} \left| \bar{c}_j e^{i\bar{\theta}_j} F_j(m^2_{K^-\pi^+}, m^2_{\pi^-\pi^+}) \right|^2 dm^2_{K^-\pi^+} dm^2_{\pi^-\pi^+}}{\int\int_{DP} \left| \sum_j \bar{c}_j e^{i\bar{\theta}_j} F_j(m^2_{K^-\pi^+}, m^2_{\pi^-\pi^+}) \right|^2 dm^2_{K^-\pi^+} dm^2_{\pi^-\pi^+}} \tag{4.8}$$

Furthermore the fit fraction asymmetry is defined to be:

$$A_j^{FF} = \frac{\overline{FF}_j - FF_j}{\overline{FF}_j + FF_j} \tag{4.9}$$

These definitions follow those in [68]. The B^+ and B^- samples are fitted separately and the results combined to find the fit fraction asymmetry.

4.7.2 Signal Model

The following resonances are included in the nominal signal amplitude model, in addition to a non resonant component:

- $\diamond$ $K^{*0}(892)$
- $\diamond$ $K_0^{*0}(1430)$
- $\diamond$ $\rho^0(770)$
- $\diamond$ $f_0(980)$

- χ_{c0}

Each resonance is modelled with a Relativistic Breit–Wigner lineshape with Blatt–Weisskopf barrier factors (Section 1.3.2.1) apart from the $f_0(980)$, which is modelled using the Flatté lineshape (Section 1.3.2.2) and the $K_0^{*0}(1430)$, which uses the LASS lineshape (Eq. (1.66)). The non resonant component is modelled as flat phase space. The χ_{c0} is included despite being a charm state because it is considerably wider than states like the J/ψ and D^0, which are vetoed in this analysis, and so can interfere significantly with the charmless modes. Indeed there are proposals of methods for measuring the CKM angle γ through the interference of the χ_{c0} with the non resonant decay, see for example [69].

As well as the nominal model I will also perform fits using other models, which will test for the presence of other higher resonances and for different lineshape parameters for some of the less well established systems. As indications of goodness of fit a combination of the following is used: the negative log likelihood (NLL) from the fit, 1-dimensional χ^2 values from comparison of data and fit result in each of the three invariant mass projections ($m_{K^+\pi^-}$, $m_{\pi^+\pi^-}$, $m_{K^+\pi^+}$), and a 2-dimensional χ^2 formed from comparing data and the fit result across the Dalitz plot. This combined information will be used to determine which of the models best describes the data. The potential higher resonances tested for are:

- $K_2^{*0}(1430)$
- $K^{*0}(1680)$
- $f_2(1270)$
- $f_0(1370)$
- $\rho^0(1450)$
- $f_0(1500)$
- $f_2'(1525)$

4.7.3 Efficiency Model

The variation of the efficiency of signal reconstruction across the Dalitz plot has been discussed in detail in Section 4.4.1. In the `Laura++` likelihood function the efficiency variation is modelled by a linearly interpolated 2-dimensional histogram, which is determined from $B^+ \to K^+\pi^-\pi^+$ non resonant MC. It is seen that the efficiency variation across the Dalitz plot is the same for $B^+ \to K^+\pi^-\pi^+$ and $B^- \to K^-\pi^+\pi^-$ events and so the combined histogram is used to boost the statistical precision. The histogram used in this analysis is shown in Figure 4.4. In the charm veto bands the efficiency is set to zero.

One output from the fit is the correctly averaged efficiency over the Dalitz plot; *i.e.* not simply assuming a phase space distribution of the signal events (as is the case in Table 4.1) but using the distributions as determined from the amplitude fit:

$$\bar{\epsilon} = \frac{\int\int_{DP} \left|\sum_j c_j e^{i\theta_j} F_j(m^2_{K^+\pi^-}, m^2_{\pi^+\pi^-})\right|^2 \epsilon(m^2_{K^+\pi^-}, m^2_{\pi^+\pi^-}) dm^2_{K^+\pi^-} dm^2_{\pi^+\pi^-}}{\int\int_{DP} \left|\sum_j c_j e^{i\theta_j} F_j(m^2_{K^+\pi^-}, m^2_{\pi^+\pi^-})\right|^2 dm^2_{K^+\pi^-} dm^2_{\pi^+\pi^-}} \quad (4.10)$$

The determination of the average efficiency in this way means that the effect of the variation of the efficiency over the Dalitz plane, including the charm vetoes, is correctly accounted for in the calculation of the total branching fraction.

4.7.4 Background Model

The various sources of background have been discussed in detail in Section 4.5. In the amplitude fit both the $q\overline{q}$ and $B\overline{B}$ backgrounds are modelled as linearly interpolated 2-dimensional histograms. It is seen that the distribution for $q\overline{q}$ is the same for $B^+ \to K^+\pi^-\pi^+$ and $B^- \to K^-\pi^+\pi^-$ events and so the combined histogram is used in order to reduce the uncertainty on the shape of the distribution. This combined histogram is shown in Figure 4.15. For $B\overline{B}$ on the other hand there are noticeable differences in the separate charge distributions. This may be due to low statistics in some of the MC samples. However, an actual asymmetry in the selection

efficiency cannot be discounted and so the separate charge histograms are used in the fit. The shape of these distributions can be seen in Figure 4.16.

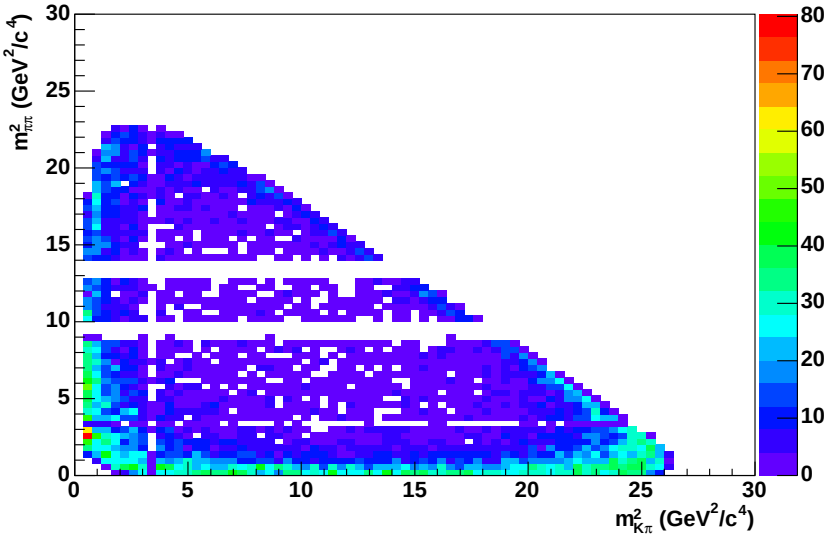

Figure 4.15: *Dalitz plot distribution for continuum ($q\overline{q}$) background events.*

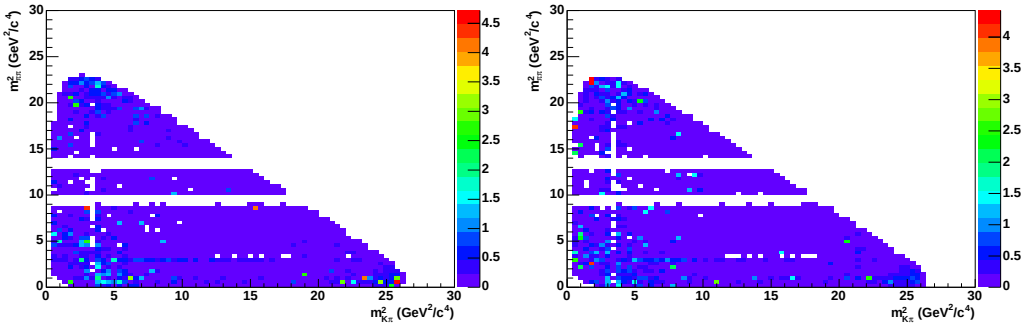

Figure 4.16: *Dalitz plot distribution for $B\overline{B}$ background events.*
The left hand plot is for B^+ events and the right hand plot is for B^- events.

4.8 Numerical Integration

The Dalitz amplitude likelihood function, Eq. (4.6), contains several instances of an integral over the Dalitz plot or the three body phase space. The integral of the signal

term must be performed numerically since the complex interference terms do not have analytic integrals. This numeric integration is performed within the `Laura++` package using the techniques of Gauss–Legendre integration, which will be briefly described here but is discussed in more detail in [70].

Gauss–Legendre integration allows a set of weights (w_j) and positions (x_j) to be chosen such that the approximation

$$\int_{x_1}^{x_2} f(x)dx \approx \sum_{j=1}^{N} w_j f(x_j) \tag{4.11}$$

is exact if $f(x)$ is a polynomial and N tends to infinity. Sufficiently fine sampling, *i.e.* large N, permits this approximation to be used for our signal likelihood function. The results from this method are checked using a Monte Carlo technique and are found to be the same. The Gauss–Legendre approach is used preferentially because it takes less CPU time.

The weights are calculated using the formula

$$w_j = \frac{2}{(1-x_j^2)[P'_N(x_j)]^2} \tag{4.12}$$

where $P'_N(x_j)$ is the derivative of the N^{th} Legendre polynomial evaluated at x_j.

5

Analysis Results

5.1 Introduction

This chapter presents the results of the analysis. Their implications with reference to theoretical predictions and results from other experiments are discussed in Chapter 6.

Firstly the fit to $m_{\rm ES}$, which is used to determine the signal and background yields, is presented along with the results for the total branching fraction of $B^+ \to K^+\pi^-\pi^+$ and the total charge asymmetry. Next, the results of toy MC and full simulation MC tests are presented to show that the Dalitz plot amplitude fit is stable and can consistently reproduce input parameter values. The results from the amplitude

fits to data are then presented. Finally the sources of systematic uncertainties are examined and their values determined from various studies.

5.2 Total Rate Results

In this section the results of the $m_{\rm ES}$ fit described in Section 4.6 are presented. The fit is performed to the B^+ and B^- samples separately as well as the combined sample. The combined sample data distribution is shown along with the fitted PDFs in Figure 5.1 and the results for all three fits are shown in Table 5.1.

Table 5.1: *The event yields from the 1D fit to $m_{\rm ES}$, the errors are from the fit for signal and $q\overline{q}$ background, whilst the error for $B\overline{B}$ background is from the uncertainty on the various branching fractions and efficiencies.*

Hypothesis	Number of Fitted Events in Signal Box	Composition of Events in Signal Box
Combined Sample		
Signal	2098 ± 81	0.446 ± 0.011
$q\overline{q}$ background	2059 ± 35	0.438 ± 0.010
$B\overline{B}$ background	547 ± 25	0.116 ± 0.006
Positive Sample		
Signal	1056 ± 57	0.447 ± 0.016
$q\overline{q}$ background	1027 ± 25	0.435 ± 0.014
$B\overline{B}$ background	277 ± 16	0.117 ± 0.007
Negative Sample		
Signal	1043 ± 57	0.445 ± 0.016
$q\overline{q}$ background	1031 ± 25	0.440 ± 0.014
$B\overline{B}$ background	270 ± 16	0.115 ± 0.007

The fit yields 1056 ± 57 signal events for the B^+ sample and 1043 ± 57 signal events for the B^- sample, which corresponds to an overall asymmetry of $(-0.5 \pm 3.9 \pm 2.1)\%$,

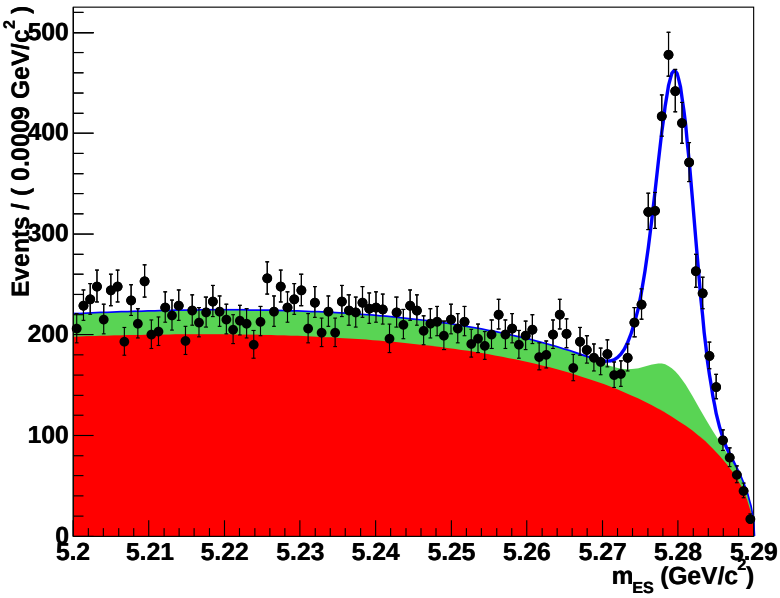

Figure 5.1: *$m_{\rm ES}$ distribution for the combined positive and negative samples, together with the fitted PDFs: the data are the black points, the lower solid red area is the $q\overline{q}$ component, the middle solid green area is the $B\overline{B}$ background contribution, while the upper blue line shows the total fit result. All errors shown are statistical only.*

where the first error is statistical and the second is systematic. Since this asymmetry is consistent with zero to a high degree of precision the number of fitted signal events from the combined fit can be used to get the branching fraction of $B^{\pm} \to K^{\pm}\pi^{\mp}\pi^{\pm}$. This branching fraction excludes the charm intermediate states $\overline{D}^0\pi^+$, $J/\psi\, K^+$ and $\psi(2S)K^+$. The branching fraction is given by

$$\mathcal{B}(B^{\pm} \to K^{\pm}\pi^{\mp}\pi^{\pm}) = \frac{N_{sig}}{\bar{\epsilon}\,\epsilon_c\, N_{B\overline{B}}} \tag{5.1}$$

where N_{sig} is the number of fitted signal events, $N_{B\overline{B}}$ is the number of $B\overline{B}$ pairs, $\bar{\epsilon}$ is the amplitude model weighted average efficiency, from Eq. (4.10), calculated using the nominal amplitude fit presented in Section 5.6 and ϵ_c is the efficiency correction due to the cuts on $\cos\theta_T$, Fisher, $m_{\rm ES}$ and ΔE. The method by which these efficiency corrections and their associated errors are obtained is described in Section 5.8.2 and

the values are given in Table 5.12. The result for the total branching fraction is:

$$\mathcal{B}(B^{\pm} \to K^{\pm}\pi^{\mp}\pi^{\pm}) = (64.4 \pm 2.5 \pm 4.6) \times 10^{-6} \tag{5.2}$$

where the first error is statistical and the second is systematic. The evaluation of the systematic error on this measurement and that of the asymmetry, above, is described in Section 5.8.2.

5.2.1 ${}_s\mathcal{P}lots$

Using the results and PDFs from the $m_{\rm ES}$ fit it is possible, using the ${}_s\mathcal{P}lots$ technique described in [71], to create histograms that show only the signal distribution of the data in a given variable. This is reliant on the fact that the $m_{\rm ES}$ PDFs are sufficiently discriminating between the different species. Toy Monte Carlo tests show negligible pulls in the number of signal events and number of background events. As such the ${}_s\mathcal{P}lot$ technique can be employed.

The ${}_s\mathcal{P}lots$ technique uses the PDFs, the values of the fitted number of events and the correlation matrix from the fit to calculate a weight for each event, called an ${}_s\mathcal{W}eight$. These ${}_s\mathcal{W}eights$ are properly normalised such that when they are summed over all the events in the sample they give the measured signal yield. It is also possible to calculate an ${}_s\mathcal{W}eight$ for each species in the fit and for each event these different species ${}_s\mathcal{W}eights$ sum to unity.

Following this technique we have produced signal distributions for the $K^+\pi^-$ and $\pi^+\pi^-$ invariant mass spectra, which can be seen in Figure 5.2. For each of these plots there is a requirement that the other invariant mass have a value greater than 2 GeV. The plots illustrate the structure of the Dalitz plot and help to inform the initial choice of contributions to include in the amplitude model. For illustration the ${}_s\mathcal{P}lot$ technique has also been used to produce a Dalitz plot of the signal events, which can be seen in Figure 5.3. This can be compared to the Dalitz plot of all the data in the signal box, which is shown in Figure 5.4.

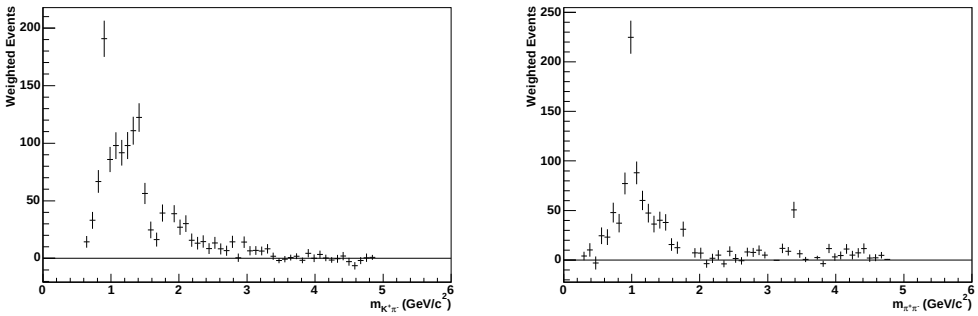

Figure 5.2: *Signal ${}_s\mathcal{P}lot$ distributions of $m_{K^+\pi^-}$ and $m_{\pi^+\pi^-}$. For the $m_{K^+\pi^-}$ plot the requirement is made that $m_{\pi^+\pi^-}$ be greater than 2 GeV and vice versa.*

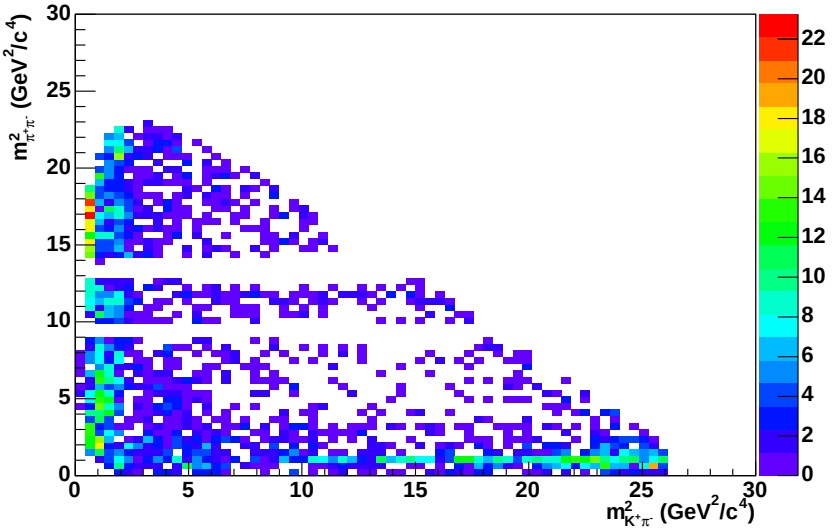

Figure 5.3: *Signal ${}_s\mathcal{P}lot$ of the $B^\pm \to K^\pm\pi^\mp\pi^\pm$ Dalitz plot.*

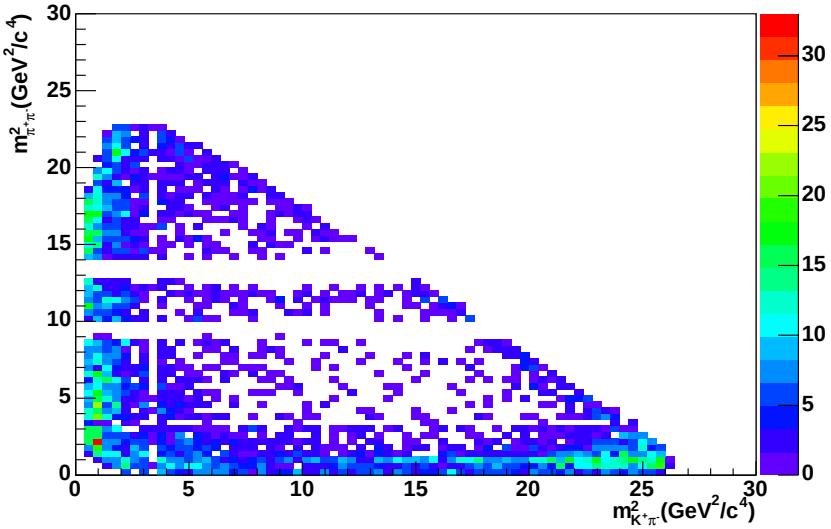

Figure 5.4: *The $B^{\pm} \to K^{\pm}\pi^{\mp}\pi^{\pm}$ Dalitz plot for all data in the signal box.*

5.3 Toy Monte Carlo Tests

The first important test to see whether the amplitude fit is performing correctly was to generate and fit toy experiments from the nominal fit model (Section 4.7.2). The values used for the magnitudes were approximately those expected from previous measurements of the branching fractions of the intermediate modes. The values for the background fractions and total number of events were fixed from the $m_{\rm ES}$ fit results just presented in Table 5.1. The phases were set to arbitrary values. Five hundred experiments were performed and in each of these the only floating parameters were the magnitudes and phases of the five floating components.

5.3.1 Multiple Solutions

One thing that became immediately apparent from these tests was that the fits were exhibiting multiple solutions. If two fits were performed to the same set of events but the starting values of the parameters were different then the two fits would not

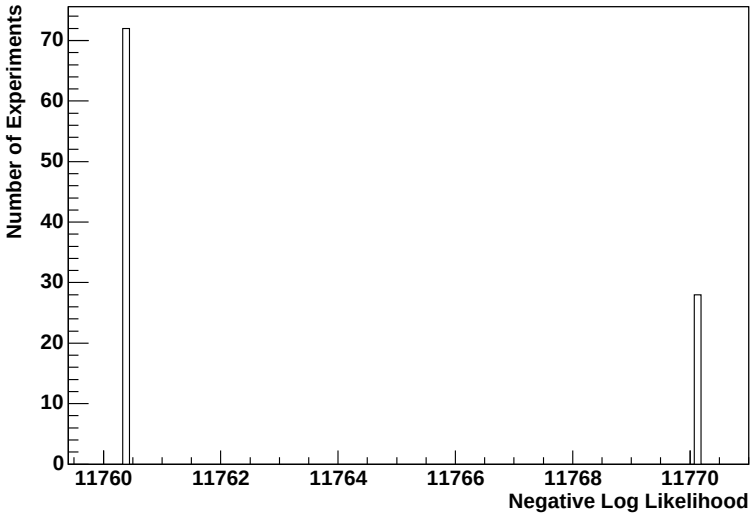

Figure 5.5: *Multiple solutions in the amplitude fit.*

necessarily converge to the same solution. The likelihood value and the values of one or more parameters would differ between the two solutions. The cause of this behaviour appears to be that the likelihood space is highly non-trivial and as such the fit can easily become stuck in a local minimum.

Several alternative solutions were investigated including the use of a *genetic algorithm* [72] but the technique employed in the analysis was that of multiple randomised fits. This involves performing $\mathcal{O}(100)$ fits to a given data sample, each with a different, random set of magnitudes and phases for the free parameters. It is seen that almost 100% of these fits converge, despite their often highly incorrect starting points, and a majority (often $> 80\%$) will converge to the solution with the best likelihood, as can be seen in Figure 5.5. From examining all the different possible solutions in toy experiments it is seen that this most favoured and best-likelihood solution is always the one closest to the generated parameters. The adopted practice for dealing with the multiple solutions behaviour is therefore to perform multiple randomised fits and to extract the solution with the best likelihood value.

5.3.2 Toy MC Test Results

For each of the 500 experiments performed the fitted values of the magnitudes and phases and their statistical errors were recorded for each of the $\mathcal{O}(100)$ fits. The fit with the best likelihood was then extracted for each experiment and the pulls for each floating parameter calculated according to Eq. (3.28) and recorded. The pull distributions for each floating parameter can be seen in Figure 5.6 and Figure 5.7. Table 5.2 shows the results of fitting a Gaussian to these pull distributions.

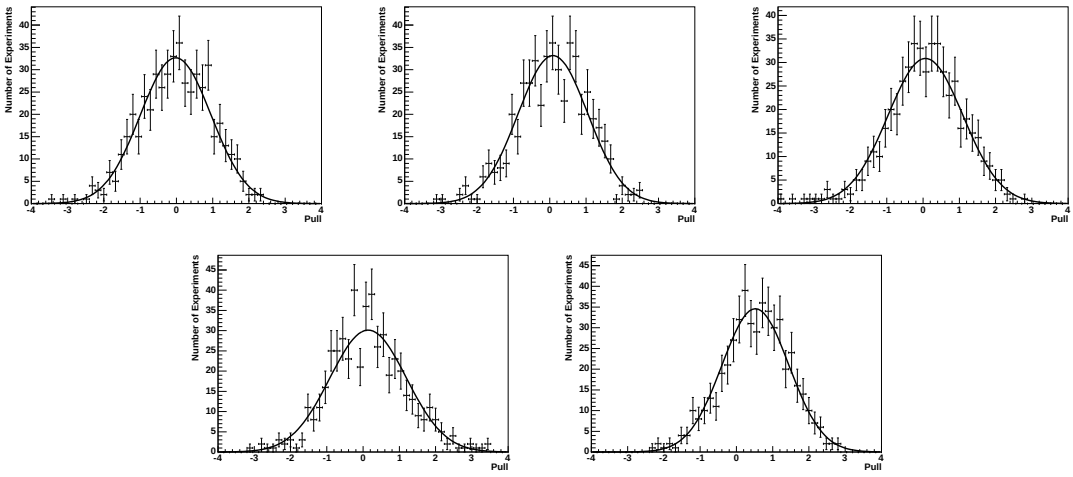

Figure 5.6: *Pull distributions for the magnitudes in the 500 toy tests. Top left shows the $K_0^{*0}(1430)$, top middle the $\rho^0(770)$, top right the $f_0(980)$, bottom left the χ_{c0} and bottom right the non resonant*

The magnitudes of the non resonant and χ_{c0} components as well as the phase of the non resonant component show significant pulls. The χ_{c0} is a very small component and the non resonant component, although not as small, is spread across the entire phase space. As such these components are particularly prone to statistical fluctuations. A set of toy experiments was also run with approximately ten times the expected statistics in which all the pulls were seen to be small. This confirms that the biases are due to statistical fluctuations. All components have additional systematic errors applied in order to account for any bias in the fit results. The

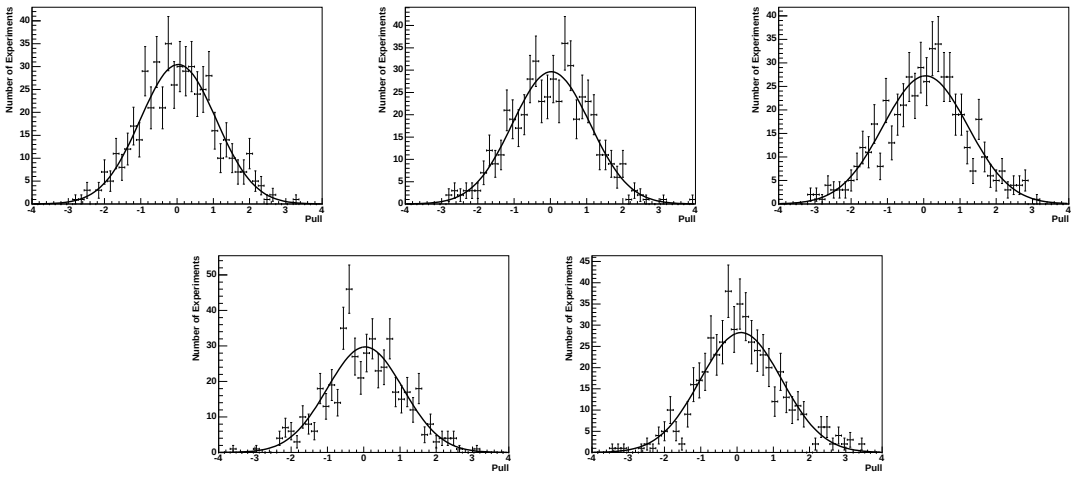

Figure 5.7: *Pull distributions for the phases in the 500 toy tests. Top left shows the $K_0^{*0}(1430)$, top middle the $\rho^0(770)$, top right the $f_0(980)$, bottom left the χ_{c0} and bottom right the non resonant*

Table 5.2: *Magnitude and Phase pulls in 500 toy tests with the six nominal components.*

Parameter	Pull Mean	Pull Width
$K_0^{*0}(1430)$ Magnitude	-0.020 ± 0.044	0.977 ± 0.031
$K_0^{*0}(1430)$ Phase	0.034 ± 0.047	1.045 ± 0.033
$\rho^0(770)$ Magnitude	0.090 ± 0.043	0.962 ± 0.031
$\rho^0(770)$ Phase	0.024 ± 0.048	1.072 ± 0.034
$f_0(980)$ Magnitude	0.067 ± 0.046	1.034 ± 0.033
$f_0(980)$ Phase	0.049 ± 0.053	1.172 ± 0.038
χ_{c0} Magnitude	0.140 ± 0.047	1.057 ± 0.034
χ_{c0} Phase	0.040 ± 0.047	1.046 ± 0.034
non resonant Magnitude	0.525 ± 0.041	0.922 ± 0.029
non resonant Phase	0.111 ± 0.051	1.125 ± 0.036

calculation of these errors is described in Section 5.8.1.1.

5.4 Full Simulation Monte Carlo Tests

The next important test of the amplitude fit is to use full simulation Monte Carlo events for the signal. This tests whether the fit can successfully return the input parameters despite neglecting experimental resolution and mis-reconstruction effects. The signal events are generated flat in phase space and are subjected to the full reconstruction and event selection process as outlined in previous chapters.

The Monte Carlo truth information from each event is used to determine the true position of each event in the Dalitz plot. These true positions are used as input for the accept/reject algorithm used for generating the toy MC. If an event is accepted on the basis of its true Dalitz position then its reconstructed position is used in the amplitude fit. This method results in the correct mix of correctly and poorly reconstructed signal events and these signal events will also exhibit the correct acceptance distribution in the Dalitz plot.

Continuum and B-background toy events are generated and added into the fit. The number of events generated is a random number based on the Poisson distribution which has a mean corresponding to

$$\nu = f_{bg}\frac{N_{sig}}{f_{sig}} \tag{5.3}$$

where f_{bg} is either the continuum or B-background fraction that will be fixed in the amplitude fit and $f_{sig} = 1 - f_{q\overline{q}} - f_{B\overline{B}}$. In total 2287 events go into the amplitude fit, which is approximately the number expected in data. Table 5.3 shows the input and fitted values of the parameters, the difference between which corresponds to a χ^2/dof of 0.91. This indicates that the amplitude fit can successfully fit data which has acceptance effects.

Table 5.3: *Magnitude and Phase results of fit to full simulation MC with the six nominal components.*

	"Generated"	Fitted
$K_0^{*0}(1430)$ Magnitude	1.95	2.00 ± 0.15
$K_0^{*0}(1430)$ Phase	2.86	2.98 ± 0.13
$\rho^0(770)$ Magnitude	0.79	0.939 ± 0.097
$\rho^0(770)$ Phase	0.21	0.61 ± 0.40
$f_0(980)$ Magnitude	1.11	1.141 ± 0.095
$f_0(980)$ Phase	-0.92	-0.75 ± 0.44
χ_{c0} Magnitude	0.32	0.369 ± 0.059
χ_{c0} Phase	-0.45	-0.16 ± 0.31
Non Resonant Magnitude	0.69	0.58 ± 0.11
Non Resonant Phase	0.28	0.76 ± 0.46

5.5 Determination of Lineshape Parameters

In the nominal signal amplitude model two of the components are not modelled by relativistic Breit–Wigner lineshapes or simply as phase space. The $f_0(980)$ is modelled using the Flatté lineshape introduced in Section 1.3.2.2 and the $K_0^{*0}(1430)$ is modelled with the LASS parameterisation introduced in Section 1.3.5. Both of these models have parameters other than the mass and width of the resonance: the $g_{\pi/K}$ coupling constants in the case of the Flatté and the effective range and scattering length in the case of the LASS. These parameters have been measured by other experiments but the values found are in disagreement. Additionally, there is no *a priori* reason to expect that the LASS parameters will be the same in B decays as in $K\pi$ scattering. As such it was decided that rather than arbitrarily choosing a set of parameters from one experiment to use in this analysis, it should be determined which values of the parameters are favoured by the *BABAR* data.

It is not feasible to directly fit for these lineshape parameters because they form part of the integrals in Eq. (4.6) and as such these integrals would have to be recalculated for each iteration of the fit, which is computationally very expensive. Instead the approach is taken of *scanning* for the parameters. This involves performing fits where the parameters are set to various values in a given expected range and comparing the value of the minimised negative log likelihood (NLL) from these fits. In the region near the favoured value of the parameter the likelihood distribution becomes parabolic and so it is possible to find this favoured value and to estimate the error on the parameter from the method in Eq. (3.22).

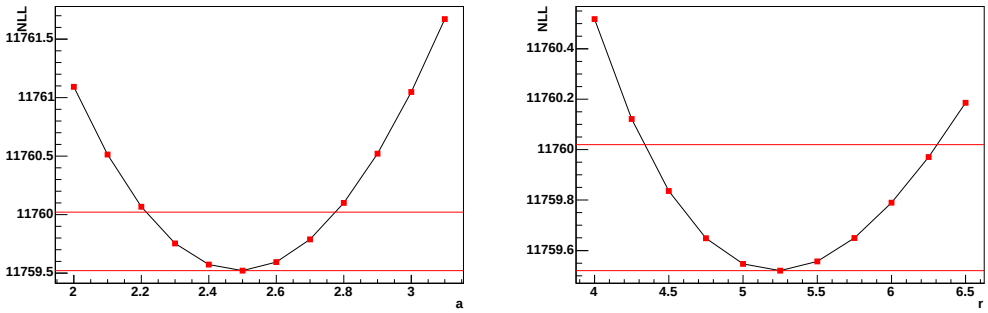

Figure 5.8: *Likelihood curves for the LASS parameter scans. The horizontal lines indicate the likelihood values of the minimum and half a unit from the minimum.*

The likelihood curves from the scans are shown in Figure 5.8 and Figure 5.9 and the values of the parameters that are used in the remainder of the analysis, along with the estimates of their errors, are shown in Table 5.4. For the $f_0(980)$ it was found that the pole mass in the Flatté function favoured a value of $965\,\mathrm{MeV}/c^2$. For the $K_0^{*0}(1430)$ the likelihood distribution was very flat in the space of the mass and width parameters and the PDG values were very close to the minimum. It was decided therefore to continue to use the PDG values.

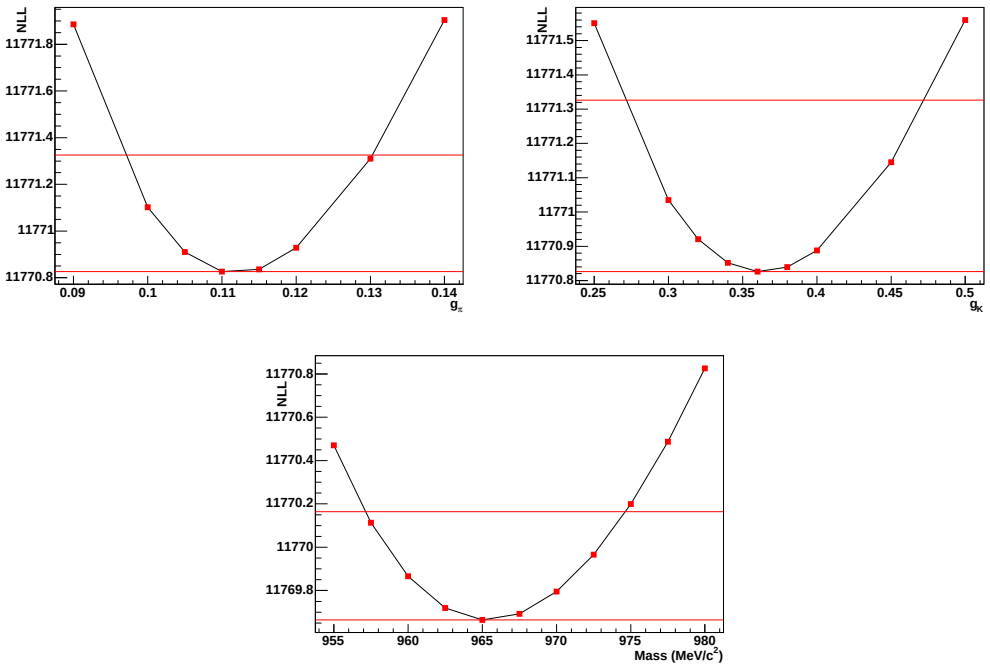

Figure 5.9: *Likelihood curves for the Flatté parameter scans. The horizontal lines indicate the likelihood values of the minimum and half a unit from the minimum.*

Table 5.4: *Results of the scans for the Flatté and LASS parameters. Also shown are the values from previous experiments.*

Parameter	Scan Result	Results from Other Experiments		
		[25]	[26]	[27]
g_π	0.11 ± 0.02	0.138 ± 0.010	$0.09 \pm 0.01 \pm 0.01$	0.28 ± 0.04
g_K	0.36 ± 0.10	0.614 ± 0.056	$0.02 \pm 0.04 \pm 0.03$	0.56 ± 0.18
Mass (GeV)	0.965 ± 0.010	0.970 ± 0.007	$0.977 \pm 0.003 \pm 0.002$	0.979 ± 0.004
		[30]	[30]	
a $(\mathrm{GeV}/c)^{-1}$	2.50 ± 0.30	1.95 ± 0.09	2.07 ± 0.10	—
r $(\mathrm{GeV}/c)^{-1}$	5.25 ± 1.05	1.76 ± 0.36	3.32 ± 0.34	—

5.6 Nominal Model Amplitude Fit Results

Now that the nominal signal amplitude model has been completed by the determination of the lineshape parameters it can be used to extract the fit fractions and phases of the components. Table 5.5 lists the fitted values of the fit fractions and phases for each component in both the B^+ and B^- data samples. Also given is the value of the average efficiency calculated according to Eq. (4.10).

The statistical errors on the phases are those returned by fit. The determination of the statistical errors on the fit fractions and the average efficiency is more complicated because they depend on the statistical errors of every fitted magnitude and phase. Due to the large correlations between these parameters and the complex dependence that the fit fractions and average efficiency have on them it is not feasible to directly calculate their errors. Instead a toy Monte Carlo approach is used. Five hundred toy experiments are performed exactly as those in Section 5.3 except that the input parameter values are those returned from the fit to data. For each toy experiment the fit fractions and average efficiency are calculated as they are for the data fit. The distributions of the fit fractions and average efficiency over the experiments is found to be well described by a Gaussian and the width of each Gaussian is taken to be the statistical error on the corresponding parameter. This technique is also used by the Belle collaboration in their analysis of this and other Dalitz plots [73]. It is very time consuming to perform such toy experiments and so this is only done for the nominal fit results. For the alternative model tests described in the follow section an approximate calculation is used to estimate the statistical errors. This calculation is found in almost all cases to be an overestimation. The systematic errors on all the parameters are calculated as described in Section 5.8.1.

The fit fraction asymmetries for each component are calculated according to Eq. (4.9) and can be found in Table 5.6. Again, the first error is statistical and the second is systematic. The statistical error is obtained by combining those of the fit fractions in Table 5.5. The calculation of the systematic error is described in Section 5.8.1.2.

Table 5.5: *Results of the nominal fit to data. The first error is statistical and the second is systematic.*

	B^+	B^-
Average Efficiency (%)	$15.957 \pm 0.054 \pm 0.079$	$15.922 \pm 0.051 \pm 0.079$
$K^{*0}(892)$ Fraction (%)	$12.5 \pm 1.4 \pm 0.5$	$14.0 \pm 1.5 \pm 0.6$
$K^{*0}(892)$ Phase	0.0 FIXED	0.0 FIXED
$K_0^{*0}(1430)$ Fraction (%)	$57.4 \pm 2.5 \pm 0.8$	$50.4 \pm 2.5 \pm 0.8$
$K_0^{*0}(1430)$ Phase	$3.08 \pm 0.12 \pm 0.03$	$2.73 \pm 0.13 \pm 0.03$
$\rho^0(770)$ Fraction (%)	$5.5 \pm 1.4 \pm 0.6$	$10.6 \pm 1.6 \pm 0.4$
$\rho^0(770)$ Phase	$1.12 \pm 0.49 \pm 0.14$	$-0.49 \pm 0.36 \pm 0.08$
$f_0(980)$ Fraction (%)	$13.2 \pm 1.9 \pm 0.5$	$15.9 \pm 2.1 \pm 0.4$
$f_0(980)$ Phase	$-0.87 \pm 0.45 \pm 0.10$	$-1.90 \pm 0.35 \pm 0.07$
χ_{c0} Fraction (%)	$1.29 \pm 0.51 \pm 0.13$	$0.90 \pm 0.43 \pm 0.09$
χ_{c0} Phase	$0.45 \pm 0.37 \pm 0.11$	$-0.81 \pm 0.39 \pm 0.11$
non resonant Fraction (%)	$4.0 \pm 1.6 \pm 0.9$	$3.5 \pm 1.3 \pm 0.9$
non resonant Phase	$1.33 \pm 0.32 \pm 0.06$	$0.87 \pm 0.38 \pm 0.09$

Histograms are created to illustrate the fit results in the projection variables $m_{K^\pm\pi^\mp}$ and $m_{\pi^\pm\pi^\mp}$. These histograms, like the ${}_s\mathcal{P}lots$ in Figure 5.2 have the requirement applied that the orthogonal invariant mass be greater than 2 GeV. These plots are shown in Figure 5.10 and Figure 5.11 for the B^+ and B^- samples respectively. The data are the black points with error bars, the lower solid red histogram is the $q\overline{q}$ component, the middle solid green histogram is the $B\overline{B}$ background contribution, while the upper blue histogram shows the total fit result. As well as the full spectrum plots, additional plots are constructed to show particular regions of the invariant mass spectra. These are shown in Figure 5.12 and Figure 5.13.

Table 5.6: *Fit fraction asymmetries calculated from the nominal results. The first error is statistical and the second is systematic.*

Component	Fit Fraction Asymmetry (%)
$K^{*0}(892)$	$5.7 \pm 7.7 \pm 5.7$
$K_0^{*0}(1430)$	$-6.5 \pm 3.3 \pm 2.0$
$\rho^0(770)$	$32 \pm 13 \pm 6$
$f_0(980)$	$9.3 \pm 9.7 \pm 2.6$
χ_{c0}	$-18 \pm 30 \pm 9$
Non Resonant	$-7 \pm 27 \pm 17$

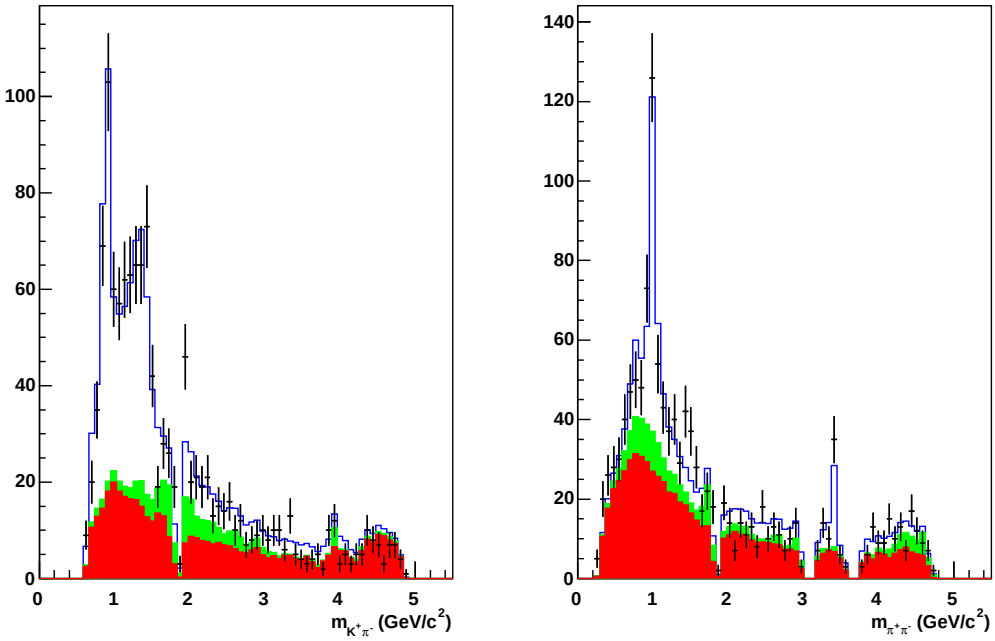

Figure 5.10: *Invariant mass projection plots for the nominal $B^+ \to K^+\pi^-\pi^+$ fit constructed as described in the text. The left plot shows the $K^+\pi^-$ mass spectrum and the right plot shows the $\pi^+\pi^-$ mass spectrum. All errors shown are statistical only. The large dips in the spectra correspond to the vetoes described in Section 4.3.3.*

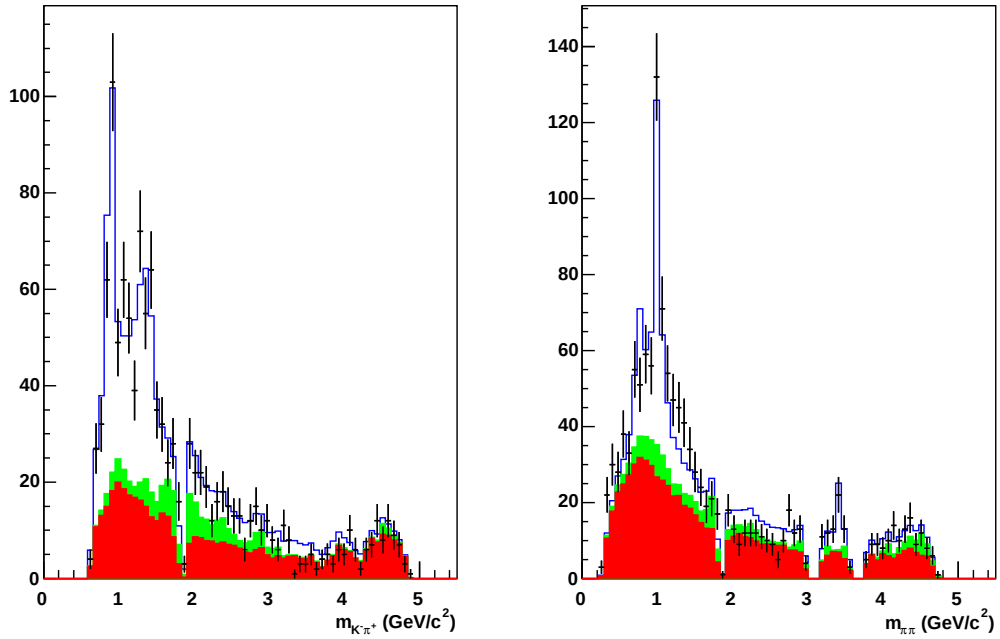

Figure 5.11: *Invariant mass projection plots for the nominal $B^- \to K^-\pi^+\pi^-$ fit constructed as described in the text. The left plot shows the $K^-\pi^+$ mass spectrum and the right plot shows the $\pi^-\pi^+$ mass spectrum. All errors shown are statistical only. The large dips in the spectra correspond to the vetoes described in Section 4.3.3.*

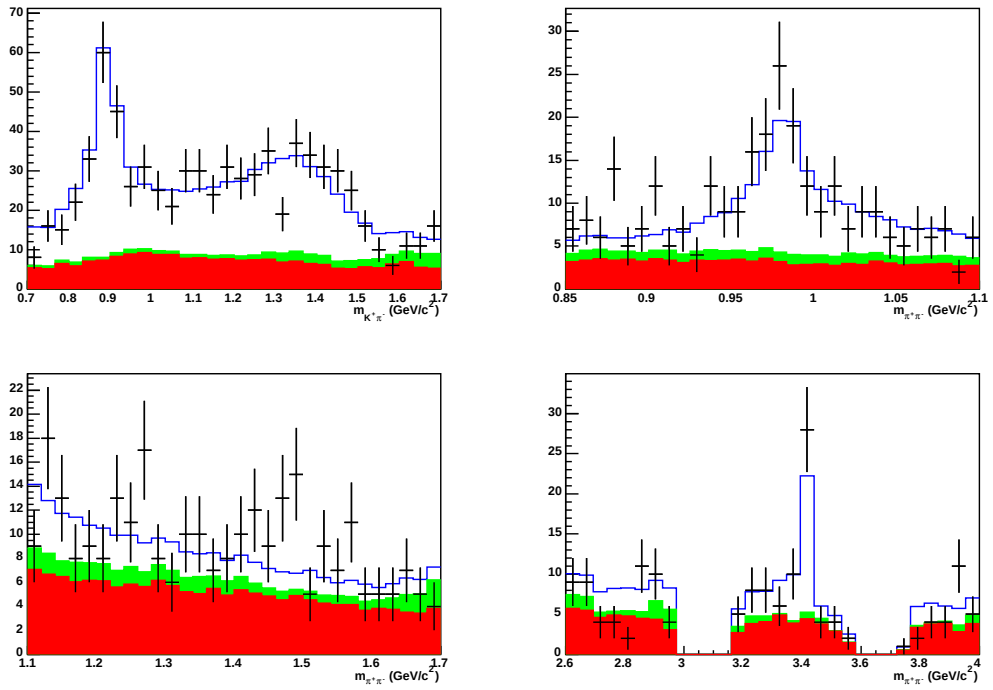

Figure 5.12: *Invariant mass regional plots for the nominal $B^+ \to K^+\pi^-\pi^+$ fit constructed as described in the text. The upper left plot shows the $K^+\pi^-$ mass spectrum in the region of the $K^{*0}(892)$ and $K_0^{*0}(1430)$; the upper right plot shows the $\pi^+\pi^-$ mass spectrum in the region of the $f_0(980)$; the lower left plot shows the $\pi^+\pi^-$ mass spectrum in the region of possible higher f resonances; and the lower right plot shows the $\pi^+\pi^-$ mass spectrum in the region of the χ_{c0}. All errors shown are statistical only. The large dips in the spectra correspond to the vetoes described in Section 4.3.3.*

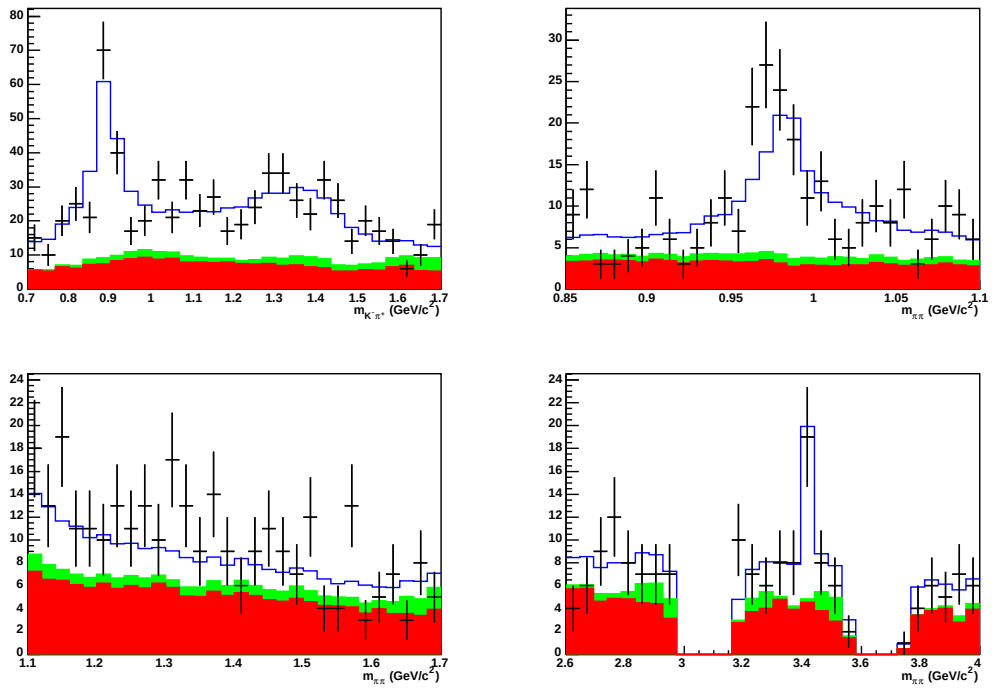

Figure 5.13: *Invariant mass regional plots for the nominal $B^- \to K^-\pi^+\pi^-$ fit constructed as described in the text. The upper left plot shows the $K^-\pi^+$ mass spectrum in the region of the $K^{*0}(892)$ and $K_0^{*0}(1430)$; the upper right plot shows the $\pi^-\pi^+$ mass spectrum in the region of the $f_0(980)$; the lower left plot shows the $\pi^-\pi^+$ mass spectrum in the region of possible higher f resonances; and the lower right plot shows the $\pi^-\pi^+$ mass spectrum in the region of the χ_{c0}. All errors shown are statistical only. The large dips in the spectra correspond to the vetoes described in Section 4.3.3.*

5.7 Alternative Model Amplitude Fits

The results presented in the previous section were for the nominal signal model, which was chosen based on the results of previous analyses and examination of the invariant mass spectra shown in Figure 5.2. Such an approach is necessary because including too many components could lead to instability in the fit and inflation of the statistical errors. However, it could be that contributions have been omitted or included erroneously. This section describes the tests of alternative models of the dynamics of the Dalitz plot.

In order to compare the different models an estimate of the goodness of fit is calculated from 2D histograms of the Dalitz plot. These are constructed from the data and from toy Monte Carlo events that are generated from the fit results but with 100× the statistics. The histograms are used to compute a χ^2 value for the fit according to:

$$\chi^2 = \sum_{i=1}^{N_{\rm bins}} \frac{[y_i - f(x_i)]^2}{f(x_i)} \tag{5.4}$$

where y_i is the number of events in bin i and $f(x_i)$ is the number of events in that bin according to the fitted likelihood function. The associated number of degrees of freedom is defined as $N_{\rm bins} - k - 1$, where k is the number of free parameters in the Dalitz plot likelihood function. In the calculation of the χ^2 bins with fewer than 10 entries are combined with neighbouring bins until they have greater than 10 entries. If after combining with their neighbours they still have fewer than 10 entries they are excluded from the χ^2 calculation. As was shown in Figure 5.4 there are very few events in the centre of the Dalitz plot and as such the contribution to the χ^2 comes almost entirely from the bands close to the axes. The χ^2 calculated from the nominal fit shown as a function of Dalitz position can be seen in Figure 5.14 for the positive sample and in Figure 5.15 for the negative sample.[1]

[1]The χ^2 values shown in Table 5.7–Table 5.10 have subsequently been found to be incorrect due to a bug in the calculation code. The correct values will be included in the official *BABAR* publication of this analysis.

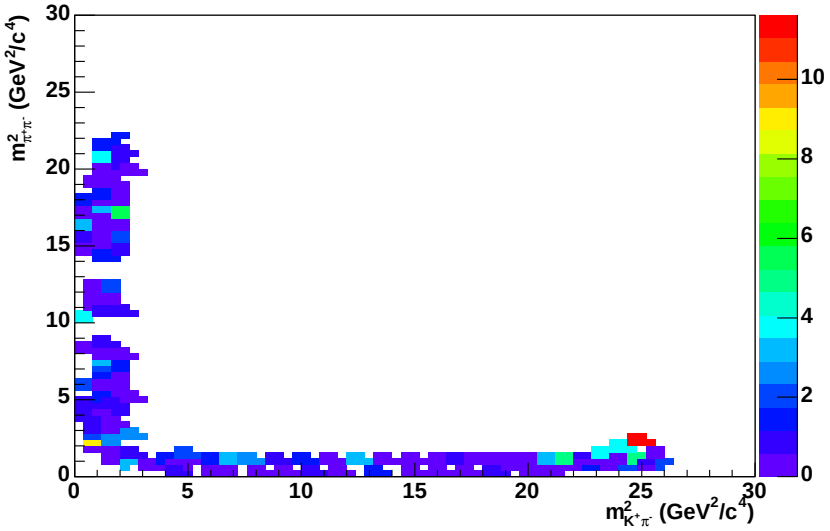

Figure 5.14: *Nominal fit χ^2 as a function of Dalitz position for the positive sample.*

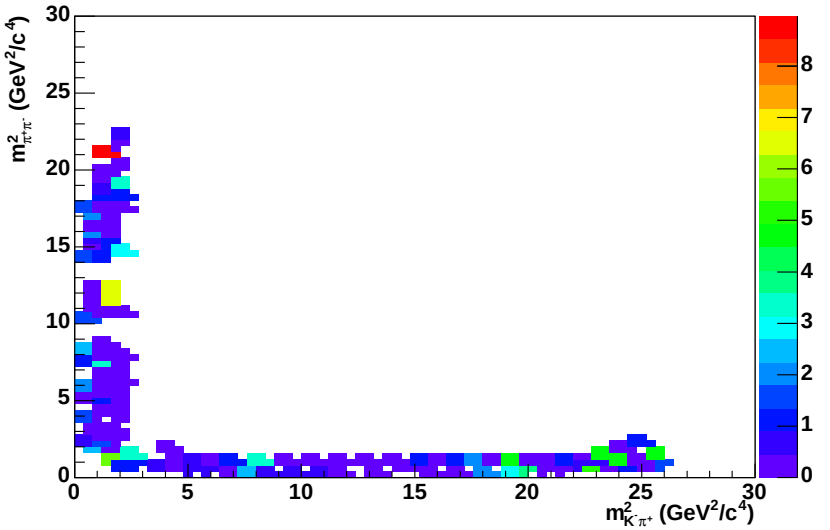

Figure 5.15: *Nominal fit χ^2 as a function of Dalitz position for the negative sample.*

5.7.1 Omission Tests

In order to test whether a component of the nominal fit model has been correctly included tests are performed where each component is removed, in turn, from the fit model. In each test the fit is performed as in the nominal case and the values of the parameters and the negative log likelihood can be compared. The results of these tests are shown in Table 5.7 for the B^+ data sample and Table 5.8 for B^- sample.

5.7.2 Addition Tests

Models are also tested adding each of the possible contributions listed in Section 4.7.2 in turn to the nominal model. Again the values of the parameters and negative log likelihood can be compared in order to gauge whether an added component is significant. Upper limits are calculated for each component that does not have a significant fit fraction in both B^+ and B^- samples using the following:

$$\frac{\int_0^x \mathcal{L}\, dx}{\int_0^\infty \mathcal{L}\, dx} = 0.90 \tag{5.5}$$

where x is the value of the fit fraction 90% confidence level upper limit. This is based on Bayesian statistics with a uniform prior. These upper limits are presented in Table 6.1.

Table 5.7: *Results of fit to B^+ data with a different component omitted in turn from the nominal fit.*

	Nominal	No $K^{*0}(892)$	No $K_0^{*0}(1430)$	No $\rho^0(770)$	No $f_0(980)$	No χ_{c0}	No non resonant
$(-\ln\mathcal{L}) - (-\ln\mathcal{L}(\text{nominal}))$	—	101.2	250.4	19.7	106.3	21.9	20.3
2D χ^2	193/117	226/119	495/119	234/119	275/119	197/119	216/119
$K^{*0}(892)$ Fraction (%)	12.5 ± 1.4	—	26.3 ± 2.7	12.8 ± 2.2	13.4 ± 1.7	12.6 ± 2.3	12.7 ± 1.9
$K^{*0}(892)$ Phase	0.0 FIXED	—	0.0 FIXED	0.0 FIXED	0.0 FIXED	0.0 FIXED	0.0 FIXED
$K_0^{*0}(1430)$ Fraction (%)	57.4 ± 2.5	71.1 ± 12.6	—	61.1 ± 4.4	63.8 ± 4.0	57.5 ± 4.3	59.8 ± 3.1
$K_0^{*0}(1430)$ Phase	3.08 ± 0.12	2.78 ± 0.39	—	3.08 ± 0.13	-3.12 ± 0.12	3.12 ± 0.12	2.98 ± 0.12
$\rho^0(770)$ Fraction (%)	5.5 ± 1.4	5.7 ± 1.4	9.0 ± 2.0	—	10.2 ± 2.2	5.3 ± 1.5	6.4 ± 1.6
$\rho^0(770)$ Phase	1.12 ± 0.49	1.01 ± 0.23	1.71 ± 0.24	—	2.73 ± 0.36	1.38 ± 0.46	0.04 ± 0.37
$f_0(980)$ Fraction (%)	13.2 ± 1.9	13.1 ± 1.6	27.3 ± 3.0	14.0 ± 2.4	—	12.3 ± 2.2	17.8 ± 2.7
$f_0(980)$ Phase	-0.87 ± 0.45	-0.87 FIXED	0.01 ± 0.19	-0.36 ± 0.38	—	-0.61 ± 0.42	-1.85 ± 0.31
χ_{c0} Fraction (%)	1.29 ± 0.51	1.28 ± 0.40	1.30 ± 0.46	1.30 ± 0.45	1.07 ± 0.41	—	2.01 ± 0.54
χ_{c0} Phase	0.45 ± 0.37	0.44 ± 0.50	-2.67 ± 0.35	0.51 ± 0.38	0.90 ± 0.40	—	0.20 ± 0.34
non resonant Fraction (%)	4.0 ± 1.6	5.2 ± 1.6	44.4 ± 3.7	5.5 ± 1.7	12.8 ± 2.8	6.0 ± 1.7	—
non resonant Phase	1.33 ± 0.32	1.69 ± 0.47	-1.82 ± 0.15	1.35 ± 0.30	1.92 ± 0.23	1.40 ± 0.29	—

Table 5.8: *Results of fit to B^- data with a different component omitted in turn from the nominal fit.*

	Nominal	No $K^{*0}(892)$	No $K_0^{*0}(1430)$	No $\rho^0(770)$	No $f_0(980)$	No χ_{c0}	No non resonant
$(-\ln\mathcal{L}) - (-\ln\mathcal{L}(\text{nominal}))$	—	130.1	185.2	45.0	134.5	16.4	22.5
2D χ^2	205/121	255/123	444/123	297/123	328/123	208/123	225/123
$K^{*0}(892)$ Fraction (%)	14.0 ± 1.5	—	24.6 ± 2.7	14.8 ± 2.2	15.2 ± 1.9	13.8 ± 2.2	14.5 ± 2.0
$K^{*0}(892)$ Phase	0.0 FIXED	—	0.0 FIXED	0.0 FIXED	0.0 FIXED	0.0 FIXED	0.0 FIXED
$K_0^{*0}(1430)$ Fraction (%)	50.4 ± 2.5	64.2 ± 3.5	—	55.0 ± 4.2	53.5 ± 4.1	50.6 ± 4.0	53.3 ± 3.2
$K_0^{*0}(1430)$ Phase	2.73 ± 0.13	2.25 ± 0.27	—	2.73 ± 0.13	2.76 ± 0.15	2.74 ± 0.13	2.66 ± 0.12
$\rho^0(770)$ Fraction (%)	10.6 ± 1.6	11.0 ± 1.6	15.7 ± 2.4	—	15.7 ± 2.5	10.5 ± 2.0	11.5 ± 2.2
$\rho^0(770)$ Phase	-0.49 ± 0.36	-0.45 ± 0.20	1.32 ± 0.25	—	0.93 ± 0.89	-0.37 ± 0.36	-0.96 ± 0.33
$f_0(980)$ Fraction (%)	15.9 ± 2.1	15.9 ± 1.7	24.5 ± 2.7	17.3 ± 2.5	—	15.6 ± 2.4	19.2 ± 2.6
$f_0(980)$ Phase	-1.90 ± 0.35	-1.90 FIXED	0.21 ± 0.22	-0.92 ± 0.37	—	-1.80 ± 0.35	-2.28 ± 0.29
χ_{c0} Fraction (%)	0.90 ± 0.43	0.87 ± 0.35	0.98 ± 0.39	0.87 ± 0.36	0.72 ± 0.33	—	1.51 ± 0.46
χ_{c0} Phase	-0.81 ± 0.39	-0.96 ± 0.47	2.86 ± 0.42	-0.72 ± 0.40	-0.67 ± 0.46	—	-1.04 ± 0.34
non resonant Fraction (%)	3.5 ± 1.3	5.8 ± 1.7	32.6 ± 3.2	6.0 ± 1.6	10.1 ± 2.1	4.8 ± 1.3	—
non resonant Phase	0.87 ± 0.38	1.23 ± 0.33	-2.27 ± 0.19	0.83 ± 0.35	0.74 ± 0.55	1.01 ± 0.35	—

Table 5.9: *Results of fit to B^+ data with a different resonance added in turn to the nominal fit. The values for the "Additional Fraction" and "Additional Phase" refer to the component named at the top of the column.*

	Nominal	With $f_2(1270)$	With $f_0(1370)$	With $\rho^0(1450)$	With $f_0(1500)$	With $f_2'(1525)$	With $K_2^{*0}(1430)$	With $K^{*0}(1680)$
$(-\ln\mathcal{L}) - (-\ln\mathcal{L}(\text{nominal}))$	—	-15.0	-4.2	-18.2	-4.9	-3.9	-1.8	-0.5
2D χ^2	193/117	168/115	188/115	181/115	190/115	180/115	193/115	195/115
$K^{*0}(892)$ Fraction (%)	12.5 ± 1.4	11.5 ± 2.3	12.3 ± 2.8	11.4 ± 2.3	12.5 ± 2.6	11.9 ± 2.4	13.0 ± 2.6	12.8 ± 2.7
$K_0^{*0}(1430)$ Fraction (%)	57.4 ± 2.5	55.4 ± 9.8	56.6 ± 9.8	56.3 ± 10.0	56.6 ± 9.8	56.4 ± 9.8	54.8 ± 9.6	57.6 ± 10.0
$K_0^{*0}(1430)$ Phase	3.08 ± 0.12	3.11 ± 0.12	3.07 ± 0.12	3.12 ± 0.13	3.10 ± 0.13	3.10 ± 0.13	3.09 ± 0.12	3.10 ± 0.13
$\rho^0(770)$ Fraction (%)	5.5 ± 1.4	4.3 ± 1.5	4.8 ± 1.5	5.5 ± 1.9	5.2 ± 1.6	5.1 ± 1.6	5.3 ± 1.6	5.5 ± 1.6
$\rho^0(770)$ Phase	1.12 ± 0.49	1.17 ± 0.41	1.29 ± 0.43	1.94 ± 0.38	1.34 ± 0.45	1.36 ± 0.46	1.70 ± 0.50	1.22 ± 0.46
$f_0(980)$ Fraction (%)	13.2 ± 1.9	13.4 ± 2.8	10.7 ± 2.3	11.8 ± 2.4	11.5 ± 2.4	12.9 ± 2.6	12.6 ± 2.5	12.8 ± 2.7
$f_0(980)$ Phase	-0.87 ± 0.45	-0.77 ± 0.37	-0.53 ± 0.41	0.47 ± 0.37	-0.60 ± 0.43	-0.58 ± 0.44	-0.36 ± 0.46	-0.78 ± 0.42
χ_{c0} Fraction (%)	1.29 ± 0.51	1.27 ± 0.45	1.35 ± 0.46	1.28 ± 0.45	1.31 ± 0.46	1.29 ± 0.45	1.25 ± 0.44	1.29 ± 0.45
χ_{c0} Phase	0.45 ± 0.37	0.41 ± 0.37	0.40 ± 0.37	0.53 ± 0.39	0.44 ± 0.37	0.47 ± 0.38	0.52 ± 0.38	0.43 ± 0.37
non resonant Fraction (%)	4.0 ± 1.6	3.7 ± 1.3	3.6 ± 1.5	5.0 ± 1.8	4.4 ± 1.6	3.9 ± 1.5	5.4 ± 2.0	4.1 ± 1.5
non resonant Phase	1.33 ± 0.32	1.25 ± 0.32	1.14 ± 0.33	1.53 ± 0.29	1.21 ± 0.32	1.39 ± 0.32	1.57 ± 0.31	1.30 ± 0.31
Additional Fraction (%)	—	4.8 ± 1.8	1.18 ± 0.80	10.1 ± 2.7	0.97 ± 0.60	2.8 ± 1.1	2.3 ± 1.6	0.27 ± 0.54
Additional Phase	—	-0.11 ± 0.26	-0.25 ± 0.50	-0.32 ± 0.29	0.83 ± 0.50	0.19 ± 0.38	-0.20 ± 0.21	-1.11 ± 0.80

Table 5.10: *Results of fit to B^- data with a different resonance added in turn to the nominal fit. The values for the "Additional Fraction" and "Additional Phase" refer to the component named at the top of the column.*

	Nominal	With $f_2(1270)$	With $f_0(1370)$	With $\rho^0(1450)$	With $f_0(1500)$	With $f_2'(1525)$	With $K_2^{*0}(1430)$	With $K^{*0}(1680)$
$(-\ln\mathcal{L}) - (-\ln\mathcal{L}(\text{nominal}))$	—	-7.9	-7.9	-2.5	-4.7	-0.4	-4.9	-1.0
2D χ^2	205/121	204/119	202/119	203/119	203/119	205/119	200/119	206/119
$K^{*0}(892)$ Fraction (%)	14.0 ± 1.5	12.7 ± 2.4	13.8 ± 3.2	13.6 ± 2.4	14.0 ± 2.6	14.0 ± 2.4	13.6 ± 2.4	14.3 ± 2.5
$K_0^{*0}(1430)$ Fraction (%)	50.4 ± 2.5	47.8 ± 7.7	48.9 ± 7.9	48.7 ± 7.7	49.6 ± 7.9	50.6 ± 8.0	47.3 ± 7.7	50.4 ± 8.1
$K_0^{*0}(1430)$ Phase	2.73 ± 0.13	2.83 ± 0.13	2.73 ± 0.13	2.76 ± 0.13	2.73 ± 0.13	2.73 ± 0.13	2.77 ± 0.13	2.78 ± 0.13
$\rho^0(770)$ Fraction (%)	10.6 ± 1.6	8.0 ± 2.0	10.6 ± 2.2	9.5 ± 2.0	10.8 ± 2.2	10.6 ± 2.2	10.5 ± 2.2	10.4 ± 2.2
$\rho^0(770)$ Phase	-0.49 ± 0.36	0.09 ± 0.37	-0.45 ± 0.38	-0.63 ± 0.41	-0.48 ± 0.36	-0.49 ± 0.37	-0.45 ± 0.31	-0.45 ± 0.36
$f_0(980)$ Fraction (%)	15.9 ± 2.1	14.6 ± 2.7	13.9 ± 3.1	16.0 ± 2.8	15.5 ± 2.9	15.8 ± 2.8	16.0 ± 2.8	15.7 ± 2.8
$f_0(980)$ Phase	-1.90 ± 0.35	-1.21 ± 0.35	-2.04 ± 0.40	-2.15 ± 0.38	-1.95 ± 0.35	-1.90 ± 0.35	-1.91 ± 0.33	-1.94 ± 0.35
χ_{c0} Fraction (%)	0.90 ± 0.43	0.94 ± 0.37	0.96 ± 0.37	0.94 ± 0.37	0.92 ± 0.36	0.90 ± 0.36	0.89 ± 0.36	0.93 ± 0.37
χ_{c0} Phase	-0.81 ± 0.39	-0.79 ± 0.38	-0.85 ± 0.38	-0.82 ± 0.38	-0.82 ± 0.39	-0.81 ± 0.39	-0.56 ± 0.41	-0.81 ± 0.39
non resonant Fraction (%)	3.5 ± 1.3	3.2 ± 1.1	3.6 ± 1.3	3.0 ± 1.0	3.8 ± 1.2	3.5 ± 1.2	4.0 ± 1.5	3.4 ± 1.1
non resonant Phase	0.87 ± 0.38	0.79 ± 0.39	0.63 ± 0.40	0.87 ± 0.39	0.79 ± 0.39	0.87 ± 0.39	1.25 ± 0.38	0.82 ± 0.40
Additional Fraction (%)	—	8.3 ± 2.5	2.3 ± 1.3	1.6 ± 1.2	1.7 ± 1.8	0.12 ± 0.28	4.9 ± 2.1	0.52 ± 0.76
Additional Phase	—	-0.68 ± 0.28	0.22 ± 0.41	0.57 ± 0.44	1.11 ± 0.63	-1.7 ± 1.2	2.63 ± 0.17	-2.22 ± 0.62

5.8 Systematic Uncertainties

This section describes the methods by which the systematic uncertainties on each of the results presented in this chapter have been estimated. The order of examination of these sources of uncertainty necessarily does not follow the order in which the results were presented due to the complex inter-relation of the quantities involved.

5.8.1 Amplitude Fit Uncertainties

There are several potential sources of systematic uncertainty in the amplitude fit, each of which give rise to uncertainties on the fit fractions, phases and the average efficiency (Eq. (4.10)):

- $f_{q\overline{q}}$ - the continuum background fraction
- $f_{B\overline{B}}$ - the $B\overline{B}$ background fraction
- $Q(m^2_{K^+\pi^-}, m^2_{\pi^+\pi^-})$ - the distribution of the continuum background
- $B(m^2_{K^+\pi^-}, m^2_{\pi^+\pi^-})$ - the distribution of the $B\overline{B}$ background
- $\epsilon(m^2_{K^+\pi^-}, m^2_{\pi^+\pi^-})$ - the reconstruction efficiency as a function of Dalitz plot position

The first two of these sources are simple numbers, each with an associated error (Table 5.1). The latter three sources are due to the shape of the two-dimensional histograms that are used in the amplitude fit. Since histograms do not have an intrinsic error these sources are more difficult to quantify. So use is made of the fact that each of the bins in the histograms do have an error, either Poisson in the case of the background histograms or binomial in the case of the efficiency histograms.

It is possible therefore to estimate the uncertainty due to the distributions by creating new histograms where the value in each bin has been replaced. The new bin

value is the result of a random number generation based on the Gaussian distribution centred on the original value and using the bin error as its width. Similarly new values of the background fractions can be generated. For each source of uncertainty, 200 new values/distributions are constructed and the amplitude fit is re-performed for each new value/distribution. The systematic uncertainties on the fit fractions, phases and average efficiency are taken to be the width of the Gaussian distribution of the parameters over these 200 tests. Table 5.11 lists the absolute systematic uncertainties due to each of the above sources, as well as the total (taken as the quadrature sum), for each of the nominal fit components and the average efficiency.

5.8.1.1 Fit Bias

Since some of the fit fractions and phases were identified in Section 5.3.2 to suffer from fit bias it is necessary to add a further systematic error to account for this bias. This systematic is calculated from the sets of toy experiments performed primarily to calculate the statistical error on the fit fractions (Section 5.6). The statistical error was taken to be the width of the distribution of the given fit fraction in the 500 experiments. The fit bias systematic error can be taken to be the residual of the mean of the distribution and the value of the given fit fraction or phase returned by the nominal fit, as illustrated in Figure 5.16 for the χ_{c0} fit fraction in the positive data sample.

The systematic errors quoted in Table 5.5 are the quadrature combination of the uncertainties in Table 5.11 and the uncertainty due to fit bias.

5.8.1.2 Fit Fraction Asymmetries

For the fit fraction asymmetries the effects of the fit bias systematics will cancel as will those from the background and efficiency distribution uncertainties, leaving only the effects from the background fraction uncertainties. In addition there is a further contribution from possible detector charge bias, which has been estimated

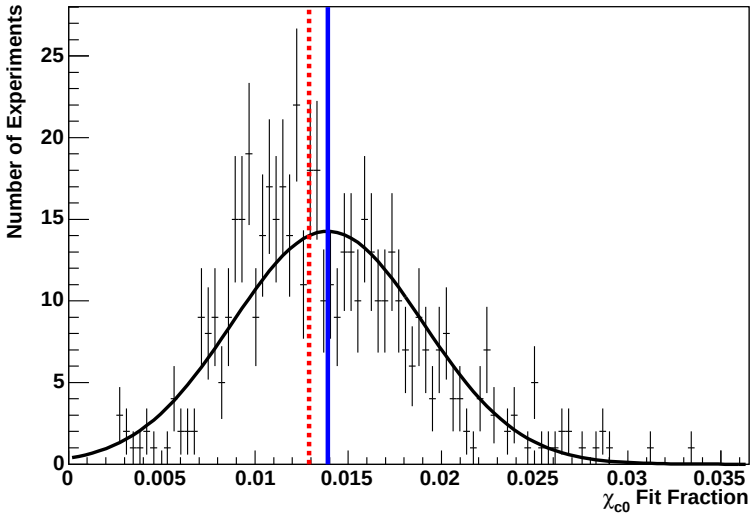

Figure 5.16: *Determination of the fit bias on the χ_{c0} fit fraction in the positive data sample. The points are the toy experiments and the solid black curve is the Gaussian fit to the points. The solid blue vertical line is the mean of the Gaussian and the dashed red vertical line is the value returned by the nominal fit.*

in previous studies to be 2% [64].

Table 5.11: *Systematic uncertainties from the amplitude fit.*

Uncertainty Source	$B\overline{B}$ Fraction		$B\overline{B}$ Histogram		$q\overline{q}$ Fraction		$q\overline{q}$ Histogram		ϵ Histogram		Total	
Data Sample	B^+	B^-	B^+	B^-	B^+	B^-	B^+	B^-	B^+	B^-	B^+	B^-
Average Efficiency	0.001	0.002	0.005	0.006	0.003	0.003	0.007	0.006	0.078	0.078	0.079	0.079
$K^{*0}(892)$ Fit Fraction	0.168	0.188	0.068	0.143	0.295	0.361	0.116	0.122	0.357	0.305	0.511	0.542
$K_0^{*0}(1430)$ Fit Fraction	0.101	0.032	0.328	0.280	0.197	0.022	0.348	0.370	0.333	0.276	0.623	0.541
$K_0^{*0}(1430)$ Phase	0.001	0.000	0.011	0.020	0.001	0.000	0.016	0.021	0.018	0.017	0.027	0.034
$\rho^0(770)$ Fit Fraction	0.096	0.069	0.320	0.168	0.234	0.184	0.227	0.258	0.117	0.180	0.481	0.407
$\rho^0(770)$ Phase	0.012	0.001	0.089	0.035	0.045	0.030	0.065	0.055	0.040	0.028	0.126	0.077
$f_0(980)$ Fit Fraction	0.046	0.047	0.212	0.175	0.120	0.118	0.259	0.244	0.157	0.165	0.391	0.365
$f_0(980)$ Phase	0.007	0.003	0.061	0.035	0.027	0.014	0.065	0.049	0.035	0.027	0.100	0.068
χ_{c0} Fit Fraction	0.029	0.025	0.021	0.013	0.045	0.041	0.051	0.029	0.020	0.017	0.079	0.060
χ_{c0} Phase	0.005	0.010	0.028	0.032	0.015	0.016	0.050	0.062	0.026	0.027	0.065	0.077
Non Resonant Fit Fraction	0.175	0.159	0.186	0.140	0.303	0.235	0.286	0.210	0.080	0.054	0.495	0.384
Non Resonant Phase	0.007	0.020	0.039	0.050	0.012	0.017	0.041	0.058	0.024	0.030	0.063	0.086

5.8.2 Branching Fraction Uncertainties

The sources of systematic uncertainty on the total branching fraction can be seen from its equation, Eq. (5.1):

$$\mathcal{B}(B^{\pm} \to K^{\pm}\pi^{\mp}\pi^{\pm}) = \frac{N_{sig}}{\bar{\epsilon}\,\epsilon_c\,N_{B\overline{B}}}$$

Each of the variables on the right hand side is a source of systematic uncertainty.

N_{sig} has an uncertainty due to the fixed $B\overline{B}$ background component in the $m_{\rm ES}$ fit. This is evaluated by performing the $m_{\rm ES}$ fit again with the $B\overline{B}$ component fixed to its nominal value plus its error and again with the error subtracted from the nominal value. The difference in the signal yield in each case is taken to be the systematic error (0.4%). $\bar{\epsilon}$ has three contributions, one from its statistical uncertainty from the amplitude fit, which is evaluated from the toy MC experiments described in Section 5.6. The second contribution is from the systematic uncertainties from Table 5.11 and the third is from the corrections due to PID and tracking, which are evaluated by their respective task force within the *BABAR* collaboration. Studies using control channels find the systematic errors to be 4.2% and 2.4% respectively for PID and tracking. The calculation of $N_{B\overline{B}}$ has statistical and systematic uncertainties due to each of the parameters in Eq. (3.1). These are calculated centrally within the collaboration and the total is found to be 1.1% [47]. The efficiency corrections, ϵ_c, due to the selection requirements on $\cos\theta_T$, the Fisher discriminant, ΔE and $m_{\rm ES}$ also have an associated systematic uncertainty. It is necessary first to describe the method by which these corrections are calculated.

5.8.2.1 Efficiency Corrections

The calculation of the selection requirement efficiency corrections makes use of the control channel $B^+ \to \overline{D}^0\pi^+$; $\overline{D}^0 \to K^+\pi^-$, which has the same final state as the signal mode but has a much larger branching fraction $(189 \pm 12) \times 10^{-6}$ [2]. For each of the selection requirements signal sets of Monte Carlo and data are subjected to all

requirements up to *but not including* the one in question (plus a requirement on the D^0 mass) to form one sample of events. A second sample is produced by applying all requirements up to *and including* the one under consideration (plus the same requirement on the D^0 mass). Since the Monte Carlo is signal only the efficiency of the requirement is simply the number of events in the second sample divided by the number in the first sample. For the data it is necessary to perform and fit to $m_{\rm ES}$ in order to extract the number of signal events in each sample before forming the ratio. Comparison of these two efficiencies gives the efficiency correction and the systematic error is given by propagating the Poisson errors on the number of events in the data and MC samples. The values of the corrections and their accompanying errors are given in Table 5.12.

5.8.2.2 Partial Branching Fractions

The partial branching fractions are formed by multiplying the fit fractions by the total branching fraction and are thus an indication of the branching fraction for a given mode were it the only mode present in the Dalitz plot. They are presented in Chapter 6 so that comparison can be made with previous measurements and theoretical predictions. The systematic uncertainty on these quantities is formed by combining in quadrature the systematic uncertainties on the fit fractions and all the contributions to the systematic on the total branching fraction other than that due to the fixed $B\overline{B}$ background component in the $m_{\rm ES}$ fit because this has already been considered in the fit fraction systematics.

5.8.2.3 Total Asymmetry

The total asymmetry systematic error has a contribution (as with the fit fraction asymmetries) from the possible detector charge bias, estimated at around 2%. The only other contribution is from the possible asymmetry in the $B\overline{B}$ background. As mention earlier in this section, the $m_{\rm ES}$ fit was re-performed several times with

the number of $B\overline{B}$ background events varied up and down by its error in order to estimate the effect on the total branching fraction. This was done also for the charge separated samples and using each combination of the possible signal yields from these fits to recalculate the asymmetry it is possible to estimate the systematic error on the asymmetry from this source.

Table 5.12: *Selection requirement efficiency corrections.*

Requirement	Data Before	Data After	Data Efficiency	MC Before	MC After	MC Efficiency	Correction	Error	Fractional Error
$\cos\theta_T$	15797	10744	0.680	76770	53322	0.695	0.979	0.026	0.027
Fisher	10744	7641	0.711	53322	38385	0.720	0.988	0.029	0.030
$m_{\rm ES}$	7641	7609	0.996	38385	38376	1.000	0.996	0.016	0.016
ΔE	7609	6327	0.831	38376	34850	0.908	0.916	0.023	0.025
Total							0.882	0.048	0.050

6

Discussion and Conclusion

6.1 Introduction

This chapter will summarise the results of the analysis and make comparisons with previous measurements and theoretical predictions. The implications of the results for the structure of the light meson spectrum and for factorisation models will be discussed. Finally some ideas for improvements to future iterations of the analysis will be presented.

Table 6.1: *Summary of branching fraction and A_{CP} results. The first error is statistical and the second is systematic.*

Mode	$\mathcal{B}(B^+ \to \text{Mode}) \times 10^6$	90% CL UL $\times 10^6$	A_{CP} (%)
$K^+\pi^-\pi^+$ Total	$64.4 \pm 2.5 \pm 4.6$	–	$-0.5 \pm 3.9 \pm 2.1$
$K^{*0}(892)\pi^+$; $K^{*0}(892) \to K^+\pi^-$	$8.53 \pm 0.74 \pm 0.50$	–	$5.7 \pm 7.7 \pm 5.7$
$K_0^{*0}(1430)\pi^+$; $K_0^{*0}(1430) \to K^+\pi^-$	$34.7 \pm 1.8 \pm 1.8$	–	$-6.5 \pm 3.3 \pm 2.0$
$\rho^0(770)K^+$; $\rho^0(770) \to \pi^+\pi^-$	$5.17 \pm 0.80 \pm 0.39$	–	$32 \pm 13 \pm 6$
$f_0(980)K^+$; $f_0(980) \to \pi^+\pi^-$	$9.36 \pm 0.98 \pm 0.51$	–	$9.3 \pm 9.7 \pm 2.6$
$\chi_{c0}K^+$; $\chi_{c0} \to \pi^+\pi^-$	$0.71 \pm 0.22 \pm 0.06$	< 2.3	–
$K^+\pi^-\pi^+$ non resonant	$2.42 \pm 0.67 \pm 0.42$	< 8.8	–
$K_2^{*0}(1430)\pi^+$; $K_2^{*0}(1430) \to K^+\pi^-$	–	< 6.3	–
$K^{*0}(1680)\pi^+$; $K^{*0}(1680) \to K^+\pi^-$	–	< 2.0	–
$f_2(1270)K^+$; $f_2(1270) \to \pi^+\pi^-$	–	< 7.4	–
$f_0(1370)K^+$; $f_0(1370) \to \pi^+\pi^-$	–	< 8.5	–
$\rho^0(1450)K^+$; $\rho^0(1450) \to \pi^+\pi^-$	–	< 7.6	–
$f_0(1500)K^+$; $f_0(1500) \to \pi^+\pi^-$	–	< 5.2	–
$f_2'(1525)K^+$; $f_2'(1525) \to \pi^+\pi^-$	–	< 3.1	–

6.2 Summary of Results

The fit fractions and phases from the nominal fit have been shown in Table 5.5. In order to make comparisons with previous measurements and predictions from factorisation theory it is necessary to convert the fit fractions into branching fractions. This is achieved by multiplying each fit fraction by the total branching fraction to give an estimate of the branching fraction of the mode. These branching fractions from each of the charge separated fits are then averaged. For components that do not have statistically significant branching fractions 90% confidence level upper limits are determined. Upper limits are also calculated for the components added in the addition tests described in Section 5.7.2. The branching fractions and *CP* asymmetries are summarised in Table 6.1. It is worth reiterating that the values measured

for the $K_0^{*0}(1430)$ component are not solely due to this resonance but also include the effective range part of the LASS amplitude. From these results the following points can be raised:

- ◇ The total $B^+ \to K^+\pi^-\pi^+$ branching fraction has been measured with increased accuracy and is compatible with previous *BABAR* measurements. It continues to differ from Belle's measurement of $(46.6 \pm 2.1 \pm 4.3) \times 10^{-6}$ [73], which although not containing the contribution from $\chi_{c0}K^+$ is still significantly smaller. One difference between the two analyses is that Belle do not apply corrections to the signal reconstruction efficiency due to observed differences between data and MC but simply include the systematic error. This difference is not sufficient to fully explain the discrepancy between the two values.

- ◇ The total charge asymmetry has been measured to be consistent with zero to a higher degree of accuracy than previous measurements.

- ◇ The $B^+ \to K^{*0}(892)\pi^+$ branching fraction[1], $(12.8 \pm 1.1 \pm 0.7) \times 10^{-6}$, is smaller than that measured in previous analyses that do not perform an amplitude fit to the Dalitz plot [1, 74]. However, it is slightly larger but consistent with the value reported by Belle in their amplitude analysis [73]. The value measured here is larger than all the factorisation theory predictions in Table 1.3.

- ◇ The branching fraction measurement of $B^+ \to \rho^0(770)K^+$ is the first measurement of the mode from *BABAR* and is highly consistent with that from the Belle collaboration in their recent amplitude analysis [73] and has a slightly improved accuracy. It is also broadly consistent with many of the factorisation predictions in Table 1.3.

- ◇ The $B^+ \to f_0(980)K^+$ branching fraction is highly consistent with previous analyses [1, 74] and is slightly larger than, but consistent with the Belle amplitude analysis [73], again, with improved accuracy. The insights that this

[1] correcting for the secondary branching fraction $\mathcal{B}(K^{*0}(892) \to K^+\pi^-) = \frac{2}{3}$

measurement can provide into the nature of the $f_0(980)$ are discussed in Section 6.4.1.

- ◇ The $K_0^{*0}(1430)$ component has been measured with a high degree of precision. Section 6.4 discusses further the S-wave contributions to the Dalitz plot.

- ◇ As expected (Section 1.4.2) the $K^{*0}(892)\pi^+$ charge asymmetry is consistent with zero. As such there is no evidence of new physics entering the penguin diagram loop.

- ◇ $B^+ \to \rho^0(770)K^+$ is measured to have a large charge asymmetry, although it is not yet a statistically significant measurement. As the *BABAR* data set increases it will become important to better understand the systematic uncertainties related to this measurement. This measurement can provide clues as to which factorisation models are most consistent since it was seen in Table 1.4 that the value of this asymmetry could vary wildly depending on the model used. The implications for factorisation of all the results will be discussed in Section 6.3.

- ◇ It is seen from Table 5.7 and Table 5.8 that removing the phase-space non resonant component from the nominal model gives very little change in the goodness-of-fit χ^2 or the fit likelihood. Furthermore the region between 2 and 3 GeV in the $\pi^+\pi^-$ spectrum of Figure 5.10 and particularly Figure 5.11 indicate that this component is being over-fitted in the nominal fit. This is supported by the toy Monte Carlo fit tests in Section 5.3. Section 6.4 will discuss this issue further.

6.3 Implications for Factorisation

Comparison between the results obtained from this analysis and the predictions made by various factorisation theory models can help to constrain which types of

model are most successful. Looking initially at the branching fraction measurements it is immediately clear that the $B^+ \to K^{*0}(892)\pi^+$ measurement is larger than any of the predictions, the closest being "Scenario 2" of [34], which is $\sim 11.1 \times 10^{-6}$. This model also yields a value for $B^+ \to \rho^0(770)K^+$ that is consistent with that measured in this analysis. The model used in this case is one based on QCD factorisation that includes so called "charming penguin" long distance interactions. Similarly in [35] it is the model that includes these terms that is more successful.

By contrast, none of the models in [36] include such effects, the differences in their models being whether naive or QCD factorisation is used, the values of certain CKM parameters and the exclusion or inclusion of weak annihilation amplitudes. Since the predicted rates for $K^{*0}(892)\pi^+$ in each of these models are between a factor 3 to 5 too small and the values for $\rho^0(770)K^+$ are all approximately an order of magnitude too small it would appear that the inclusion of long distance effects is necessary. The approach in [20] also does not include such effects but their final scenario, in which a combination of including weak annihilation amplitudes with non-universal phases and an enhancement of the penguin:tree ratio in $B^0 \to \pi^+\pi^-$ decays, yields their closest values, but these are still too small to be compatible with the results presented here.

The predictions from [33] are not based on factorisation but a rather different approach that relies on assumptions of isospin and SU(3) flavour symmetry. They provide an interesting comparison with the factorisation models. Their fits were found to have three minima, corresponding to different values of the CKM angle γ, these are the three different values reported in Table 1.3. From the values measured here, the first solution, which corresponds to $\gamma = 26^\circ$ is favoured, but the difference between the solutions is marginal.

Comparison of the *CP* asymmetries also provides some information although they are not experimentally well constrained. The asymmetry for $K^{*0}(892)\pi^+$ is expected to be zero, or very small and indeed is measured to be consistent with zero in

this analysis. As such it is in good agreement with all the predictions and so the values for $\rho^0(770)K^+$ must be examined in order to provide some discrimination. Unfortunately, there are no predictions for $\rho^0(770)K^+$ provided in [34], but those in [35] and [36] appear to be of the wrong magnitude. The final scenario in [20] is the closest agreement of all the predictions and finally those of [33], which are all very similar, are consistent with the result of this analysis and are certainly of the same sign.

Measurements of the $K^{*0}(892)\pi^+$ and $\rho^0(770)K^+$ branching fractions and also particularly the $\rho^0(770)K^+$ charge asymmetry with greater precision will definitely help to constrain and refine the factorisation models. Better refined models could then be employed to make more accurate predictions of even rarer modes such as $B^+ \to K^{*0}(892)K^+$ and $B^+ \to \phi\,\pi^+$, which in turn help to constrain the theoretical uncertainties on measuring $\sin 2\beta$ in penguin modes [75].

6.4 S-wave Contributions

The most uncertain part of the amplitude model is the exact form of the S-wave. In the $K^+\pi^-$ spectrum the possible contributions come from the $K_0^{*0}(1430)$ and from a non resonant amplitude. In the $\pi^+\pi^-$ spectrum there may also be a non resonant contribution plus the $f_0(980)$ and potentially higher f resonances such as the $f_0(1370)$ and $f_0(1500)$.

In this analysis the $K^+\pi^-$ S-wave has been modelled using the LASS parameterisation, which consists of the $K_0^{*0}(1430)$ plus a non resonant contribution that is not distributed according to phase space but takes an effective range form. In the $\pi^+\pi^-$ spectrum the $f_0(980)$ resonance is modelled as a Flatté and higher f's are included in extended models as relativistic Breit–Wigner lineshapes. No specific non resonant term was included in the $\pi^+\pi^-$ spectrum but in the nominal fit a phase space non resonant component is included. These choices were empirically driven and it may

be that there is a better way of describing the S-wave. The analysis results point towards the phase space non resonant component being unnecessary to model the data currently available. It furthermore indicates that the LASS parameterisation models the data extremely well in the $K^+\pi^-$ spectrum. As to the presence of higher f resonances, the results are inconclusive although the data does show enhancement in that region of the spectrum (Figure 5.12 and Figure 5.13).

Belle's analysis of this Dalitz plot uses an ad hoc shape for the non resonant component and they observe a strong correlation between this component and the $K_0^{*0}(1430)$ component [73]. It is hard to compare these results with theirs but the sum of the non resonant and $K_0^{*0}(1430)$ branching fractions is compatible between the two analyses: $\sim 45 \times 10^{-6}$ from Belle and $\sim 37 \times 10^{-6}$ from this analysis. The combined experimental errors being $\sim 4 \times 10^{-6}$.

One possible improvement that could be tried is to add an effective range term to the $f_0(980)$ amplitude in much the same way as the LASS parameterisation does for the $K_0^{*0}(1430)$. There are also several suggestions as to separate parameterisations for the non resonant component, some based on theory [76] and others simply ad hoc functions [73]. The suggestion that the apparent non resonant is in fact due to very wide resonances such as the κ and σ is another possible explanation, however studies in the $B^+ \to \pi^+\pi^-\pi^+$ Dalitz plot show little evidence for a contribution from the σ [77]. All of these possibilities could be investigated in future iterations of the analysis. It is certainly true that B-meson decays are not the best place to determine these parameterisations because they suffer from low statistics and high background levels. However there is little choice at the present time but to attempt to do so since there is no standard approach.

6.4.1 The $f_0(980)$

The presence of the $f_0(980)$ in this decay mode has now been well established by this analysis and the similar analysis by the Belle collaboration [73]. The composition

of the $f_0(980)$ is not well known but the fact that it is present in these B-meson decays can give hints as to its nature and rule out certain possibilities.

One possible theory as to the structure of the $f_0(980)$ is that it is a $K\overline{K}$-molecule. However, as pointed out in [78] the fact that it is ejected with an energy of around 2.5 GeV in this decay mode indicates that it is unlikely to be such a loosely bound state. However, it is unlikely that it is simply a conventional meson but could be a four-quark state. Its strong appearance in this decay mode compared with the much smaller signal for the $\rho^0(770)$ could point to a possible strong coupling to gluons according to [79]. Additionally its appearance in this decay mode combined with its absence from the $\pi^+\pi^-$ spectrum in the decay mode $B^0 \to J/\psi\,\pi^+\pi^-$ [80,81] indicates that the coupling of the $f_0(980)$ to $s\overline{s}$ is greater than its coupling to $d\overline{d}$. This is because it is the $d\overline{d}$ state that produces the $\pi^+\pi^-$ resonance in both the tree and penguin diagrams for $B^0 \to J/\psi\,\pi^+\pi^-$ while in $B^+ \to K^+\pi^-\pi^+$ it can have additional contributions from and $s\overline{s}$ penguin diagram shown in Figure 6.1.

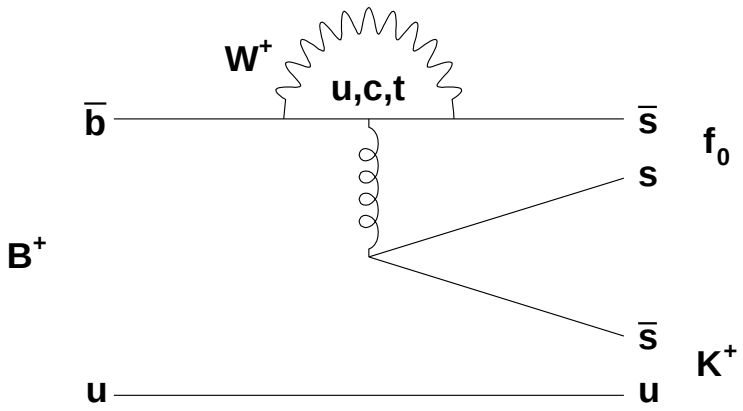

Figure 6.1: *Feynman diagram for $B^+ \to f_0(980)K^+$ with a strong $s\overline{s}$ coupling.*

6.5 Future Enhancements

In addition to the parameterisation of the S-wave just discussed there are four main areas in which the analysis could be enhanced:

- ◇ improving the algorithm to calculate the fit χ^2
- ◇ modelling of the possible effects of experimental resolution and distribution of Self Cross Feed events
- ◇ an expansion of the likelihood to include the $m_{\rm ES}$ variable allowing the combination of the two current fits into one
- ◇ the possibility of performing a simultaneous fit to the combined B^+ and B^- samples, including terms for both charges in the likelihood

6.5.1 Fit χ^2 Determination

Figure 5.14 and Figure 5.15 show that the current algorithm for combining the Dalitz plot bins is sufficient near the edges of the plot where the majority of events lie but is inadequate for the less populous centre of the plot. This is not a large problem since the areas where it is successful are those where the resonances of interest lie. However in order for a rigorous test of the fit quality to be provided improvements are needed. There are two possible approaches which can be combined for greater effect. The first is to calculate the χ^2 not in the conventional Dalitz plane but in the so called "square Dalitz plot" proposed in [82] and used in a slightly adapted form in [83]. This construction has the effect of spreading the edges of the Dalitz plot towards the centre, giving a more uniform population. The second approach is to attempt to combine a greater number of bins in order to reach the minimum content level. Some upper limit to the number of bins to be combined must be imposed because comparing the content of bins of too great a size will provide no information. Defining a generic algorithm for this procedure will be challenging.

6.5.2 Resolution and Self Cross Feed Effects

Although the amount of Self Cross Feed (Section 4.4.2) is small its effect will become more significant as the statistics available increase. Separation of Self Cross Feed from correctly reconstructed signal requires the use of Monte Carlo truth matching, which can be imperfect. Although the effect of this should be small it is desirable to avoid its use if possible. Resolution effects are not great because the resonances in the $K^+\pi^-\pi^+$ plot are generally wide with respect to the scale of the detector resolution. The χ_{c0} is the narrowest resonance in the $K^+\pi^-\pi^+$ plot and may be subject to resolution effects but at the present time they do not affect the results of the analysis because of the low χ_{c0} branching fraction. Other Dalitz plots such as $B^+ \to K^+K^-K^+$ contain resonances like ϕ, which are very narrow and as such the amplitude fit needs to account for them. A technique that can be used to model both of these effects is described in detail in [84] and is summarised here.

The technique uses a large sample of full simulation Monte Carlo events to provide a set of weights for each data event. A MC event is associated with a data event based on the proximity of its reconstructed Dalitz position to the data event but the size of the weight is based on the value of the signal amplitude at its MC truth Dalitz position. The signal likelihood function for a given data event, x, becomes:

$$\mathcal{L} = \frac{\sum_{\tilde{y}_j \in V_x} W(y_j, \vec{\mu})}{V_x \sum_{j=1}^{M} W(y_j, \vec{\mu})} \tag{6.1}$$

where there are M generated events in the MC sample; a given MC event j has a reconstructed position $\tilde{y_j}$ and a MC truth position y_j; $W(y_j, \vec{\mu})$ is the original amplitude function, which is a function of Dalitz position and has parameters $\vec{\mu}$; V_x is the volume around the reconstructed position of the data event in which a MC event's reconstructed position must fall in order for it to be associated with the data event.

This technique also has the effect of removing the need for the efficiency histogram from the amplitude fit since the numerator in Eq. (6.1) sums over all the generated MC events the efficiency is built in to the signal likelihood, *i.e.* this technique models

all detector effects. The method is yet to be tested in the `Laura++` amplitude fit and it may prove to be computationally too expensive since the amplitude function has to be evaluated for every MC event rather than for each of the very much smaller sample of data events. If the fit is not slowed too badly then this will prove to be an excellent tool for improving the accuracy of the fits.

6.5.3 Combined Amplitude and m_{ES} Fit

One of the largest sources of systematic uncertainty on the fit fraction measurements is the error on the continuum fraction, which is at present fixed in the amplitude fit. Combining the m_{ES} and amplitude fits allows the small amount of separation power of the Dalitz variables to be added to that of the m_{ES} variable, increasing the continuum discrimination of the fit as well as removing the continuum fraction as a source of systematic uncertainty. Furthermore it may be better to turn this combined fit into an extended one and to fit for the actual numbers of event rather than fractions. Adding further discriminating variables such as ΔE may be possible if correlations with the Dalitz position can be taken into account, perhaps by extending the MC method just described.

6.5.4 Combined Charge Fit

Combining the two fits to the separate charges into a single fit will allow the extraction of several more fit-fraction-like constructs known as the *CP*-conserving fit fraction, *CP*-violating fit fraction and the *CP*-violating interference fraction (all defined in [68]) as well as the weak and strong phases for each amplitude component. These extra variables give different handles for probing for *CP* violation and new physics with the larger statistics that will become available as *BABAR* continues to record more data.

A

Yield Fit PDF Parameters

This appendix gives the values of the PDF parameters used in the fit to determine the signal and continuum background yields described in Section 4.6. The signal parameters are given in Table A.1, the $q\overline{q}$ background parameters are given in Table A.2 and those of the $B\overline{B}$ background are given in Table A.3.

Table A.1: *The signal $m_{\rm ES}$ fit parameters*

Parameter	MC Value	Data Value (if floated)
Core Gaussian Mean	5.27970 ± 0.00003	5.2800 ± 0.0001
Core Gaussian Width	0.00226 ± 0.00002	—
Secondary Gaussian Mean	5.27780 ± 0.00002	—
Secondary Gaussian Mean	0.00285 ± 0.00004	—
Core Gaussian Fraction	0.705 ± 0.042	—

Table A.2: *The $q\overline{q}$ background $m_{\rm ES}$ fit parameters*

Parameter	Off Peak Data Value	On Peak Data Value (if floated)
ARGUS Shape	-17.7 ± 2.6	-17.8 ± 1.0
ARGUS End Point	Fixed to 5.29	

Table A.3: *The $B\overline{B}$ background $m_{\rm ES}$ fit parameters*

Parameter	MC Value
Gaussian Mean	5.27900 ± 0.00031
Gaussian Width	0.00299 ± 0.00030
ARGUS Shape	-24.4 ± 3.1
ARGUS End Point	Fixed to 5.29
ARGUS Fraction	0.888 ± 0.012

References

[1] *BABAR* Collaboration, B. Aubert, et al. Measurements of the branching fractions of charged B decays to $K^{\pm}\pi^{\mp}\pi^{\pm}$ final states. *Phys. Rev.*, D70:092001, 2004.

[2] Particle Data Group, S. Eidelman, et al. Review of Particle Physics. *Phys. Lett. B*, 592:1–1109, 2004.

[3] M. Kobayashi and T. Maskawa. *CP* violation in the renormalizable theory of weak interaction. *Prog. Theor. Phys.*, 49:652–657, 1973.

[4] Ling-Lie Chau and Wai-Yee Keung. Comments on the parametrization of the Kobayashi-Maskawa matrix. *Phys. Rev. Lett.*, 53:1802, 1984.

[5] Matthias Neubert. B physics and *CP* violation. *Int. J. Mod. Phys.*, A11:4173–4240, 1996.

[6] Lincoln Wolfenstein. Parametrization of the Kobayashi-Maskawa matrix. *Phys. Rev. Lett.*, 51:1945, 1983.

[7] Julian S. Schwinger. Spin, statistics, and the TCP theorem. *Proc. Nat. Acad. Sci.*, 44:223–228, 1958.

[8] P. F. Harrison and H. R. Quinn. The *BABAR* physics book: Physics at an asymmetric B factory. Papers from Workshop on Physics at an Asymmetric B

Factory (BaBar Collaboration Meeting), Rome, Italy, 11-14 Nov 1996, Princeton, NJ, 17-20 Mar 1997, Orsay, France, 16-19 Jun 1997 and Pasadena, CA, 22-24 Sep 1997.

[9] C. Jarlskog. Commutator of the quark mass matrices in the standard electroweak model and a measure of maximal cp violation. *Phys. Rev. Lett.*, 55:1039, 1985.

[10] C. S. Wu, E. Ambler, R. W. Hayward, D. D. Hoppes, and R. P. Hudson. Experimental test of parity conservation in beta decay. *Phys. Rev.*, 105:1413–1414, 1957.

[11] J. H. Christenson, J. W. Cronin, V. L. Fitch, and R. Turlay. Evidence for the 2 π decay of the K_2^0 meson. *Phys. Rev. Lett.*, 13:138–140, 1964.

[12] *BABAR* Collaboration, B. Aubert, et al. Observation of *CP* violation in the B^0 meson system. *Phys. Rev. Lett.*, 87:091801, 2001.

[13] V. Fanti et al. A new measurement of direct *CP* violation in two pion decays of the neutral kaon. *Phys. Lett.*, B465:335–348, 1999.

[14] A. Alavi-Harati et al. Observation of direct *CP* violation in $K_{S,L} \to \pi\pi$ decays. *Phys. Rev. Lett.*, 83:22, 1999.

[15] *BABAR* Collaboration, B. Aubert, et al. Observation of direct *CP* violation in $B^0 \to K^+\pi^-$ decays. *Phys. Rev. Lett.*, 93:131801, 2004.

[16] *BABAR* Collaboration, B. Aubert, et al. Improved measurement of *CP* asymmetries in $B^0 \to c\overline{c}K^{(*)0}$ decays. 2004. hep-ex/0408127.

[17] Belle Collaboration, K. Abe, et al. Improved measurement of *CP*-violation parameters $\sin(2\phi_1)$ and $|\lambda|$, B meson lifetimes, and $B^0\overline{B}^0$ mixing parameter Δm_d. 2004. hep-ex/0408111.

[18] Gerhard Buchalla, Andrzej J. Buras, and Markus E. Lautenbacher. Weak decays beyond leading logarithms. *Rev. Mod. Phys.*, 68:1125–1144, 1996.

[19] Ahmed Ali, G. Kramer, and Cai-Dian Lu. Experimental tests of factorization in charmless non- leptonic two-body B decays. *Phys. Rev.*, D58:094009, 1998.

[20] Martin Beneke and Matthias Neubert. QCD factorization for $B \to PP$ and $B \to PV$ decays. *Nucl. Phys.*, B675:333–415, 2003.

[21] R. H. Dalitz. *Phil. Mag.*, 44, 1953.

[22] S. Spanier. Parametrization of the dynamics of partial wave amplitudes. *BABAR* Analysis Document #303.

[23] J. Blatt and V. E. Weisskopf. *Theoretical Neuclear Physics*. J. Wiley (New York), 1952.

[24] Stanley M. Flatte. Coupled - channel analysis of the $\pi\eta$ and $K\overline{K}$ systems near $K\overline{K}$ threshold. *Phys. Lett.*, B63:224, 1976.

[25] BES Collaboration, M. Ablikim, et al. *Phys. Lett.*, B598:149–158, 2004.

[26] E791 Collaboration, E. M. Aitala, et al. *Phys. Rev. Lett.*, 86:765–769, 2001.

[27] WA76 Collaboration, T. A. Armstrong, et al. *Z. Phys.*, C51:351–364, 1991.

[28] Howard E. Haber. Spin formalism and applications to new physics searches. 1994. hep-ph/9405376.

[29] D. Aston et al. A study of $K^-\pi^+$ scattering in the reaction $K^-p \to K^-\pi^+n$ at 11 GeV/c. *Nucl. Phys.*, B296:493, 1988.

[30] W. M. Dunwoodie. Fits to $K\pi$ I=$\frac{1}{2}$ S-wave amplitude and phase data. http://www.slac.stanford.edu/∼wmd/kpi_swave/kpi_swave_fit.note.

[31] D. V. Bugg. Comments on the sigma and kappa. *Phys. Lett.*, B572:1–7, 2003.

[32] W. N. Cottingham, I. B. Whittingham, N. de Groot, and F. F Wilson. Factorization and hadronic B decays in the heavy quark limit. *J. Phys.*, G28:2843–2860, 2002.

[33] Cheng-Wei Chiang, Michael Gronau, Zumin Luo, Jonathan L. Rosner, and Denis A. Suprun. Charmless $B \to VP$ decays using flavor SU(3) symmetry. *Phys. Rev.*, D69:034001, 2004.

[34] R. Aleksan, P. F. Giraud, V. Morenas, O. Pene, and A. S. Safir. Testing QCD factorisation and charming penguins in charmless $B \to PV$. *Phys. Rev.*, D67:094019, 2003.

[35] W. N. Cottingham, N. de Groot, and I. B. Whittingham. Factorization fits and the unitarity triangle in charmless two-body B decays. *Phys. Rev.*, D68:113005, 2003.

[36] Dong-sheng Du, Hai-jun Gong, Jun-feng Sun, De-shan Yang, and Guo-huai Zhu. Phenomenological analysis of charmless decays $B \to PV$ with QCD factorization. *Phys. Rev.*, D65:094025, 2002.

[37] W. Kozanecki. The PEP-II B-factory: Status and prospects. *Nucl. Instrum. Meth.*, A446:59–64, 2000.

[38] J. Seeman et al. Results and plans of the PEP-II B-factory. Presented at 9th European Particle Accelerator Conference (EPAC 2004), Lucerne, Switzerland, 5-9 Jul 2004.

[39] J. L. Turner et al. Trickle-charge: A new operational mode for PEP-II. Presented at 9th European Particle Accelerator Conference (EPAC 2004), Lucerne, Switzerland, 5-9 Jul 2004.

[40] *BABAR* Collaboration, B. Aubert, et al. The *BABAR* detector. *Nucl. Instrum. Meth.*, A479:1–116, 2002.

[41] A. Snyder. The effect of vertx cuts on *CP* reach. *BABAR* Note #177, 1994.

[42] A. J. S. Smith et al. A barrel IFR instrumented with limited streamer tubes. http://www.slac.stanford.edu/BFROOT/www/Detector/LST/documentation/LSTprop-A4-May30-ajss.pdf.

[43] The Objectivity^{TM} database. http://www.objectivity.com.

[44] Pierre Billoir. Track fitting with multiple scattering: A new method. *Nucl. Instr. Meth.*, A225:352, 1984.

[45] S. Spanier and G. Mancinelli. Kaon selection at *BABAR*. *BABAR* Analysis Document #116.

[46] T. Brandt. likelihood-based electron identification. *BABAR* Analysis Document #396.

[47] C. Hearty. Measurement of the number of $\Upsilon(4S)$ mesons produced in Run 1 (B counting). *BABAR* Analysis Document #134.

[48] W. M. Dunwoodie. Simple observations on $B\overline{B}$ kinematics. http://www.slac.stanford.edu/∼wmd/bbkinematics/kinematics.note.

[49] W. T. Ford. Choice of kinematic variables in B meson reconstruction - Take 3. *BABAR* Analysis Document #53.

[50] D. M. Asner et al. Search for exclusive charmless hadronic b decays. *Phys. Rev.*, D53:1039–1050, 1996.

[51] O. Deschamps et al. Tagging Higgs bosons in hadronic LEP-2 events with neural networks. New Computing Techniques in Physics Research IV, page 725, Pisa, April 1995.

[52] R. A. Fisher. The use of multiple measurements in taxonomic problems. *Annals Eugen.*, 7:179–188, 1936.

[53] A. Hoecker et al. Measurement of *CP*-violating asymmetries in $B^0 \to \pi^+\pi^-\pi^0$. *BABAR* Analysis Document #637.

[54] D. A. Bowerman et al. Measurement of the branching fraction and charge asymmetry for the decay $B^\pm \to K^{*\pm}\pi^0$. *BABAR* Analysis Document #814.

[55] L Lyons. *Statistics for nuclear and particle physicists*. Cambridge University Press, Cambridge, 1986.

[56] F. James and M. Roos. 'MINUIT' a system for function minimization and analysis of the parameter errors and correlations. *Comput. Phys. Commun.*, 10:343–367, 1975.

[57] F. James. MINUIT, function minimization and error analysis, reference manual. http://wwwasdoc.web.cern.ch/wwwasdoc/minuit/minmain.html.

[58] The Roofit toolkit for data modeling. http://roofit.sourceforge.net/.

[59] ROOT, an object oriented data analysis framework. http://root.cern.ch/.

[60] http://www.slac.stanford.edu/BFROOT/www/Physics/Analysis/AWG/chrmls_hadronic/ThreeBody/Software/Laura++/index.html.

[61] I. M. Sobol. *The Monte Carlo Method*. University Chicago Press, Chicago, 1974.

[62] Wahid Bhimji. *A study of the charmless decays of charged B mesons to the final state $K^+\pi^-\pi^+$ using the BABAR detector*. PhD thesis, University of Bristol, 2003.

[63] http://www.slac.stanford.edu/BFROOT/www/Physics/Analysis/AWG/chrmls_hadronic/ThreeBody/Software/NonCharm3BodyUser_cm2.html.

[64] *BABAR* Collaboration, B. Aubert, et al. Measurements of the branching fractions and charge asymmetries of charmless three-body charged B decays. *Phys. Rev. Lett.*, 91:051801, 2003.

[65] *BABAR* Collaboration, B. Aubert, et al. Measurement of the branching fraction for $B^+ \to K^{*0}\pi^+$. 2001. hep-ex/0109007.

[66] Heavy Flavor Averaging Group. http://www.slac.stanford.edu/xorg/hfag/.

[67] H. Albrecht et al. Exclusive hadronic decays of B mesons. *Z. Phys.*, C48:543–552, 1990.

[68] D. M. Asner et al. Search for *CP* violation in $D^0 \to K^0_S\pi^+\pi^-$. *Phys. Rev.*, D70:091101, 2004.

[69] S. Fajfer, R. J. Oakes, and T. N. Pham. *CP* violating phase γ and the partial widths asymmetry in $B^- \to \pi^+\pi^-K^-$ and $B^- \to K^+K^-K^-$ decays. *Phys. Lett.*, B539:67–75, 2002.

[70] W. H. Press, S. A. Teukolsky, W. T. Vetterling, and B. P. Flannery. *Numerical recipes in C*. Cambridge University Press, Cambridge, 1998.

[71] Muriel Pivk and Francois R. Le Diberder. ${}_s\mathcal{P}lot$: a statistical tool to unfold data distributions. 2004. physics/0402083.

[72] A. Hoecker and M. Laget. Resolving mirror solutions in $B^0 \to \pi^+\pi^-\pi^0$ with a genetic algorithm. *BABAR* Analysis Document #672.

[73] A. Garmash et al. Dalitz analysis of the three-body charmless decays $B^+ \to K^+\pi^-\pi^+$ and $B^+ \to K^+K^-K^+$. hep-ex/0412066.

[74] Belle Collaboration, K. Abe, et al. Study of three-body charmless B decays. *Phys. Rev.*, D65:092005, 2002.

[75] Yuval Grossman, Zoltan Ligeti, Yosef Nir, and Helen Quinn. SU(3) relations and the *CP* asymmetries in B decays to $\eta' K^0_S$, ϕK^0_S and $K^+K^-K^0_S$. *Phys. Rev.*, D68:015004, 2003.

[76] B. Bajc, S. Fajfer, R. J. Oakes, T. N. Pham, and S. Prelovsek. The *CP* violating asymmetry in $B^\pm \to M\bar{M}\pi^\pm$ decays. *Phys. Lett.*, B447:313–320, 1999.

[77] *BABAR* Collaboration, B. Aubert, et al. Amplitude analysis of $B^\pm \to \pi^\pm\pi^\mp\pi^\pm$ and $B^\pm \to K^\pm\pi^\mp\pi^\pm$. hep-ex/0408032.

[78] Hai-Yang Cheng and Wei-Shu Hou. B decays as spectroscope for charmed four-quark states. *Phys. Lett.*, B566:193–200, 2003.

[79] Peter Minkowski and Wolfgang Ochs. Scalar mesons and glueball in B decays and gluon jets. 2003. hep-ph/0304144.

[80] *BABAR* Collaboration, B. Aubert, et al. A measurement of the $B^0 \to J/\psi\,\pi^+\pi^-$ branching fraction. *Phys. Rev. Lett.*, 90:091801, 2003.

[81] Belle Collaboration, K. Abe, et al. Measurement of branching fractions in $B^0 \to J/\psi\,\pi^+\pi^-$ decay. 2004. hep-ex/0408107.

[82] W. M. Dunwoodie. Suggestion for the parametrization of Dalitz plot efficiency. http://www.slac.stanford.edu/∼wmd/bbkinematics/dalitz_efficiency.note.

[83] *BABAR* Collaboration, B. Aubert, et al. $B^0 \to K^+\pi^-\pi^0$ Dalitz plot analysis. 2004. hep-ex/0408073.

[84] D. M. Schmidt, R. J. Morrison, and Michael S. Witherell. A general method of estimating physical parameters from a distribution with acceptance and smearing effects. *Nucl. Instrum. Meth.*, A328:547–552, 1993.